Modern and future colliders

V. Shiltsev

Fermilab, P.O. Box 500, MS339, Batavia, Illinois 60510, USA

F. Zimmermann

European Organization for Nuclear Research, CERN, 1211 Geneve, Switzerland

(published 3 March 2021)

Since the initial development of charged particle colliders in the middle of the 20th century, these advanced scientific instruments have been at the forefront of scientific discoveries in high-energy physics. Collider accelerator technology and beam physics have progressed immensely and modern facilities now operate at energies and luminosities many orders of magnitude greater than the pioneering colliders of the early 1960s. In addition, the field of colliders remains extremely dynamic and continues to develop many innovative approaches. Indeed, several novel concepts are currently being considered for designing and constructing even more powerful future colliders. The colliding-beam method and the history of colliders are first reviewed. Then, the major achievements of operational machines and the key features of near-term collider projects that are currently under development are presented. The review concludes with an analysis of numerous proposals and studies for distant-future colliders. The evaluation of their respective potentials reveals promising prospects for further significant breakthroughs in the collider field.

DOI: 10.1103/RevModPhys.93.015006

CONTENTS

I. INTRODUCTION

Particle accelerators are unique scientific instruments that offer access to unprecedented energy per constituent, using well-focused high density beams of electrons (e^-), positrons (e^+), protons (p), antiprotons ($\bar{p}$), ions (i), muons (μ^+, μ^-), mesons, photons, and gamma quanta (γ), among others (Livingston, 1954; Scharf, 1989; Sessler and Wilson, 2014). They have been widely used for physics research since the early 20th century and have greatly progressed both scientifically and technologically since. Analysis of all Nobel Prize–winning research in physics since 1939 (Nobel Foundation, 2020) [the year that the Nobel Prize was awarded to Ernest O. Lawrence for the invention of the first modern accelerator, the cyclotron (Lawrence and Livingston, 1932)] reveals that accelerators have played an integral role in influencing more than a quarter of physics-prize recipients by either inspiring them or facilitating their research. On average, accelerators have contributed to one Nobel Prize in Physics every three years (Haussecker and Chao, 2011). Four Nobel prizes have directly honored breakthroughs in accelerator science and technology; in

addition to Lawrence, John Cockcroft and Ernest Walton received the prize in 1951 for their invention of the eponymous linear accelerator (Cockcroft and Walton, 1932), and Simon van der Meer received the prize in 1984 for conceiving and developing the novel method of stochastic cooling (van der Meer, 1985). To gain an insight into the physics of elementary particles, one accelerates them to high kinetic energy, lets them strike other particles, and detects products of the ensuing reactions that transform the particles into new particles, such as the Higgs boson, which was discovered in the debris of proton-proton collisions at the CERN Large Hadron Collider (LHC) (Bruning and Collier, 2007) and celebrated with the 2013 Nobel Prize in Physics (Englert, 2014; Higgs, 2014). Recently accelerator-based synchrotron-radiation sources were instrumental for a number of Nobel Prize–winning research achievements in chemistry and biology, recognized in 1997, 2003, 2006, 2009, and 2012. At present, about 140 accelerators of all types worldwide are devoted to fundamental research (ELSA Working Group, 2019).

In the United States alone, the Department of Energy (DOE) Office of Science is supporting 16 large accelerator-based user facilities open for basic research (such as colliders, light sources, and neutron sources), with a total annual budget for operation and construction exceeding $2 billion (U.S. Department of Energy, Office of Science User Facilities, 2019). These facilities enable scientific research to be carried out by about 20 000 users from academia, industry, and government laboratories.

In 2012, the EU's TIARA project identified 125 European public-sector accelerator infrastructures in 12 countries (Austria, Denmark, Finland, France, Germany, Italy, Poland, Slovenia, Spain, Sweden, Switzerland, and the United Kingdom), along with their annual operating costs and replacement value (Bordais *et al.*, 2012). These 125 infrastructures included the e^+e^- collider DAΦNE in Frascati, Italy, with a construction budget of about 100 million euro, 3.5 million euro annual costs for electricity and maintenance, and about 60 full-time equivalents operating the collider infrastructure. Several other laboratories, including Germany's DESY and France's CNRS, have historically hosted colliding-beam facilities such as DORIS, PETRA, and HERA, or ACO and DCI, respectively. Europe's leading particle-physics laboratory the European Organization for Nuclear Research (CERN), with an annual budget of about 1.15 billion CHF (CERN, 2019a), operates the world's largest accelerator complex and brings together 17 000 physicists, engineers, and technicians from more than 110 countries.

In Asia, Japan's KEK is presently running SuperKEKB with about 100 accelerator experts to serve the Belle II detector, involving more than 1000 researchers from 23 countries. IHEP in China operates the BEPCII collider, with about 50 accelerator staff, for the BESIII detector, which has about 500 members in 15 countries. Russia's Budker Institute of Nuclear Physics (BINP) boasts a long-standing tradition in electron-positron colliders and is presently operating two: VEPP-4M and VEPP2000. BINP employs about 1000 technical experts.

Colliders are arguably the most complex of all accelerator types and employ the most advanced technologies and beam physics techniques to push the envelope of their performance (Shiltsev, 2011). What makes them the instruments of choice for particle physics is their kinematic advantage of a high center-of-mass energy resulting in larger momentum transfers. Indeed, the center-of-mass energy (c.m.e.) $E_{\mathrm{c.m.e.}}$ [also often cited as $\sqrt{s}$, the square root of one of the Lorentz-invariant *Mandelstam variables* in the kinematics of reactions; see Perkins (2000)] for the head-on collision of two particles of masses m_1 and m_2 with energies E_1 and E_2 colliding at a crossing angle θ_c is

$$E_{\mathrm{c.m.e.}} = \left(2E_1E_2 + (m_1^2 + m_2^2)c^4 + 2\cos\theta_c\sqrt{E_1^2 - m_1^2c^4}\sqrt{E_2^2 - m_2^2c^4}\right)^{1/2}, \quad (1)$$

where c denotes the speed of light.

For many decades throughout the first half of the 20th century, the only arrangement for accelerator experiments involved a fixed-target setup, where a beam of charged particles accelerated with a particle accelerator hits a stationary target set into the path of the beam. In this case, as follows from Eq. (1), for high-energy accelerators $\gamma = E/mc^2 \gg 1$, $E_{\mathrm{c.m.e.}} \approx \sqrt{2Emc^2}$, assuming that $m_1 = m_2 = m$. The collision of $E_b =$ 7000 GeV protons with stationary protons $mc^2 \approx 1$ GeV can produce reactions with $E_{\mathrm{c.m.e.}}$ of about 120 GeV. A more effective colliding-beam setup in which two beams of particles are accelerated and directed against each other offers a much higher center-of-mass energy of $E_{\mathrm{c.m.e.}} \approx 2\sqrt{E_1E_2}$, assuming a typically small or zero crossing angle $\theta_c \approx 0$. In the case of two equal masses of colliding particles (such as protons and protons or protons and antiprotons) with the same energy of 7000 GeV, one obtains $E_{\mathrm{c.m.e.}} = 2E_b$ or 14 000 GeV. Several machines operate with beams of unequal energies, either because the colliding particles have different masses (electron-proton collisions at HERA, *p-A* collisions at the LHC) or because of the need to generate new short-lived particles, such as *B* mesons, with a Lorentz boost so as to more easily detect and analyze their decays (asymmetric *B* factories KEKB, PEP-II, and SuperKEKB).

In total, 31 colliders have thus far reached the operational stage (some in several successive configurations), and seven of these are currently operational; see Table I. These facilities have essentially shaped modern particle physics (Hoddeson *et al.*, 1997; Ellis, Stirling, and Webber, 2003; Barger, 2018). The idea of exploring collisions in the center-of-mass system to fully exploit the energy of accelerated particles was first given serious consideration by the Norwegian engineer and inventor Rolf Wideröe, who in 1943 filed a patent for the collider concept (and received the patent in 1953) (Wideroe, 1953; Waloschek, 2013). This idea was further developed by Kerst *et al.* (1956) and O'Neill (1956), and in the late 1950s three teams started working on colliding beams: (i) a Princeton-Stanford group in the United States that included William Barber, Bernard Gittelman, Gerald O'Neill, and Burton Richter, who in 1959 proposed building a couple of tangent rings to study Møller scattering $e^-e^- \to e^-e^-$ [Stanford colliding-beam experiment CBX (Barber *et al.*, 1959)]; (ii) a somewhat similar project initiated by Gersh

TABLE I. Past and present particle colliders: their particle species, maximum beam energy E_b, circumference or length C, maximum luminosity $\mathcal{L}$, and years of luminosity operation [i indicates ions; luminosity is in units of $\mathrm{cm}^{-2}\,\mathrm{s}^{-1}$: it is defined in Eq. (3) and discussed later].

	Species	E_b (GeV)	C (m)	$\mathcal{L}_{\mathrm{peak}}^{\mathrm{max}}$	Years
AdA	e^+e^-	0.25	4.1	10^{25}	1964
VEP-1	e^-e^-	0.16	2.7	5×10^{27}	1964–1968
CBX	e^-e^-	0.5	11.8	2×10^{28}	1965–1968
VEPP-2	e^+e^-	0.67	11.5	4×10^{28}	1966–1970
ACO	e^+e^-	0.54	22	10^{29}	1967–1972
ADONE	e^+e^-	1.5	105	6×10^{29}	1969–1993
CEA	e^+e^-	3.0	226	0.8×10^{28}	1971–1973
ISR	pp	31.4	943	1.4×10^{32}	1971–1980
SPEAR	e^+e^-	4.2	234	1.2×10^{31}	1972–1990
DORIS	e^+e^-	5.6	289	3.3×10^{31}	1973–1993
VEPP-2M	e^+e^-	0.7	18	5×10^{30}	1974–2000
VEPP-3	e^+e^-	1.55	74	2×10^{27}	1974 to 1975
DCI	e^+e^-	1.8	94.6	2×10^{30}	1977–1984
PETRA	e^+e^-	23.4	2304	2.4×10^{31}	1978–1986
CESR	e^+e^-	6	768	1.3×10^{33}	1979–2008
PEP	e^+e^-	15	2200	6×10^{31}	1980–1990
S$p\bar{p}$S	$p\bar{p}$	455	6911	6×10^{30}	1981–1990
TRISTAN	e^+e^-	32	3018	4×10^{31}	1987–1995
Tevatron	$p\bar{p}$	980	6283	4.3×10^{32}	1987–2011
SLC	e^+e^-	50	2920	2.5×10^{30}	1989–1998
LEP	e^+e^-	104.6	26 659	10^{32}	1989–2000
HERA	ep	$30+920$	6336	7.5×10^{31}	1992–2007
PEP-II	e^+e^-	$3.1+9$	2200	1.2×10^{34}	1999–2008
KEKB	e^+e^-	$3.5+8$	3016	2.1×10^{34}	1999–2010
VEPP-4M	e^+e^-	6	366	2×10^{31}	1979–present
BEPC-I/II	e^+e^-	2.3	238	10^{33}	1989–present
DAΦNE	e^+e^-	0.51	98	4.5×10^{32}	1997–present
RHIC	p, i	255	3834	2.5×10^{32}	2000–present
LHC	p, i	6500	26 659	2.1×10^{34}	2009–present
VEPP2000	e^+e^-	1.0	24	4×10^{31}	2010–present
S-KEKB	e^+e^-	$7+4$	3016	8×10^{35}[a]	2018–present

[a]Design.

Budker in the Soviet Union, where an electron-electron collider VEP-1 was under construction in 1958 (Budker, Yerozolimsky, and Naumov, 1962); and (iii) an Italian group at the Laboratori Nazionali di Frascati, led by Bruno Touschek, which began the design of the first electron-positron collider AdA (Bernardini *et al.*, 1960). In the early 1960s, almost concurrently, these first colliders went into operation in the Soviet Union (Budker, 1967; Levichev *et al.*, 2018), France (to where the AdA had been moved) (Bernardini *et al.*, 1964, 2004), and the United States (Gittelman, 1965; Rees, 1986).

Figure 1 presents the most common arrangements of colliding beams. In storage-ring configurations [Figs. 1(a) and 1(b)] particles of each beam circulate and repeatedly collide. Historically, a single ring was often used for colliding particle and antiparticle beams of equal energy. Modern and future storage-ring colliders (LHC, DAΦNE, BEPC-II, FCC, CEPC, SppC, etc.) utilize double rings to achieve extremely high luminosity by colliding a large number of bunches while avoiding spurious collisions at undesired locations. The two rings may store particles of the same type or particles and their

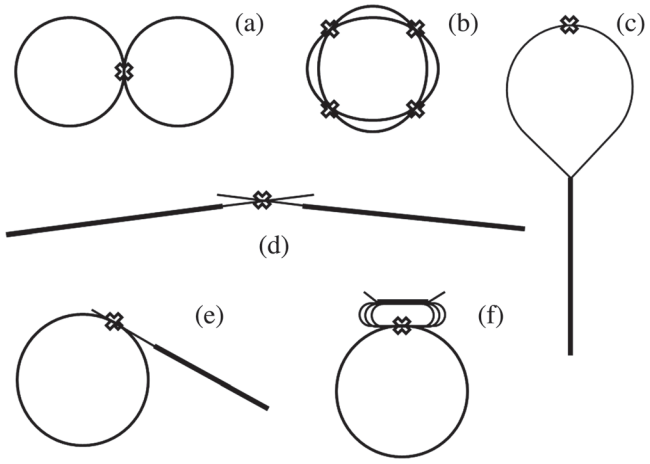

FIG. 1. Schematics of particle collider types.

antiparticles or two different particle types, like electrons and hadrons. In linear colliders, first proposed by Tigner (1965) and then further developed for higher energy by Amaldi (1976) and Balakin and Skrinsky (1979), the two colliding beams are accelerated in linear accelerators (linacs) and transported to a collision point, either with use of the same linac and two arcs shown in Fig. 1(c) or in the simple two-linac configuration depicted in Fig. 1(d). Other configurations are possible and have been considered, including the linac-ring schemes depicted in Fig. 1(e) or a collision of beams circulating in a ring and a few-pass energy recovery linac (ERL) [Fig. 1(f)].

In contrast to other types of accelerators, which have many diverse applications, colliders have exclusively served the needs of frontier particle-physics research [or what is now called high-energy physics (HEP) and nuclear physics]. The ever-growing demands of particle-physics research drove the increase in energy of colliders, as demonstrated in Fig. 2. In the figure, the triangles represent maximum c.m.e. and the start of operation for lepton colliders (mostly e^+e^-), while full circles represent hadron (protons, antiprotons, ions,

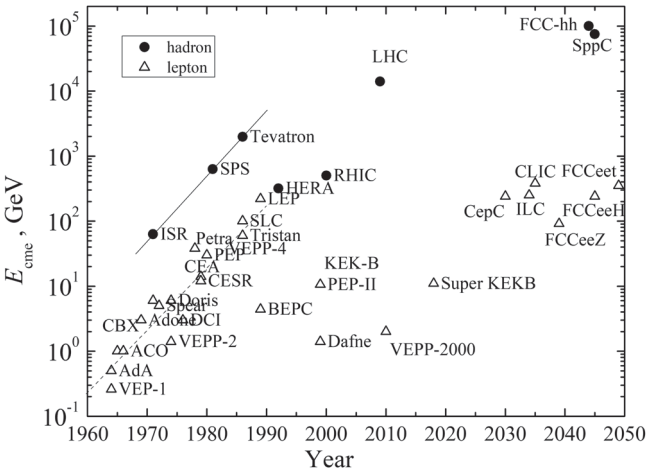

FIG. 2. Center-of-mass energy reach of particle colliders vs their start of operation. Solid and dashed lines indicate a tenfold increase per decade for hadron (circles) and lepton colliders (triangles). Adapted from Shiltsev, 2012a.

proton-electron) colliders. One can see that until the early 1990s, the c.m.e. increased on average by a factor of 10 every decade. Hadron colliders were 10–20 times more energetic (though hadrons are not elementary particles and only a fraction of their energy is available to produce new particles during collisions). Since then, the paths of different colliders have diverged: hadron colliders continued the quest for record high energies in particle reactions and the LHC was built at CERN, while in parallel highly productive e^+e^- colliders called *particle factories* focused on precise exploration of rare phenomena at much lower energies.

The exploration of rare particle-physics phenomena requires not only an appropriately high energy but also a sufficiently large number of detectable reactions. The number of events of interest $N_{\rm exp}$ is given by the following product of the cross section of the reaction under study $\sigma_{\rm exp}$ and the time integral over the instantaneous luminosity $\mathcal{L}$:

$$N_{\rm exp} = \sigma_{\rm exp} \int \mathcal{L}(t) dt. \tag{2}$$

The luminosity dimension is $[\text{length}]^{-2}\,[\text{time}]^{-1}$. The integral on the right is referred to as integrated luminosity $\mathcal{L}_{\rm int}$, and, reflecting the smallness of typical particle-interaction cross sections, or the correspondingly high integrated luminosity required, is often reported in units of inverse picobarn, femtobarn, or attobarn, where $1\ \text{b} = 10^{-24}\ \text{cm}^2$; $1\ \text{fb} = 10^{-39}\ \text{cm}^2$, for example. In fixed-target mode, luminosity is a product of the extracted high-energy particle flux rate times target density and length. Collider luminosity is defined only by the beam parameters and is dependent on beam densities, which are typically orders of magnitude lower than those of liquid or solid targets. Colliders usually employ bunched beams of particles with approximately Gaussian distributions, and for two bunches containing N_1 and N_2 particles and colliding head on with frequency $f_{\rm coll}$, a basic expression for the luminosity is

$$\mathcal{L} = f_{\rm coll} \frac{N_1 N_2}{4\pi \sigma_x^* \sigma_y^*}, \tag{3}$$

where σ_x^* and σ_y^* characterize the rms transverse beam sizes in the horizontal and vertical directions at the point of interaction; see Myers and Schopper (2013), Chap. 6.4. To achieve high luminosity, one therefore has to maximize the population and number of bunches, either producing these narrowly or focusing them tightly and colliding them at high frequencies at dedicated locations where products of their reactions can be registered by detectors. Figure 3 demonstrates the progress in luminosity of colliding-beam facilities since the invention of the method; over the past 50 years, the performance of colliders has improved by more than 6 orders of magnitude and reached record high values of over $10^{34}\ \text{cm}^{-2}\,\text{s}^{-1}$. At such a luminosity, one can expect to produce 5×10^6 events over 1 yr of operation (effectively, about 10^7 s) for a reaction cross section of $50\ \text{pb} = 5 \times 10^{-35}\ \text{cm}^2$. An example of a process with this magnitude is Higgs particle production $pp \to H + X$ at 14 TeV c.m.e. in the LHC (De Florian *et al.*, 2016).

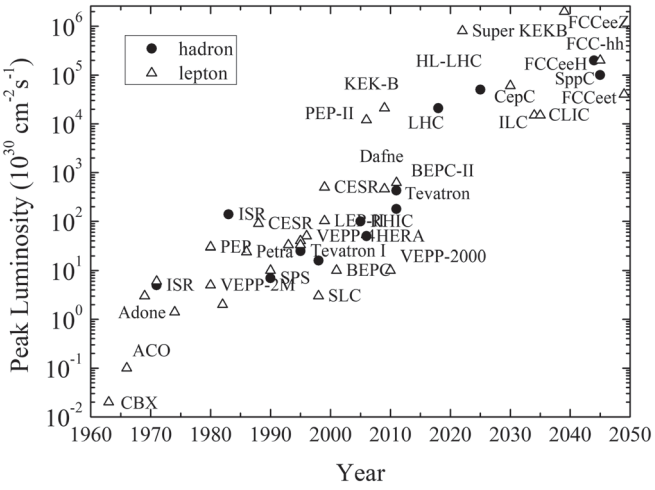

FIG. 3. Luminosities of particle colliders (triangles are lepton colliders and full circles are hadron colliders). Values are per collision point. Adapted from Shiltsev, 2012a.

Luminosity considerations differ significantly for lepton and hadron colliders. For pointlike colliding particles such as leptons, the reach of the collider, defined as the highest mass M of a particle that can be produced there, simply equals $E_{\rm c.m.e.}/c^2$. Because of the "$1/s$" scaling of the Feynman propagator for hard-scattering processes [here $s = (p_1 + p_2)^2$ again is the Mandelstam variable, with p_1 and p_2 denoting the four-momenta of the two incoming particles], the production cross section of M is proportional to $E_{\rm c.m.e.}^{-2}$ (Frauenfelder and Henley, 1991). To detect new particles of increasing mass, integrated luminosity should increase as $E_{\rm c.m.e.}^2$. As hadrons are quark-gluon composite objects, the probability of creating a new mass M depends on the quantum chromodynamics (QCD) parton distribution functions in the nucleon; the corresponding cross sections scale as $\sigma_{\rm exp} \propto E_{\rm c.m.e.}^{-2} f(Mc^2/E_{\rm c.m.e.})$, where $f(x)$ is a sharply falling function (Eichten *et al.*, 1984; Quigg, 2011a). In consequence, the collider mass reach is a strong function of $E_{\rm c.m.e.}$ and a weak function of $\mathcal{L}_{\rm int}$ (Salam and Weiler, 2019). For example, with a rough approximation of $f(x) \propto x^{-6}$, the mass discovery reach of a hadron collider scales as $M \propto E_{\rm c.m.e.}^{2/3} \mathcal{L}_{\rm int}^{1/6}$ (Teng, 2001). This peculiar characteristic of high-energy hadron colliders has been proven repeatedly in the past (see Sec. II), and it is often invoked to qualify them as "discovery machines."

In general, the key components of the experimental program toward an understanding of the structure of matter are particle detectors and accelerators. Advances in the detector technology and key challenges of the detectors for future hadron and lepton colliders are outside the scope of this review and were addressed by Tanabashi *et al.* (2018) (Chap. 34), Green (2000), Grupen and Shwartz (2008), and Ellis *et al.* (2019) (Chap. 11).

Over the past five decades, the quest for higher-energy particles have led to some 5 orders of magnitude boost of collider energies and an even greater increase in their luminosities; see Figs. 2 and 3. Simultaneously, the size, complexity, and cost of colliding-beam facilities have also increased. Modern colliders employ numerous technologies

for tunneling, geodesy and alignment, power converters and power supplies, ultrahigh vacuum systems, particle sources, injection and extraction systems, cooling water and cryogenic cooling, beam diagnostics, accelerator control, personnel safety, and machine protection, among others. While at the dawn of accelerator and collider technology most of these required dedicated and often pioneering developments, now many such technologies are widely available from specialized industries. Still left almost solely to the pursuit of accelerator engineers and scientists are the "core technologies" required for accelerating particles to high energies [normal-conducting and superconducting radio-frequency (rf) acceleration systems, and normal-conducting and superconducting accelerator magnets] and "beam physics techniques" to attain the necessary beam qualities such as intensity, brightness, and sometimes polarization. These techniques include beam cooling, manipulation, and collimation, the production of exotic particles like antiprotons or muons, mitigation of beam instabilities, and countermeasures against beam-size blowup caused by space-charge and beam-beam effects, or *intrabeam scattering* (IBS), among others. The energy reach of a collider is defined mostly by core accelerator technologies, while its luminosity is grossly dependent on the sophistication of beam physics techniques.

As arguably the biggest and the most technologically advanced scientific instruments, colliders have been and remain costly, often at the brink of financial and political affordability. That makes them prone to various risks and, in the past, several were terminated, even after the start of construction. Most notable in this respect are energy-frontier hadron colliders. In 1983, the construction of the 400 GeV c.m.e. ISABELLE pp collider (briefly renamed CBA) at the Brookhaven National Laboratory in the United States was stopped (Month, 2003; Crease, 2005a, 2005b), and in the early 1990s two other flagship projects were terminated: the 6 TeV c.m.e. proton-proton complex UNK (Yarba, 1990; Kuiper, 1994) in Protvino, Russia, and the 40 TeV c.m.e. proton-proton Superconducting Super Collider (SSC) in Texas in 1993 (Wojcicki, 2009; Riordan, Hoddeson, and Kolb, 2015). Notwithstanding, advances in core accelerator technologies [including the superconducting (SC) magnet developments for ISABELLE (or CBA), UNK, and SSC] have led to substantial reductions in collider cost per GeV (Shiltsev, 2014). This progress, together with the growing strength of the high-energy particle-physics community, enabled the development of frontier machines, such as the currently operational multibillion dollar LHC. Even larger $10-billion-scale future collider projects are generally considered feasible; see Secs. IV.B and IV.C.

On average, the colliders listed in Table I operated for 13 years, with many remarkable facilities operating for even twice that time (Adone, VEPP-2, CESR, Tevatron, VEPP-4M, BEPC-I/II). Contrary to other research accelerators, such as light sources, where user groups and experiments are numerous and each might have beam times lasting as little as weeks or a few days, over their lifetime most of these colliders served just one, two, or four permanently installed particle detector experiments surrounding the beam collision points. For example, PETRA, TRISTAN, Large Electron-Positron collider (LEP), Relativistic Heavy Ion Collider (RHIC) and the LHC each had (or have) four main collision points and detectors (Fernow and Fernow, 1989; Hauptman, 2011). The colliding-beam facilities usually consist of several machines needed to prepare and accelerate the beams and are generally highly complex, featuring several layers of structural hierarchy: numerous primary elements, combined in technical subsystems, composed in individual accelerators, highly interconnected and working synchronously as one complex. The largest of these require hundreds of highly skilled personnel for operation, including a sizable number of Ph.D. physicists. The complexity and scale of the colliders result in substantial lengths of time, usually many years, required for full commissioning and for attaining the ultimate luminosities (Shiltsev, 2011). It is characteristic for colliders to continuously proceed through a series of minor operational improvements, interleaved with a few major upgrades, and to see their performance increase all through their lifetimes.

Particle physics has not yet fully exploited the potential of the colliding-beam technique and is largely betting its future on it (Ellis, 2018). The current consensus is that "no other instrument or research programme can replace high-energy colliders in the search for the fundamental laws governing the universe" (Giudice, 2019).

In Sec. II, we briefly outline the development of colliders and the corresponding core accelerator technologies and beam physics techniques. Seven currently operational collider facilities are described and discussed in Sec. III. The next generation of colliders, which are believed to be technically feasible and affordable and which could be constructed over the next two or three decades, is the subject of Sec. IV. Finally, in Sec. V we assess opportunities offered by emerging accelerator technologies and attempt to look beyond the current horizon and outline possible changes in the collider paradigm that might enable distant-future, ultimate colliders.

II. DEVELOPMENT OF COLLIDERS

Modern and future colliders are extensively based on the accelerator technology and beam physics techniques developed and appraised by their predecessors. In this section, we introduce and elaborate on major collider issues from a historical perspective. More detailed considerations and comprehensive lists of references were given by Chao *et al.* (2013), Myers and Schopper (2013), and Myers and Brüning (2016).

In an accelerator, charged particles gain energy from an electric field, which usually varies in time at a high frequency ranging from tens of megahertz to tens of gigahertz. The accelerating field gradients in rf cavities are usually orders of magnitude higher than in direct-current (dc) systems; rf cavities are therefore commonly used in colliders. At present, the highest beam accelerating gradients ever achieved in operational machines or beam test facilities are some $G \approx 100$ MV/m in 12 GHz normal-conducting (NC) rf cavities (Senes *et al.*, 2018) and 31.5 MV/m in 1.3 GHz superconducting rf (srf) ones (Broemmelsiek *et al.*, 2018). In a linear-collider arrangement, which is illustrated in Figs. 1(c)–1(e), the beam energy E_b is the following product of the average accelerating gradient G and the length of the linac L:

$$E_b = eGL, \tag{4}$$

where e denotes the elementary electron charge assuming the acceleration of singly charged particles like electrons or

protons. For example, reaching 1 TeV energy requires either 10 km of NC rf accelerator or ~30 km of srf linac, if the rf cavities occupied all available space (which they do not). Cost considerations (discussed later) often call for the minimization of rf acceleration, such as through repeated use of the same rf system, which in that case would boost the energy in small portions $\Delta E_b = eV_{\rm rf}$ per turn every time a particle passes through the total cavity voltage $V_{\rm rf}$. Such an arrangement can be realized both in the form of circular colliders [Figs. 1(a) and 1(b)], which have proven to be extremely successful, and through novel schemes based on ERLs [Fig. 1(f)]. Circular colliders are the most common; here the momentum and energy of ultrarelativistic particles are determined by the bending radius inside the dipole magnets ρ and the average magnetic field B of these magnets

$$p = eB\rho \quad \text{or} \quad E_b\,(\text{GeV}) = 0.3B\rho\,(\text{Tm}). \tag{5}$$

As the particles are accelerated in a *synchrotron*, the strength of the magnetic field is increased to keep the radius of the orbit approximately constant. Such a condition allows the beam orbit to remain inside the limited space provided by the accelerator beam pipe passing through the magnet apertures.

The maximum field of NC magnets is about 2 tesla (T), owing to the saturation of ferromagnetic materials, and while this is sufficient for lower-energy colliders, such as most e^+e^- storage rings, it is not adequate for frontier-energy hadron or muon beams because of the implied need for excessively long accelerator tunnels and prohibitively high total magnet power consumption. The development of SC magnets that employ high electric current-carrying Nb-Ti wires cooled by liquid helium below 5 K, opened up the way toward higher fields and to hadron colliders at record energies (Tollestrup and Todesco, 2008). The latest of these, the 14 TeV c.m.e. LHC at CERN, uses double bore magnets with a maximum field of 8.3 T at a temperature of 1.9 K, in a tunnel of $C = 26.7$ km circumference (dipole-magnet bending radius $\rho = 2800$ m).

A. Basic technologies and beam physics principles

1. Magnets and rf structures

Magnets form the core of all types of colliders. In addition to bending magnets, several other field shapes are required in order to focus and control the beams and manipulate beam polarization. Accelerator magnets typically are long (up to a few meters) and feature transversely small apertures (a few centimeters), which accommodate the beam vacuum pipes. The magnetic field components are normally oriented in the (x, y) plane of the magnet cross section. In such a 2D configuration, the most common representation of the field is given by a complex multipole expansion

$$B_y + iB_x = \sum_{n=1}^{\infty}(B_n + iA_n)(x + iy)^{n-1}, \tag{6}$$

where B_n and A_n represent the normal and skew multipole components of the field, and $2n$ signifies the number of poles. For example, in an ideal horizontally deflecting, normal dipole magnet ($n = 1$), we have $B_y = B_1$ and $B_x = 0$.

For an ideal quadrupole magnet ($n = 2$), the fields are $B_y = B_2 x, B_x = B_2 y$. Thus, this type of magnet can be used as a focusing element, as it deflects a particle proportionally to its transverse offset x or y from the magnet axis. Namely, to first approximation, we have $\Delta x' = Kx$, where $x' \equiv p_x/p_s$ is the slope of the particle trajectory (horizontal momentum p_x divided by longitudinal momentum p_s), $\Delta x'$ is the change in slope after passing through the quadrupole, and K is the normalized strength of a quadrupole of length l, which is given by $K = B_2 l/B\rho$, with the magnetic rigidity $B\rho = p_s/e$.

Higher-order multipole magnets such as sextupoles ($n = 3$) and octupoles ($n = 4$) are also widely used to control an accelerator's chromaticity (the dependence of its focusing property on particle momentum) and for beam stabilization, respectively. Other commonly employed magnets are wigglers and undulators, sequences of short dipole magnets with alternating polarity, which yield a periodic field variation along the beam trajectory, causing the beam to wiggle and to lose energy, emitting electromagnetic radiation (Clarke, 2004). High-field, few tesla solenoids are commonly deployed in collider detectors (Yamamoto and Makida, 2002); solenoid magnets are also used for spin rotation and beam polarization control (Barber *et al.*, 1985), and for the focusing of mostly lower-energy beams, such as in electron coolers (Parkhomchuk and Skrinsky, 2000) and injectors (Carlsten, 1995).

Collider beam dynamics is highly sensitive to magnet field quality, understood as the relative deviation of the actual field from its ideal design value, and requires the unwanted components (B_n, A_n) to be of the level of a few 10^{-4} of the main field (i.e., of the corresponding primary dipole or quadrupole field), and to be even smaller for a few special, strong magnets used to ultimately focus or transversely compress the beams at the collider's interaction points (IPs). In NC magnets, a steel or iron yoke is employed to direct and shape the magnetic field inside the magnet aperture so that the field quality is usually assured by the proper shaping of the magnet poles (Tanabe, 2005). For field levels above 1.7–2.0 T, which are typical for NC magnets, such an approach no longer works. However, significantly higher fields can be obtained with SC magnets. In SC magnets, the iron of the yoke does not play a major role in field formation. Instead, the achievement of the target field quality requires a conductor-coil placement accuracy and position stability of less than a few dozen micron, which is to be obtained while the coil is subjected to enormous magnetic forces, sometimes exceeding 10^6 N per meter of magnet length (Mess *et al.*, 1996); see also Myers and Schopper (2013), Chap. 8.1.

In addition, ramping the SC magnets induces so-called persistent currents inside the superconducting cables, which can result in dangerous systematic sextupole field components of the order of $B_3/(B_1 R_0^{-2}) \sim 20 \times 10^{-4}$ (where R_0 denotes a reference radius for the good field region, typically chosen as about 2/3 of the magnet's aperture) (Tollestrup and Todesco, 2008). These and other time-dependent effects require sophisticated systems of weak, but numerous, corrector magnets, adding to the complexity of collider operation, while assuring its efficiency. There are many other difficulties related to the operation of SC magnets, such as the need for cooling by liquid helium, quench detection and protection, alternating-current (ac) losses, and the careful control of the megajoules to

gigajoules of stored magnetic field energy. All of these have been generally resolved and do not outweigh the major advantages of superconductive systems, namely, a few orders of magnitude lower electric wall-plug power consumption and the ability to generate much higher magnetic fields in Nb-Ti-based magnets of up to 9 T, as demonstrated in the Tevatron (4.5 T), HERA (4.7 T), RHIC (3.5 T), and LHC (8.3 T); see Fig. 4. Even higher fields of up to 12–16 T can be achieved with a Nb_3Sn conductor (Schoerling and Zlobin, 2019), and over 20 T are expected with certain high-temperature superconductors (HTS) (Rossi and Bottura, 2012). We note that the previously cited field values are lower than the critical fields of these materials since the operation of systems of many (hundreds to thousands) accelerator magnets demands significant margins in temperature and critical current to achieve an acceptable stability in an environment characterized by powerful heat sources, due to beams circulating just a few centimeters away from SC coils (irradiation by local beam loss, vacuum pipe heating due to electron-cloud effects and image currents, synchrotron radiation, etc.).

The rf systems of colliders are needed mostly to increase or maintain the particles' energy using time-varying longitudinal electric fields. They typically operate at carefully preselected frequencies $f_{\rm rf}$ in the range of several tens of megahertz to tens of gigahertz and consist of three main elements (power converter, rf amplifier, and rf cavity resonator) together with control loops (low level rf subsystem, including the master oscillator) and ancillary systems: water cooling, vacuum, and cryogenics in the case of srf cavities. The rf system is essentially a device that transforms electrical energy taken from the grid into energy transferred to a beam of particles in three major steps, each with its own technology and efficiency: (1) the transformation of ac power from the electric grid (alternate, low voltage, high current) to dc power [continuous, high voltage (HV), low current] that takes place

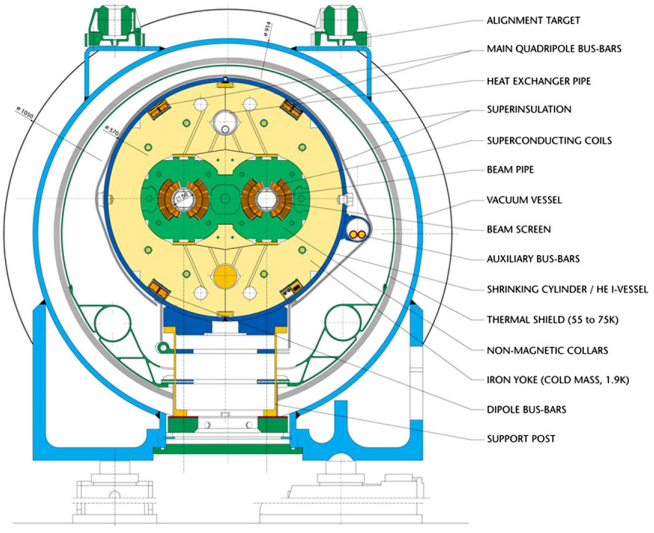

FIG. 4. Cross section of the 14.3-m-long superconducting magnet of the Large Hadron Collider (Evans, 2016). The design field of 8.33 T is vertical and opposite in the two 56 mm diameter bores for the two counterrotating beams, with a horizontal beam-to-beam separation of 194 mm. The LHC comprises 1232 main dipoles, each weighing about 35 tons.. From CERN, 1999.

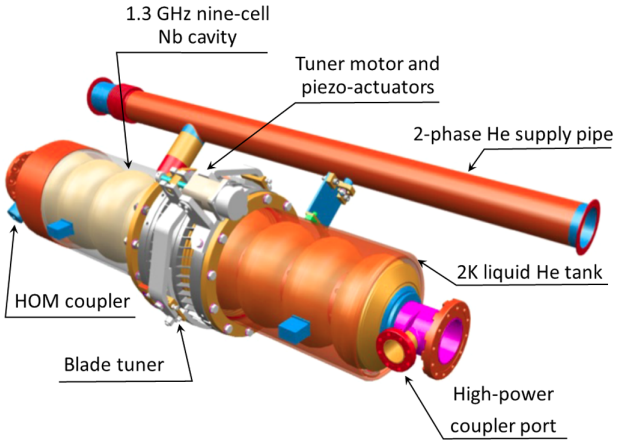

FIG. 5. Baseline superconducting cavity package (dressed cavity) of the International Linear Collider. The titanium helium tank is shown as a transparent display for the 1-m-long nine-cell niobium rf cavity inside. Adapted from Phinney, Toge, and Walker, 2007.

in a power converter with some 90% efficiency; (2) the transformation of the dc power into rf power (high frequency) that takes place in a rf power source: rf tube, klystron, transistor, etc., with efficiency ranging from 50% to 70% or more, depending on the specific device and mode of operation [continuous wave (cw) or pulsed]; (3) transformation of rf power into the particle-beam power gain that takes place in the gap of an accelerating cavity, with efficiencies that may reach 30% or $\geq 50\%$ in a pulsed NC or SC linac (Bailey, 2012) or be approximately 100% in case of a cw srf system for a storage ring. Thanks to cost saving considerations, all these efficiencies have been constantly improving with increasing rf power demands, which for large modern and future colliders can be as high as dozens of or even several hundred megawatts (Delahaye, 2018).

The energy gain of a particle traversing a rf cavity is

$$\Delta E_b = e\int \boldsymbol{E}\boldsymbol{v}dt = eV_{\rm acc}\cos\left(\omega_{\rm rf}t+\phi\right), \tag{7}$$

where $\boldsymbol{E}$, $V_{\rm acc}$, $\omega_{\rm rf}=2\pi f_{\rm rf}$, and ϕ denote the cavity's electric field, accelerating voltage, frequency, and phase, respectively, and $\boldsymbol{v}$ is the particle's velocity, usually parallel to the accelerating field, at the time of passage t. For synchrotrons and storage rings, the condition of synchronicity over subsequent acts of acceleration calls for the rf frequency $f_{\rm rev}$ to be a harmonic of the revolution frequency $f_{\rm rf}=hf_{\rm rev}$, with the integer h known as the harmonic number. For a non-ultra-relativistic particle the rf frequency needs to be increased over the course of acceleration. The rf power supplied to the cavity from the source goes into the increase of beam power P_b and into sustaining an accelerating field that otherwise would decay ($P_{\rm loss}$) due to the finite cavity surface conductivity

$$P_{\rm rf}=P_b+P_{\rm loss}=I_b\Delta E_b+\frac{V_{\rm acc}^2}{2R_s}. \tag{8}$$

Here I_b is the beam current and R_s is the so-called shunt impedance (the resonant resistance of an equivalent RCL

circuit) $R_s = Q(R/Q)$: the product of the rf cavity's quality factor Q, related to the power dissipation on the cavity surface, and a factor R/Q depending only on the cavity geometry. Typical Q values for NC cavities are in the range of 10^4, while they can reach a few 10^{10} in srf cavities (Martinello *et al.*, 2018). The factor R/Q, which is independent of the cavity size and of the surface resistance, is commonly used as a figure of merit; see Padamsee, Knobloch, and Hays (2008). It typically varies between 196 Ω per resonant cell, obtained for a TM_{010} mode pillbox cavity with minimal opening for beam passage, and some 100 Ω per cell for large aperture elliptical cavities, such as those used in srf systems.

The largest linac built to date is a 3-km-long linac at the Stanford Linear Accelerator Center (SLAC), which operated NC copper structures at a frequency of 2.856 GHz (corresponding to a rf wavelength of $\lambda_{\rm rf} = 10.5$ cm). It provided a total of 50 GeV acceleration in one pass, with average gradient $G = \Delta E_b/eL$ of about 21 MV/m (Erickson *et al.*, 1984). Only 80 kW of 10 MW of total rf power went into the power of the two colliding beams $2P_b$ (Lavine, 1992; Phinney, 2000).

Circular colliders are much more efficient due to repetitive energy transfer from rf cavities to beams over many turns, but at the highest energies they face a serious impediment in the form of synchrotron radiation. The latter causes an energy loss per turn of (Sands, 1970)

$$\Delta E_{\rm SR} = \frac{1}{3\epsilon_0}\frac{e^2\beta^3\gamma^4}{\rho}, \tag{9}$$

which increases with the fourth power of energy and scales with the inverse of the bending radius (here ϵ_0 is the permittivity of vacuum and $\beta = \sqrt{1-1/\gamma^2}$). Inserting numerical values for electrons, the energy loss of a particle during one revolution becomes $\Delta E_{\rm SR} = 0.089\ {\rm MeV/turn}$, $E_b^4\ ({\rm GeV})/\rho\ ({\rm m})$. Even for the largest circumference e^+e^- collider LEP with an average bending radius ρ of about 3.1 km, maintaining maximum beam energy at 104.5 GeV required cw operation of the 353.2 MHz rf system with a voltage of $eV_{\rm acc}\cos(\phi_s) = \Delta E_{\rm SR} = 3.4$ GeV per turn, to compensate for about 23 MW total synchrotron-radiation beam power loss (Brandt *et al.*, 2000). Adequately, the final LEP rf system consisted of 272 superconducting Nb sputter-coated Cu cavities and 16 solid Nb cavities, with an average gradient of $G = 5$ to 6 MV/m, and 56 lower voltage normal-conducting Cu cavities, with a gradient of 1.5 MV/m, together provided a maximum total rf voltage of $V_{\rm acc} = 3.63$ GV. In the last year of LEP operation the 288 srf cavities were powered by 36 klystrons with an average power of 0.6 MW each (Brown *et al.*, 2001; Assmann, Lamont, and Myers, 2002). The pure rf-to-beam-power efficiency was $\eta \approx 100\%$. An effective "rf-to-beam-power efficiency" of about 75% was computed by taking into account the additional cryogenic power needs resulting from both rf-related heating and static heat load of the cryostat, in conjunction with the low cooling efficiency at cryogenic temperature (Weingarten, 1996). Adding ac-to-dc conversion and LEP klystron efficiencies (Butterworth *et al.*, 2008) plus waveguide losses, the total wall-plug-to-beam-power efficiency, including cryogenics, was close to 50%.

Besides beam acceleration, rf systems are employed for various other beam manipulations, such as longitudinal bunching, bunch compression, splitting, coalescing, and flattening (Minty and Zimmermann, 2013) and, in some cases, to provide a time-varying transverse deflection to particle bunches in *crab cavities* for linear and circular colliders (Palmer, 1988; Oide and Yokoya, 1989; Sun *et al.*, 2009), as streaking devices for time-varying diagnostics (Akre *et al.*, 2002), and for bunch separation or bunch combination, including as rf deflectors in the drive-beam complex of the proposed Compact Linear Collider (CLIC) and the former CLIC Test Facility 3 (Marcellini and Alesini, 2004).

Synchrotron-radiation power of protons is smaller than for electrons by a significant factor $(\gamma_p/\gamma_e)^4 \propto (m_e/m_p)^4 \approx 1.3\times10^{-13}$ at the same energy [see Eq. (9)], but it can still become a significant concern in the highest-energy, high-current SC accelerators like the LHC. The reason is that synchrotron radiation leads to heating and outgassing of the beam vacuum pipe. The former poses problems for the cryogenic system of the SC magnets, while the latter may impede attainment of vacuum gas pressures of 1–10 ntorr or better, which are needed to guarantee sufficiently long lifetimes of the continually circulating beams. These technological challenges have been successfully resolved in modern colliding-beam facilities; see Barron (1985), Lafferty (1998), and Myers and Schopper (2013), Chaps. 8.3 and 8.5.

For many modern colliders, especially for hadron and linear colliders, the costs of core accelerator components, magnets, and rf structures dominate construction costs, followed by the costs for tunnels, electric power infrastructure, and auxiliary systems for ultrahigh vacuum, cryogenics, beam control, and stabilization, among others. The growing demands for higher-energy beams have motivated a large segment of the accelerator community to search for, and to develop, new cost-effective technological concepts and approaches.

2. Beam dynamics

Given the enormous and highly concentrated power carried by high-energy particle beams, the main concern of beam dynamics in colliders is stability. We now introduce major physics phenomena affecting the dynamics of individual particles in accelerators, of single high-intensity beams of many particles moving together, and of colliding beams. Comprehensive definitions and explanations of these subjects were given by Edwards and Syphers (2008), Chao, Mess *et al.* (2013), Peggs and Satogata (2017), and Lee (2018).

While a reference particle proceeds along a design trajectory (reference orbit) mostly determined by transverse magnetic dipole fields, other particles in the bunch are kept close by through the focusing effect of quadrupole fields. Generally following Edwards and Syphers (2008), we assume that the reference particle carries a right-handed Cartesian coordinate system, with the comoving z coordinate pointing in the direction of motion along the reference trajectory $z = s - vt$ (with v the reference particle velocity and t time). The independent variable is the distance s of the reference particle along this trajectory, rather than time t, and for simplicity this reference path is taken to be planar. The transverse coordinates

are x (horizontal) and y (vertical), where $\{x, z\}$ defines the plane of the reference trajectory.

Several timescales are involved, and this is reflected in the approximations used in formulating the equations of motion. All of today's high-energy colliders are alternating gradient synchrotrons (Chao *et al.*, 2013) and their shortest timescale is set by so-called betatron oscillations. The linearized equations of motion of a particle displaced from the reference trajectory are

$$\begin{aligned} x'' + K_x x = 0, \quad \text{with} \quad K_x \equiv \frac{e}{p}\frac{\partial B_y}{\partial x} + \frac{1}{\rho^2}, \\ y'' + K_y y = 0, \quad \text{with} \quad K_y \equiv -\frac{e}{p}\frac{\partial B_y}{\partial x}, \\ z' = -x/\rho, \end{aligned} \tag{10}$$

where the magnetic field $B_y(s)$ in the (x, z) plane is only in the y direction, contains only dipole and quadrupole terms, and is here treated as static in time but s dependent. We take into account the Maxwell equation in vacuum $\nabla \times \boldsymbol{B} = \boldsymbol{0}$ to eliminate $B_x(s)$, using the relation $\partial B_x/\partial y = \partial B_y/\partial x$. The radius of curvature due to the field on the reference orbit is ρ ($\rho = e/pB_y$); p and e are the particle's total momentum and charge, respectively. The prime denotes d/ds.

The equations for x and y are those of harmonic oscillators but with a restoring force periodic in s; that is, they are instances of Hill's equation (Magnus and Winkler, 1979). The solutions are

$$x(s) = \sqrt{2J_x\beta_x}\cos\psi_x, \tag{11}$$

$$x'(s) = -\sqrt{\frac{2J_x}{\beta_x}}[\alpha\cos\psi_x + \sin\psi_x], \tag{12}$$

where the action J_x is a constant of integration, $\alpha_x = \alpha_x(s) \equiv -(1/2)d\beta_x(s)/ds$, and the envelope of oscillations is modulated by the amplitude function β_x, commonly called the *beta function*. A solution of the same form describes the motion in y. The betatron oscillation phase advances according to $d\psi_x/ds = 1/\beta_x$; that is, $2\pi\beta_x$ also plays the role of a local wavelength of oscillations along the orbit. An extremely important parameter is the *tune*, Q_x, which is the number of such oscillations per turn about the closed path

$$Q_x = \frac{1}{2\pi}\oint d\psi_x = \frac{1}{2\pi}\oint \frac{ds}{\beta_x(s)}. \tag{13}$$

While the integer part of the tune $[Q_{x,y}]$ generally characterizes the extent of the focusing lattice, it is the fractional part of the tune Q_x that needs to be well defined and controlled by the machine operators in order to stay away from potentially detrimental resonances, which may occur under conditions of $kQ_x + lQ_y = m$, where k, l, and m are integers. For example, for the LHC a combination of horizontal and vertical tunes, also called the *working point*, equal to $(Q_x, Q_y) = (64.31, 59.32)$ has been selected such that resonances up to the order of $|k| + |l| = 10$ or 12 are avoided (Gareyte, 1999; Persson *et al.*, 2017a). These resonances are driven by high-order multipole components B_n, A_n of the fields in the magnets if $k + l = n$, by self-fields of the beam, or by the electromagnetic fields of the opposite bunch. Normally, the nonlinear components are weak relative to linear ones B_1, B_2, A_2. However, when the nonlinear resonance condition is encountered, the amplitudes of particle oscillations $A_{x,y}$ could grow over the beam lifetime, resulting in the escape of the particles to the machine aperture, an increase of the average beam size, or both; either of these are highly undesirable phenomena. Careful analysis of nonlinear beam dynamics is instrumental in determining and optimizing the *dynamic aperture*, which is defined as the maximum amplitude of a stable particle motion (Wiedemann, 2012).

Neglecting for now all nonlinear effects and considering only the linear dynamics, the beta function is well defined and satisfies

$$2\beta_x\beta_x'' - \beta_x'^2 + 4\beta_x^2 K_x = 4. \tag{14}$$

In a region free of magnetic fields, such as the neighborhood of a collider IP, usually occupied by particle detectors (at high energies the effect of the longitudinal detector solenoid can often be neglected), a symmetric solution of Eq. (14) is a parabola

$$\beta_x(s) = \beta_x^* + \frac{s^2}{\beta_x^*}, \tag{15}$$

where in this case s denotes the longitudinal distance from the IP. The location of the beam waist usually coincides with the IP and corresponds to the minimum value of the beta function β_x^*; the asterisk indicates the IP parameters. A focusing force $K_x(s)$ is needed to prevent the amplitude from growing. In the case of the widely used alternating gradient periodic focusing lattice, consisting of a sequence of equally spaced quadrupoles with a magnetic field gradient equal in magnitude but alternating in sign ("focusing quadrupole—drift space—defocusing quadrupole—drift space," known as a *FODO cell*), Eq. (14) has stable periodic solutions $\beta_x(s)$, $\beta_y(s)$ in both planes provided that the focal length of the quadrupoles is longer than half the lens spacing L, i.e., $f = p/(eB_2 l) > L/2$ (where l is the length of the quadrupole magnet, here assumed to be much shorter than the cell length L). In that case, the amplitude functions have maxima at the focusing quadrupoles and minima at the defocusing ones, e.g., equal to $(2 \pm \sqrt{2})L$ in the case of $f = L/\sqrt{2}$, which corresponds to a betatron phase advance $\Delta\psi_{x,y} = 90°$ per FODO cell.

Expressing J_x in terms of x, x' yields

$$J_x = \frac{1}{2}(\gamma_x x^2 + 2\alpha_x x x' + \beta_x x'^2) = \frac{x^2 + (\alpha_x x + \beta_x x')^2}{2\beta_x}, \tag{16}$$

with $\gamma_x = \gamma_x(s) \equiv [1 + \alpha_x^2(s)]/\beta_x(s)$. In a periodic system, these *Courant-Snyder* parameters (Courant and Snyder, 1958) $\alpha(s), \beta(s), \gamma(s)$ are usually defined by the focusing lattice; in a single pass system such as a linac, the parameters may be selected to match the $x - x'$ distribution of the input beam.

For a given position s in the ring, the transverse particle motion in $\{x, x' \equiv dx/ds\}$ phase space describes an ellipse, the area of which is $2\pi J_x$, where the horizontal action J_x is a constant of motion and is independent of s. If the interior of

that ellipse is populated by an ensemble of noninteracting particles, that area, given the name *emittance*, is constant over the trajectory as well and would change only with energy. In a typical case in which the particle's energy change rate is much slower than the betatron motion, and considering a Hamiltonian system (i.e., a hadron collider or a linear collider, either without synchrotron radiation), the adiabatic invariant $\int p_x dx$ is conserved, and given that for small angles $p_x = x'\beta\gamma mc^2$, it is common practice to consider an energy-independent *normalized emittance* that is equal to the product of the emittance and relativistic factor $\beta\gamma/\pi$ and is denoted by ε_n. For a beam with a Gaussian distribution in $\{x, x'\}$, average action value $\langle J_x \rangle$, and standard deviations σ_x and $\sigma_{x'}$, the definition of the normalized emittance is

$$\varepsilon_{nx} \equiv \beta\gamma\langle J_x\rangle = \beta\gamma\frac{\sigma_x^2(s)}{\beta_x(s)} = \beta\gamma\frac{\beta_x(s)\sigma_{x'}^2(s)}{1+\alpha_x^2(s)}, \tag{17}$$

with a corresponding expression for the other transverse direction y. The angular brackets denote an average over the beam distribution. For 1D Gaussian beam, 95% of the particles are contained within an $\{x, x'\}$ phase-space area of $6\pi\varepsilon_n/\beta\gamma$. Normalized beam emittances are conserved over the acceleration cycle in linear, static focusing lattices $K_{x,y}(s)$, and consequently one would expect the same ε_n at the hadron or linear collider top energy as the one coming from the initial low-energy particle source, such as the duoplasmotron (Brown, 2004; Wolf, 2017) (or photoinjector or damping ring). That is rarely the case, as many time-varying or nonlinear phenomena come into play; some of the more important ones are discussed in Sec. II.A.3.

In an e^-/e^+ storage ring, the normalized emittance is not preserved during acceleration, but at each energy the beam's equilibrium emittance is determined by the effect of synchrotron radiation as a balance between radiation damping and quantum excitation (Sands, 1970). In this case, for a constant accelerator optics, the normalized emittance increases with the third power of the beam energy.

As for the description of a particle's longitudinal motion, one takes the fractional momentum deviation $\delta p/p$ from that of the reference particle as the variable conjugate to z. The factors $K_{x,y}$ and ρ in Hill's equations (10) are dependent on momentum p, leading to a number of effects: first, the trajectory of off-momentum particles deviates by $\Delta x(s) = D_x(s)(\delta p/p)$, where the *dispersion function* $D_x(s)$ is determined by the magnetic lattice and is usually positive, periodic, and of the order of $\sim\rho/Q_x^2$. Second, the radius of curvature and orbit path length C vary with the momentum and to first order are characterized by the *momentum compaction factor* α_c

$$\alpha_c \equiv \frac{\Delta C/C}{\delta p/p} = \frac{1}{C}\oint\frac{D_x(s)}{\rho(s)}ds. \tag{18}$$

Energy deviations also result in changes of machine focusing lattice properties and variations of the particle tunes, characterized by the chromaticity $Q_{x,y}' = \Delta Q_{x,y}/(\delta p/p)$. The natural chromaticity due to energy dependence of the quadrupole focusing is large and negative ($\sim -Q_{x,y}$). Corresponding chromatic tune variations, even for relatively small energy deviations $\delta p/p \sim 10^{-4}$–10^{-3}, can become unacceptably large. To assure transverse particle stability, the chromaticity is usually partially or fully compensated for by additional sextupole magnets placed at locations of nonzero dispersion.

In the s direction rf electric fields [Eq. (7)] provide a longitudinal focusing effect. This is also known as the *phase stability principle*, which historically was important for the development of the synchrotron concept (Veksler, 1944; McMillan, 1945). The frequency f_s of such longitudinal *synchrotron oscillations* is (expressed in units of revolution frequency $f_{\rm rev}$ to become the *synchrotron tune* Q_s)

$$Q_s \equiv \frac{f_s}{f_{\rm rev}} = \sqrt{\frac{(\alpha_c - 1/\gamma^2)heV_{\rm acc}\sin(\phi_s)}{2\pi\beta cp}}, \tag{19}$$

where h again denotes the rf harmonic number. The synchrotron tune Q_s determines the amplitude of longitudinal oscillations for a particle with an initial momentum offset $\delta p/p$ via

$$\Delta z = \left(\frac{\delta p}{p}\right)\frac{E_b Q_s}{eV_{\rm acc}h}C. \tag{20}$$

As in the case of transverse oscillations, the area of the longitudinal phase space $\{\Delta E, \Delta t\}$, or $\{\gamma\beta mc\delta p/p = (mc/\beta)\Delta\gamma, z = \beta c\Delta t\}$, encircled by a moving particle is an adiabatic invariant, and the corresponding normalized longitudinal emittance proportional to the product of rms bunch length σ_z and rms momentum spread $\varepsilon_{n,L} = \beta\gamma mc\sigma_z(\delta p/p)$ is a generally conserved quantity in hadron accelerators and also in linear accelerators. In the case of lepton storage rings, synchrotron radiation determines the relative momentum spread, which grows with the square of the beam energy (Sands, 1970), and the corresponding bunch length follows from Eq. (20). In hadron synchrotrons, the longitudinal emittance is often intentionally blown up during acceleration so as to preserve longitudinal beam stability (Baudrenghien *et al.*, 2011).

Longitudinal oscillations are the slowest of all the periodic processes that take place in the accelerators. For example, in the LHC, the frequency of synchrotron oscillations at the top energy of 7 TeV is about $f_s = 23$ Hz, the revolution frequency is $f_{\rm rev} = 11.3$ kHz, the frequency of betatron oscillations is about $Q_{x,y}f_{\rm rev} = 680$ kHz, and the rf frequency is $f_{\rm rf} = 400.8$ MHz ($h = 35\,640$).

We note that longitudinal motion is practically absent in linacs. In the absence of bending dipoles, dispersion $D_x(s)$ is zero and so are the momentum compaction factor α_c and the synchrotron tune Q_s. As a result, in a linac ultrarelativistic particles barely change their relative positions during acceleration despite significant energy spread; see Eq. (20).

3. Beam dynamics impediments to and evolution of luminosity

For further discussion, the basic equation (3) for luminosity is now rewritten in terms of the normalized transverse emittances (17) and the amplitude functions β^* at the IP as

$$\mathcal{L} = f_0 \gamma n_b \frac{N^2}{4\pi\varepsilon_n \beta^*} H\left(\frac{\sigma_z}{\beta^*}, \theta_c\right). \tag{21}$$

Here f_0 signifies either the repetition rate of a linear collider or $f_{\rm rev}$ of a circular one; for simplicity we assume equal bunch populations N in two Gaussian beams with n_b bunches each, with equal and round cross sections at the IP $\varepsilon_{nx} = \varepsilon_{ny} = \varepsilon_n$, $\beta_x^* = \beta_y^* = \beta^*$, with $\sigma_x^* = \sigma_y^* = \sqrt{\beta^* \varepsilon/\beta\gamma}$. The numerical factor $H \leq 1$ accounts for geometrical reduction in luminosity (Hirata, 1995) due to the finite bunch length with respect to β^* and due to a crossing angle at the IP θ_c. The former, also referred to as the *hourglass effect*, is caused by the increase in transverse beam sizes as one proceeds away from the IP, where $\beta(s)$ grows parabolically, as in Eq. (15). Thus, for round beams, the hourglass effect lowers the contribution to luminosity from such locations by

$$H\left(\frac{\sigma_z}{\beta^*}, \theta_c = 0\right) = \sqrt{\pi} A \exp(A^2) \mathrm{erfc}(A), \tag{22}$$

where $A = \beta^*/\sigma_z$ (Lee, 2018), and also leads to a harmful modulation of the beam-beam tune shift (discussed later) at twice the synchrotron frequency.

In the case of a nonzero crossing angle, assuming small A the factor H is given by (Napoly, 1993)

$$H\left(\frac{\sigma_z}{\beta^*} \ll 1, \theta_c\right) = \frac{1}{[1 + \sigma_z^2 \tan^2(\theta_c/2)/\sigma^{*2}]^{1/2}}. \tag{23}$$

The factor H rarely drops below 0.5 for the majority of colliders, unless it is specifically required by physics processes under study, such as that given by Bogomyagkov *et al.* (2018). Thanks to the additional focusing effect due to the high-intensity opposite beam during the beam-beam collision, the factor H can also be enhanced by a factor of up to 2 [*dynamic beta* along with *dynamic emittance* effects in circular colliders (Chao, 1985; Furman, 1994; Otboyev and Perevedentsev, 1999), and "disruption enhancement" in linear colliders (Yokoya and Chen, 1992)].

To achieve high luminosity, one has to maximize the total beam populations $n_b N$ with the lowest possible emittances and make the beams collide at high frequency at locations where the focusing beam optics provides the lowest possible values of the amplitude functions β^*, via the *low-beta insertions* (Robinson and Voss, 1966). The latter requires sophisticated systems of strong focusing elements, sometimes occupying quite a significant fraction of the collider's total length (Levichev, 2014). The lowest achievable β^* is determined by the maximum field gradients and apertures in the interaction region (IR) magnets and the effectiveness of compensation of chromatic and nonlinear aberrations. The quest for maximum intensities and lowest emittances is limited by a number of important and often interdependent effects that affect either incoherent single particle dynamics or the dynamics of the beam as a whole (coherent effects).

Examples of incoherent effects are particle losses caused by scattering at a large angle or with a large energy loss so that either the particle's amplitude $\sqrt{2J_{x,y}\beta_{x,y}(s)}$ or its dispersive position deviation $\Delta x = D_x(s)(\delta p/p)$ physically exceeds the available transverse aperture, usually set by collimators (otherwise set by the vacuum chamber and magnet apertures). This can be due to residual vacuum molecules near the beam orbit or Compton scattering off thermal photons (Telnov, 1987), due to Coulomb scattering on other particles within the same bunch (*Touschek effect*) (Bernardini *et al.*, 1963), or due to collisions with opposite beam particles and fields, such as inelastic interaction of protons, Bhabha scattering $e^+e^- \to e^+e^-$, and radiative Bhabha scattering $e^+e^- \to e^+e^-\gamma$; see Chao *et al.* (2013), Chap. 3.

Particles can also get lost on the aperture as a result of much slower mechanisms of diffusion caused either by the previously mentioned processes with smaller scattering amplitudes, but stochastically repeated many times, such as multiple Coulomb *intrabeam scattering* (Bjorken, 1983; Piwinski, 1988; Piwinski, Bjorken, and Mtingwa, 2018), by external noises such as ground motion and magnetic field fluctuations (Levedev *et al.*, 1994), or via chaotic mechanisms like Arnold diffusion, modulational diffusion, and resonance streaming in nonlinear fields, enhanced by minor tune modulations (Zimmermann, 1994). Diffusion is characterized by the action-dependent coefficient $D(J) = D(J_x, J_y)$ and leads to a slow evolution of the beam distribution function $f(J_{x,y}, t)$ according to the diffusion equation

$$\frac{\partial f}{\partial t} = \frac{\partial}{\partial t}\left(D(J)\frac{\partial f}{\partial J}\right), \tag{24}$$

and, consequently, to a change (normally an increase) in the average action $\langle J \rangle$. For an ensemble of particles, the corresponding beam emittance growth is given by

$$\frac{d\varepsilon_n}{dt} = \beta\gamma \frac{dD(J)}{dJ} - \frac{\varepsilon_n}{\tau_{\rm cool}} \tag{25}$$

where the additional second term accounts for the *beam cooling* or damping of particle oscillations. This term appears in the presence of a reaction force opposite to particle momentum if, on average, the corresponding dissipative particle energy loss is compensated for by external power (Skrinsky and Parkhomchuk, 1981; Parkhomchuk and Skrinsky, 2008).

In the case of electron or positron storage rings, such cooling occurs naturally due to synchrotron radiation [Eq. (9)], and it fully determines equilibrium emittance according to Eq. (25) through a balance between radiation damping and excitation of oscillations by random radiation of individual photons (Sands, 1970; Wiedemann, 2003). Four other methods of beam cooling have been developed and successfully employed to attain low emittances, namely, *electron cooling* (Budker, 1967; Parkhomchuk and Skrinsky, 2000; Nagaitsev *et al.*, 2006; Kayran *et al.*, 2019, 2020) and *stochastic cooling* of heavy particles (ions and antiprotons) [see van der Meer (1985), Litvinenko and Derbenev (2009), and Lebedev and Shiltsev (2014), Chap. 7], *laser cooling* of ion beams (Schröder *et al.*, 1990; Hangst *et al.*, 1991; Lauer *et al.*, 1998), and, in a proof-of-principle experiment, the *ionization cooling* of muons (Budker, 1970a; Neuffer, 1983; Adams *et al.*, 2019).

The most prominent coherent effects arise from electric and magnetic forces of the opposite bunch at the IPs, characterized by a dimensionless beam-beam parameter

$$\xi_{x,y} = \frac{r_0 N \beta^*_{x,y}}{2\pi\gamma\sigma^*_{x,y}(\sigma^*_x + \sigma^*_y)}, \tag{26}$$

where $r_0 = e^2/4\pi\varepsilon_0 mc^2$ is the classical radius of the colliding particle (with charge e and mass m) (Chao, 1985). The beam-beam parameter is roughly equal to the betatron tune shift experienced by small amplitude particles: positive in the case of opposite charge beams like e^+e^-, and negative for same charge beams as in pp collisions (Pieloni and Herr, 2013). It also describes the maximum angular beam-beam kick experienced by particles at the IP, which, in the case of round beams, is given by $\Delta x'_{\max} \approx 0.9(4\pi\xi)(\sigma^*/\beta^*)$, with $\xi = r_0 N/4\pi\varepsilon_n$, and occurs at $x \approx 1.6\sigma^*$ (Shiltsev, 1996). As seen in Fig. 6, electromagnetic fields of a Gaussian beam 1 present a nonlinear lens to particles of the opposite beam 2, resulting in changes to the transverse tunes of these particles in beam 2 by an amount varying between ξ in the core and 0 for particles with large amplitudes experiencing minimal beam-beam force.

Beam-beam forces can lead to coherent effects, such as unstable beam oscillations (Dikanskij and Pestrikov, 1982; Chao and Ruth, 1985; Yokoya *et al.*, 1989; Alexahin, 1998) or a blowup of one beam's size while the other beam remains small or even shrinks (the beam-beam *flip-flop* effect) (Krishnagopal and Siemann, 1991; Otboyev and Perevedentsev, 1999). In addition, the tune spread arising from ξ and the nonlinear nature of beam-beam interactions results in strong diffusion along high-order transverse resonances $k\nu_x + l\nu_y = m$ and, ultimately, in beam-size growth and beam losses. Accordingly, it was concluded operationally that the aforementioned effects are tolerable below certain *beam-beam limit* of $\xi_{x,y} \approx 0.003$–0.012 in hadron colliders (Shiltsev *et al.*, 2005). Thanks to strong synchrotron-radiation damping, the beam-beam limit is about an order of magnitude larger in e^+e^- colliders, with maximum $\xi_{x,y} \approx 0.03$–0.12 (Seeman, 1986).

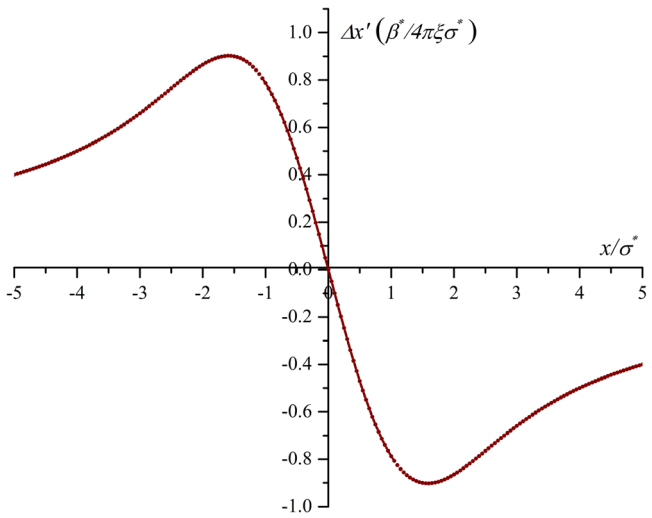

FIG. 6. Angular kick due to beam-beam force.

From Eqs. (21) and (26), one notes that the path to higher luminosity via higher beam intensity and smaller beam size almost automatically calls for a higher beam-beam parameter as $\mathcal{L} \propto \xi$. Several methods have been implemented over the decades to get around the beam-beam limit, including (a) carefully choosing working tunes (Q_x, Q_y) away from the most detrimental resonances; b) operation with flat bunches [wide in the horizontal plane and narrow in the vertical; see Eq. (26)]; (c) more recently, compensation of the beam-beam effects using *electron lenses* (Shiltsev *et al.*, 2007; Fischer *et al.*, 2015; Shiltsev, 2016); (d) reduction of the strength of the beam-beam resonance in the *round beam* scheme with strongly coupled vertical and horizontal motion (Danilov *et al.*, 1996; Young *et al.*, 1998; Berkaev *et al.*, 2012; Shatunov *et al.*, 2016); and (e) by using the *crab-waist* collision method, which beneficially modifies the geometry of colliding bunch profiles only at the IPs so as to minimize the excitation of harmful resonances (Raimondi, 2006; Raimondi, Shatilov, and Zobov, 2007; Zobov *et al.*, 2010).

The focusing of the beams during the collision changes the beam optics, especially for low-amplitude particles. With a properly chosen working point, e.g., just above the half integer resonance in the case of e^+e^- collisions with a single IP, this leads to a reduction of the effective beta function at the collision point, the dynamic beta effect (Chao, 1985; Furman, 1994). In circular e^+e^- colliders, this optics change in collision, propagating all around the ring, also modifies the equilibrium horizontal emittance, which is known as dynamic emittance (Hirata and Ruggiero, 1990; Otboyev and Perevedentsev, 1999). The net IP beam sizes then follow from the combined change of β^* and ε_x. Parameters are normally chosen so that the overall dynamic effect increases the luminosity.

In linear colliders, where each bunch collides only once, with typically much smaller beam size and experiencing much stronger forces, the strength of the collision is measured by the ratio of the rms bunch length σ_z to the approximate linear, thin-lens beam-beam focal length. This ratio, called the disruption parameter D_y (Yokoya and Chen, 1992), is related to ξ_y via $D_y = 4\pi\sigma_z\xi_y/\beta^*_y$. Significant disruption leads to effectively smaller beam size and a resulting luminosity enhancement; it also makes the collision more sensitive to small offsets, resulting in a *kink instability*. Additional beam-beam effects arising in the collisions at linear colliders are the emission of *beamstrahlung* (synchrotron radiation in the field of the opposing beam), along with e^+e^- pair creation and depolarization by various mechanisms (Yokoya and Chen, 1992).

Self-fields of an ultrarelativistic beam are such that the electric force F_E and magnetic force $F_M = -\beta^2 F_E$ on its own particles effectively cancel each other out. This is not the case at $\gamma = (1-\beta^2)^{-1/2} \sim 1$ in the low-energy machines of the injector chain of colliders, where, similar to beam-beam phenomena, the beam's own forces set the limit on the *space-charge tune shift* parameter:

$$\Delta Q_{\mathrm{SC}} = \frac{r_0 N}{4\pi\beta\gamma^2\varepsilon_n}. \tag{27}$$

For most rapid-cycling proton synchrotrons $\Delta Q_{\mathrm{SC}} \leq 0.2$–$0.3$ (Weng, 1987; Reiser, 2008; Hofmann, 2017). Space-charge effects at injection usually also determine the ultimate beam phase-space brightness N/ε_n at top energy.

With the single-bunch brightness set by either space-charge or beam-beam limits, further increases in luminosity require an increase in the number of bunches $\mathcal{L} \propto n_b$. The beams need to be separated in all but a few head-on IPs; otherwise multiple $2n_b$ collision points would immediately lead to unacceptable total beam-beam tune shift parameters $\xi = 2n_b\xi_{x,y}$. Such separation can be implemented either by the use of HV electrostatic separators in single-aperture proton-antiproton colliders as in the Tevatron ($n_b = 36$) or by having an independent aperture and two magnetic systems for each beam as in RHIC ($n_b = 111$), most modern e^+e^- colliders ($n_b = 1584$ in SuperKEKB), or in the LHC ($n_b = 2808$). In the last cases, by necessity, certain regions exist near the main IPs, where the colliding beams have to join each other in a common vacuum chamber; here a significant number of parasitic long-range beam-beam interactions between separated bunches can still take place. These parasitic collisions may produce significant, sometimes dominant, effects on beam dynamics. The separation of the two beam orbits, typically by at least $\sim 9\sigma_{x,y}$, allows troublesome operational issues to be avoided. Other complications of beam-beam interactions can result from the fact that bunch dimensions at the IPs are not always the same between the two colliding beams or between vertical and horizontal planes or that beam intensities are sometimes significantly mismatched. Despite many advances and inventions, beam-beam effects remain one of the most critical challenges, setting a not yet fully resolved limit on the performance of all colliders.

Higher luminosities within beam-beam limits are possible via an increase of the total beam current $I_b = ef_0n_bN$. Three major related difficulties include growing rf power demands in synchrotron-radiation dominated e^+/e^- beams, the advent of so-called coherent (or collective) beam instabilities, and growing demands for minimization of radiation due to inevitable particle losses. Many types of single-bunch and multibunch instabilities (Chao, 1993; Ng, 2006) are caused by beam interactions with electromagnetic fields induced by the beam itself due to the *impedance* of the vacuum chambers and rf cavities (Heifets and Kheifets, 1991; Kheifets and Zotter, 1998) or caused by unstable clouds of secondary particles, like electrons or ions, which are formed around the circulating beams (Ohmi, 1995; Raubenheimer and Zimmermann, 1995; Zimmermann, 2004; Flanagan *et al.*, 2005). These instabilities can develop as quickly as within tens to thousands of turns and need to be controlled. Mechanisms that are routinely employed to avoid coherent instabilities include the use of nonlinear magnets to generate sufficient spread of the tunes and, therefore, provide *Landau damping* (Courant and Sessler, 1966; Métral, 1999), fast beam-based transverse and longitudinal feedback systems (Karliner and Popov, 2005; Burov, 2016), and electron or ion clearing [either by weak magnetic or electric fields or by modulation of the primary beam current profile, rendering secondaries unstable, or by reducing the yield of secondary electrons via either special coating or extensive "beam scrubbing" of the vacuum chamber walls (Kulikov *et al.*, 2001; Fischer *et al.*, 2008; Yin Vallgren *et al.*, 2011; Dominguez *et al.*, 2013)]. To provide acceptable detector background and to avoid quenches of SC magnets and damage or excessive irradiation of accelerator components so that these remain accessible for maintenance in the tunnel, sophisticated collimation systems are utilized. These systems usually employ a series of targets or *primary collimators* (which scatter the halo particles) and numerous absorbers (sometimes as many as 100, which intercept particles in dedicated locations) (Von Holtey, 1987; Mess and Seidel, 1994; Schmidt *et al.*, 2006; Mokhov *et al.*, 2011). In the highest-energy modern and future colliders, extreme total beam energies n_bNE_b ranging from megajoules to gigajoules and densities reaching many $\mathrm{GJ/mm^2}$ pose one of the biggest challenges for high-efficiency and robust particle collimation; see Valentino *et al.* (2012) and Myers and Schopper (2013), Chap. 8.8. Novel sophisticated techniques like collimation by bent crystals (Mokhov *et al.*, 2010; Scandale *et al.*, 2016) or by hollow electron beams (Stancari *et al.*, 2011) are therefore being developed.

Finally, operation of the colliders with progressively smaller beams brings up many issues relevant to alignment of magnets, vibrations, and long-term tunnel stability (Fischer, 1987; Rossbach, 1987; Parkhomchuk, Shiltsev, and Stupakov, 1993; Sery and Napoly, 1996; Shiltsev, 2010a). Radiation backgrounds in physics detectors necessitate careful designs of the interaction region and of the accelerator-detector interface in high-energy high-luminosity colliders (Mokhov *et al.*, 2012; Boscolo, Burkhardt, and Sullivan, 2017). HEP demands for polarized beam collisions and precise c.m.e. calibration of about $\delta E/E \sim 10^{-5}$ or even $\delta E/E \sim 10^{-6}$ have been largely satisfied by the development of polarized particle sources coupled with sophisticated methods to maintain beam polarization along the acceleration chain, or, for e^+/e^- storage rings, by dedicated spin matching procedures to enable self-polarization, combined with the well-established method of *resonant depolarization* (Derbenev *et al.*, 1978, 1980; Huang *et al.*, 1994; Barber *et al.*, 1995; Bai *et al.*, 2006; Blinov *et al.*, 2009).

B. Past advances of e^+e^- colliders

In the remainder of this section, we present key milestones of past colliders and their major breakthroughs and contributions to accelerator science and technology, as well as to particle physics. Extended reviews were given by Pellegrini and Sessler (1995), Voss (1996), Myers and Schopper (2013), Chap. 10, Sessler and Wilson (2014), Scandale (2014), and Myers and Brüning (2016), Part 2.

Though the trio of the first colliders (AdA at Frascati, Italy, and Orsay, France; VEP-I in Novosibirsk, Russia; and CBX at Stanford) constituted mostly of proof-of-principle machines, they were used for initial studies of QED processes (elastic scattering, single and double bremsstrahlung) at their range of center-of-mass energy $\sqrt{s}$. Technological challenges addressed at these machines included development of nanosecond-fast injector kickers, attainment of an ultrahigh vacuum of about a micropascal or better, and reliable luminosity monitoring and other beam diagnostics. Beam physics advances have included first observations and studies of the

Touschek effect, luminosity degradation due to beam-beam effects at $\xi_{x,y} \sim 0.02$–0.04, complex beam dynamics at nonlinear high-order resonances, and coherent instabilities due to resistive vacuum pipe walls (Bernardini *et al.*, 1963, 1964; Gittelman, 1965; Barber *et al.*, 1966; Budker, 1967; Bernardini, 2004; Levichev *et al.*, 2018).

In the late 1960s to mid 1970s, VEPP-2 in Novosibirsk, Russia (Skrinsky, 2002), ACO in Orsay, France (Marin *et al.*, 1965), and ADONE in Frascati, Italy (Adone Group, 1971), were the first electron-positron colliders with an extended particle-physics program, and they included studies of ρ, ω, and ϕ mesons, two-photon pair production $e^+e^- \to e^+e^-e^+e^-$, and multihadronic events (Balakin *et al.*, 1971; Bacci *et al.*, 1972; Cosme *et al.*, 1972; Kurdadze *et al.*, 1972). With a maximum energy of 2×1.5 GeV, ADONE just missed the discovery of the J/ψ particle (and confirmed its existence later). Beam instabilities, including bunch lengthening at high intensity, were the most important beam effects studied and a longitudinal phase feedback system was developed and installed in ADONE to control them. Measured luminosity was mostly set by the beam-beam limit together with synchrotron-radiation effects, i.e., beam emittances defined by the balance between quantum excitation and radiative damping, and scaled approximately as the fourth power of energy $\mathcal{L} \propto \gamma^4$ (Haissinski, 1969). VEPP-2 and ACO were also the first storage rings in which the buildup of electron spin polarization through synchrotroton radiation (the *Sokolov-Ternov effect*) (Sokolov and Ternov, 1964) could be observed and studied (Baier, 1972).

At the Cambridge Electron Accelerator (CEA) facility, electron and positron beams were collided in a special bypass interaction region with two quadrupole magnet doublets on both sides of the IP, demonstrating for the first time a *low-beta insertion* optics with a small $\beta_y^* \approx 2.5$ cm (Robinson and Voss, 1966), representing almost 2 orders of magnitude of reduction compared to more traditional designs. The CEA also measured an unexpectedly large ratio of the hadronic cross section to the muon cross section in electron-positron collisions $R = \sigma(e^+e^- \to \text{hadrons})/\sigma(e^+e^- \to \mu^+\mu^-)$ at $\sqrt{s}$ above 3 GeV, hinting at a new decay channel via charm quarks (Voss, 1996).

Stanford Positron-Electron Accelerating Ring (SPEAR) at SLAC was productive in particle physics, enabling the codiscovery of the J/ψ meson at $\sqrt{s} = 3.1$ GeV consisting of a charm quark and a charm antiquark (1976 Nobel Prize in Physics, Burton Richter) and discovery of the tau lepton with mass of 1.7 GeV/c^2 (1995 Nobel Prize in Physics, Martin Perl). Transverse horizontal and vertical *head-tail instabilities* were observed at about 0.5 mA of current per bunch and were successfully addressed through a positive chromaticity $Q'_{x,y} > 0$ (Paterson, 1975; Chao, 1993).

Several innovative ideas were tried at the Dispositif de Collisions dans l'Igloo (DCI) and VEPP-2M. The DCI team at Orsay attempted to compensate for beam-beam effects by having four collinear beams $e^+e^-e^+e^-$ of equal size and current at the IP. However, the machine never fulfilled its expectations and the beam-beam limit was not significantly different than with two beams (Orsay Storage Ring Group, 1979; Le Duff *et al.*, 1980) due to higher-order coherent beam-beam instabilities (Derbenev, 1973; Krishnagopal and Siemann, 1991; Podobedov and Siemann, 1995). VEPP-2M at Novosibirsk, Russia, reached a luminosity 2 orders of magnitude above its predecessor VEPP-2, which served for a while as the injector (Tumaikin, 1977). The ring operated at the beam-beam limit $\xi_y \approx 0.05$, and luminosity was thus proportional to beam current,

$$\mathcal{L} = f_0 \gamma \frac{I_b \xi_y}{2 e r_e \beta_y^*} \left(1 + \frac{\sigma_y^*}{\sigma_x^*}\right), \tag{28}$$

as follows from Eqs. (3) and (26). At the VEPP-2M's low energy and high currents, intrabeam scattering played a major role, leading to emittance growth and momentum-spread increase. As a countermeasure, a 7.5 T SC wiggler was used to increase the horizontal emittance and, in parallel, the beam current, and to decrease the damping time, allowing for a higher beam-beam tune shift. As a consequence, a significant gain in luminosity was obtained (Levichev *et al.*, 2018). In addition, over decades of operation, the VEPP-2M team mastered the control of beam polarization; it used the resonant depolarization method (Derbenev *et al.*, 1978) to achieve a beam energy calibration at the level of $\sim 10^{-5}$–10^{-6} and carried out the most precise measurements of the masses of ρ, ω, $K^{\pm}$, and K^0 mesons (Skrinskii and Shatunov, 1989).

A large boost in colliding-beam physics came with the next generation of e^+e^- colliders: DORIS at DESY (Hamburg, Germany) (Nesemann and Wille, 1983), which had started its operation almost simultaneously with SPEAR, the Cornell Electron-Positron Storage Ring (CESR) (McDaniel, 1981), and VEPP-4 in Novosibirsk, Russia (VEPP-4 Group, 1980). Following the 1977 discovery of Υ at the Fermilab fixed-target experiment E288 (Herb *et al.*, 1977), their particle-physics programs were aimed at the b-quark states and decays, B-meson mass and lifetime measurements, $B - \bar{B}$ mixing, and determination of Cabibbo-Kobayashi-Maskawa (CKM) matrix parameters (Bohringer *et al.*, 1980; Finocchiaro *et al.*, 1980; Artamonov *et al.*, 1984; Baru *et al.*, 1992; Patrignani, Pedlar, and Rosner, 2013). DORIS initially started as a two-ring collider with 480 bunches in each ring, but it was soon realized that in such a regime its total current was significantly limited by coherent instabilities due to the impedance of the rf cavities and beam-beam effects in the presence of a vertical crossing angle. DORIS was therefore subsequently converted to a one bunch per beam, single-ring collider with head-on collisions.

The history of CESR spans almost three decades (Berkelman, 2004) and witnessed an impressive increase in luminosity by 2 orders of magnitude thanks to a number of important beam physics and technology advances, including operation with up to 45 bunches per beam in a single ring separated in accelerator arcs by six 3-m-long ± 85 kV electrostatic separators that generated closed-orbit displacements (*pretzels*), weaving back and forth around the ring and allowing the electrons and positrons to simultaneously be stored in the same vacuum chamber without destructive unwanted beam-beam collisions (Rubin, 1989). Single-cell SC rf cavities with damping of detrimental *higher-order modes* (HOMs) excited by the beams (Padamsee, Knobloch, and Hays, 2008; Belomestnykh, 2012) allowed

up to 0.37 A beams of both e^- and e^+ to be stored. Tight vertical focusing with $\beta_y^* = 1.8$ cm was provided by a pioneering combination of permanent-magnet and SC technologies for quadrupole magnets in the interaction region. Over many years, CESR held, and continually improved on, the world record for collider luminosity, from about 3×10^{32} cm^{-2} s^{-1} with nine bunches per beam in the early to mid 1990s to 1.25×10^{33} cm^{-2} s^{-1} with 36 bunches per beam around the year 2000. CESR also studied the possible implementation of a *Moebius ring* collider (Talman, 1995) by colliding round beams with a beam-beam parameter ξ as high as 0.09 (Young *et al.*, 1998).

The next triplet of high-energy colliders was made of 2×23 GeV c.m.e. PETRA at DESY (Voss *et al.*, 1979), 2×15 GeV c.m.e. PEP at SLAC (Helm *et al.*, 1983), and 2×32 GeV c.m.e. TRISTAN at KEK (Japan) (Nishikawa, Ozaki, and Kimura, 1983). PETRA is known for the discovery of the gluon and for QCD studies. The first measurement of the tau lepton lifetime and accurate measurements of B- and D-meson lifetimes were carried out at PEP, while the search for high mass resonances (such as those of the top quark) in TRISTAN was in vain. TRISTAN collided 2×2 bunches in four IPs and was the first large accelerator to extensively use srf technology, with its 104 nine-cell 508 MHz cavities providing a total rf voltage of 0.4 GV (Kimura, 1986). The *transverse mode coupling instability* (TMCI), a sort of single-bunch head-tail instability, was extensively studied at both PETRA (Kohaupt, 1980) and PEP, and effective solutions were found.

The highest-energy lepton colliders ever built were the Stanford Linear Collider (SLC) (Phinney, 2000), running on the Z pole at a c.m.e. of 91 GeV, and the LEP at CERN (Assmann, Lamont, and Myers, 2002), the c.m.e. of which was steadily increased from the Z pole over the WW threshold (160 GeV) to a highest energy of 209 GeV in a search for the then still elusive Higgs boson. The SLC complex is shown in Fig. 7; the LEP tunnel, including later additions for the LHC, is shown in Fig. 8.

The LEP and SLC operated simultaneously in the 1990s and were rivals in tests of the *standard model* of electroweak physics. In the seven years that LEP operated below 100 GeV, it produced around 17×10^6 Z particles (and later, at 160 GeV, some 40 000 $W^\pm$ pairs) collected over four experiments. Accurate determination of the parameters of Z^0 resonance at $\sqrt{s} = 91$ GeV led to a precise measurement of the number of light neutrino families $N_\nu = 2.9840 \pm 0.0082$ (Schael *et al.*, 2006), a value that, in 2019, was later further improved to $N_\nu = 2.9963 \pm 0.0074$ (Janot and Jadach, 2020), and to an

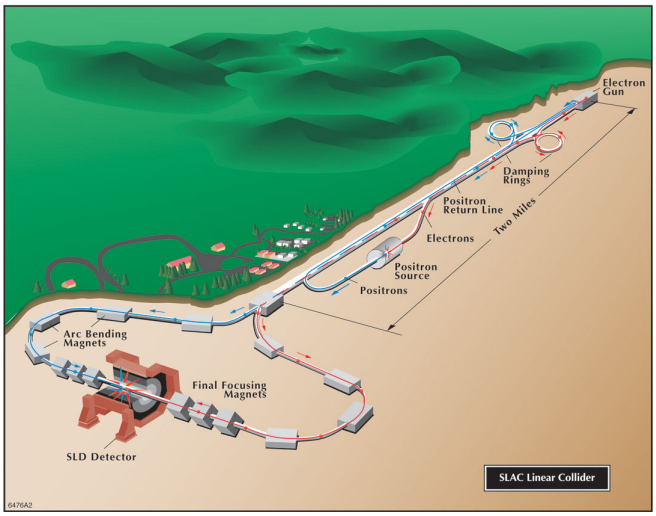

FIG. 7. The Stanford Linear Collider (SLC). Polarized electrons are produced by photoemission from a Ti:sapphire laser and a GaAs photocathode at the electron gun, accelerated to 1.2 GeV, injected into a damping ring (DR) to reduce the e^- beam emittance, kicked back into the 3-km-long linac to be accelerated together with positrons to 46.6 GeV, and then separated magnetically and transported along two arcs and collide head on at the IP. The positrons are produced by a fraction of the 30 GeV e^- beam that is stopped on a target. e^+'s are then collected and returned to the upstream end of the linac for manyfold emittance reduction in another DR.

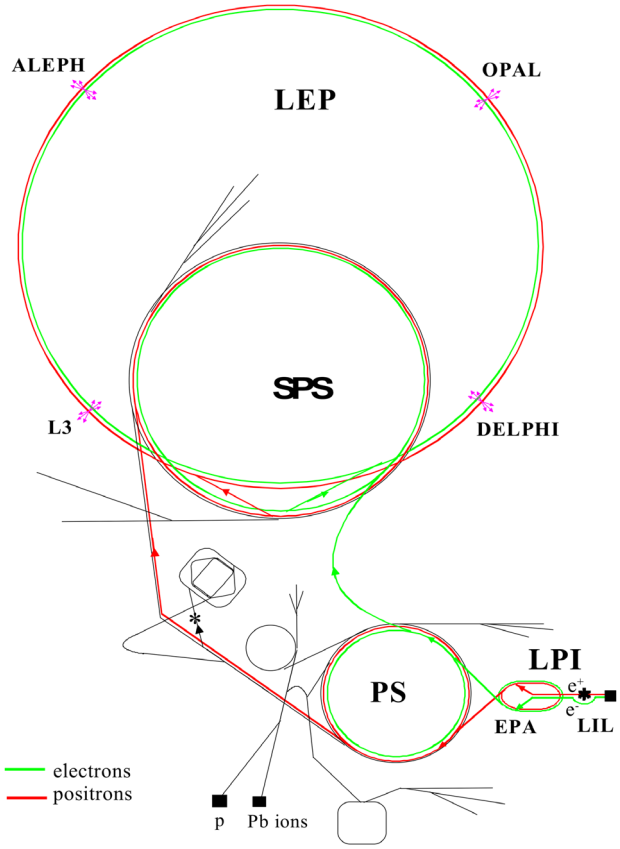

FIG. 8. Schematic view of the LEP injector chain of accelerators and the LEP storage ring (Baudrenghien and Collier, 1996) with the four experiments ALEPH, DELPHI, L3, and OPAL. The first part of the chain of injectors, the LEP preinjector (LPI), consisted of two LEP injector linacs (LILs) and an electron-positron storage ring (EPA). Eight positron bunches, followed by eight electron bunches, were ejected from EPA to the Proton Synchrotron (PS), then accelerated plus extracted to the Super Proton Synchrotron (SPS) for further acceleration. Positrons and electrons were injected into LEP from the SPS, initially at a beam energy of 20 GeV, and later (since 1995) at 22 GeV, to boost the bunch current, which was limited at injection by the TMCI. In its last year of operation (2000), the LEP reached a maximum e^+e^- collision energy of 209 GeV.

indirect determination of the mass of the top quark as $M_t = 173 \pm 23$ GeV. Beam energy calibration with the resonant depolarization method was good to about 0.001%, and the combined error of the resonance scans of 1.9 MeV on m_Z and of 1.2 MeV on Γ_Z were obtained after identifying and correcting for various small, subtle effects, including magnetic field drifts, Earth tides, and ground currents induced by a nearby railway (Assmann *et al.*, 1999; Brandt *et al.*, 2000). The LEP magnets contained little steel so as to provide a relatively small bending field of 1.1 kG needed to circulate 100 GeV particles in a 27 km ring. At the highest energy of operation (beam energy of 104.5 GeV), the synchrotron-radiation loss per turn was some 3% of beam energy. That explains the need for LEP's powerful srf system based on 352 MHz SC niobium-on-copper cavities, which in the last years of operation provided a total rf voltage of about 3.5 GV; see Sec. II.A.1 for further details. Without collisions, at top energy the LEP beam lifetime was limited by the scattering of beam particles off thermal photons (blackbody radiation inside the beam pipe) (Telnov, 1987), a new effect observed for the first time (Dehning *et al.*, 1990). The TMCI (Kohaupt, 1980; Besnier, Brandt, and Zotter, 1984) limited single-bunch current at an injection energy of 20 GeV (later 22 GeV) to about 1 mA. A feedback system to address the TMCI has been proposed and attempted (Danilov and Perevedentsev, 1997). In collision, the luminosity was limited by beam-beam effects at a record high value for the beam-beam tune shift, namely, $\xi_y = 0.083$ per collision point (Assmann and Cornelis, 2000), or $n_{\mathrm{IP}}\xi_y = 0.33$ for the total tune spread.

The SLC (see Fig. 7) was the world's first linear collider of single electron and positron bunches. It operated at a 120 Hz rate and provided 80% longitudinal e^- polarization at the IP coming from a strained GaAs photo gun (Alley *et al.*, 1995). Other accelerator advances at the SLC included the application of *Balakin-Novokhatsky-Smirnov damping* (Balakin, Novokhatsky, and Smirnov, 1983) to suppress the single-bunch beam breakup (Chao, Richter, and Yao, 1980) (a kind of head-tail instability occurring in linear accelerators) and the corresponding emittance growth (Seeman, 1992), a pulse-by-pulse IP position feedback system, implementation of sophisticated nonlinear optics knobs, procedures for the frequent tuning of various IP optics aberrations (Emma *et al.*, 1997; Hendrickson *et al.*, 1999), and a high-efficiency positron source (Clendenin *et al.*, 1988), providing more than 5×10^{12} e^+ per second for injection into the SLC linac (Krejcik *et al.*, 1992). The SLC also pioneered the beam-beam deflection scans for IP beam-size diagnostics (Bambade *et al.*, 1989) and, for the first time, observed beamstrahlung (Bonvicini *et al.*, 1989), i.e., the synchrotron radiation emitted during the collision in the electromagnetic field of the opposing bunch, and exploited it for diagnostics purposes. The SLC also demonstrated a significant increase of luminosity, by more than a factor of 2, due to *disruption enhancement*, i.e., the mutual focusing of the colliding electron and positron bunches at the interaction point (Barklow *et al.*, 1999). During the decade of its operation (1989–1998), the SLC produced close to 600 000 Z bosons (about 3% of LEP production), but with a longitudinally polarized electron beam, allowing the SLC's experiment SLD to perform the world's single most precise measurement of the weak mixing angle $\sin^2\theta_W^{\mathrm{eff}}$ (Abe *et al.*, 2000).

Two particle factories that aimed for precision measurements with luminosities far exceeding those of its predecessors (in particular, CESR) operated during the first decade of the 21st century. These were the two B factories, PEP-II at SLAC (PEP-II Collaboration, 1993) and KEKB at KEK (KEK B-Factory, 1995). They were conceived as asymmetric (unequal energy) two-ring electron-positron colliders, constructed to measure the properties of the b-quark sector, the CP violation, and confirm the CKM matrix (Bevan *et al.*, 2014). The energy of positrons was much lower than that of electrons, so the created B and $\bar{B}$ mesons had significant forward momentum away from the collision point, making it easier for detectors to pinpoint the origin of the B particles'

TABLE II. Design parameters of SuperKEKB (Akai, Furukawa, and Koiso, 2018) compared to past achieved parameters in PEP-II (Seeman *et al.*, 2006; Seeman, 2008b) and KEKB, distinguishing the respective low- and high-energy rings (LERs and HERs). The beam-beam parameter in the table is computed without the hourglass factor or any geometric factors.

Parameter	Unit	PEP-II (achieved)		KEKB (achieved)		SuperKEKB (design)	
Ring		LER	HER	LER	HER	LER	HER
Species		e^+	e^-	e^+	e^-	e^+	e^-
Beam Energy	GeV	3.1	9.0	3.5	8.0	4.0	7.0
Circumference	m	2199		3016		3016	
Horizontal IP beta-function β_x^*	mm	1050	400	1200	1200	32	25
Vertical IP beta-function β_y^*	mm	9–10	9–10	5.9	5.9	0.27	0.30
Horizontal rms normalized emittance ε_{nx}	μm	182	880	123	376	25	63
Vertical rms normalized emittance ε_{ny}	μm	4.8	14	1	3.4	0.07	0.3
Beam current	mA	3213	2069	1640	1190	3600	2600
Bunches per beam		1658		1584		2500	
Bunch current	mA	1.94	1.25	1.04	0.75	1.44	1.04
rms bunch length	mm	10–12	10–12	7	7	6.0	5.0
Full crossing angle	mrad	< 0.05		0 (crab-crossing)		83	
Vertical beam-beam parameter ξ_y		0.047	0.062	0.098	0.059	0.069	0.060
Luminosity	10^{34} cm^{-2} s^{-1}	1.2		2.11		80	

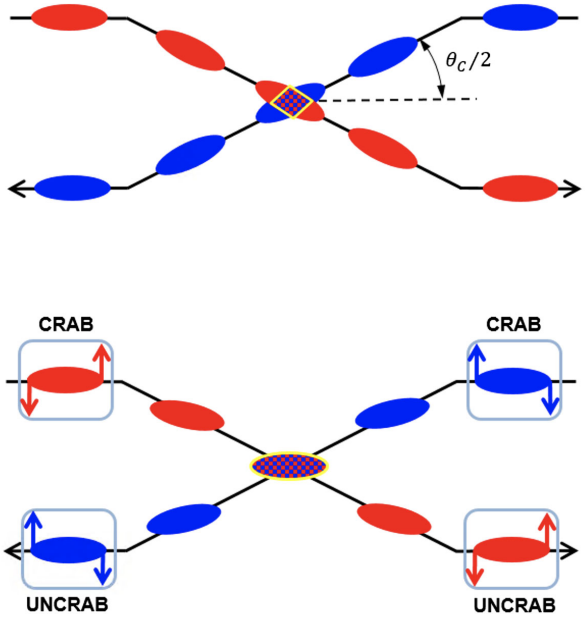

FIG. 9. Top panel: beam collision scheme with crossing angle suffers from geometric luminosity reduction. Bottom panel: crab-crossing scheme that results in full bunch overlapping and thus maximum luminosity. Deflecting rf cavities generate a null kick to the center of the bunch, while its head and tail receive opposite transverse kicks. Adapted from Verdu-Andres *et al.*, 2016.

decay products. Table II presents the beam parameters achieved at these colliders. After a few years of operation, both PEP-II and KEKB introduced a *top-up injection* mode of operation (Satoh, 2010; Seeman, 2015), where small amounts of beam are injected quasicontinually, so as to keep the beam current and luminosity constant over long periods of time, e.g., a day, until the occurrence of a technical failure. The particle detectors remained active and continued data collection during, or shortly after, each beam injection. PEP-II and KEKB had sophisticated transverse and longitudinal bunch-by-bunch feedback systems to suppress coherent instabilities and other measures to allow storage of high currents (Seeman, 2008a; Oide, 2009). PEP-II holds the world record of stored positrons (at 3.2 A) and electrons (at 2.1 A). KEKB set the world record for highest luminosity at 2.1×10^{34} cm^{-2} s^{-1}. KEKB was also the first collider to use srf crab cavities (Oide and Yokoya, 1989) to tilt the bunches at the IP and avoid the geometric luminosity reduction due to the crossing angle θ_c [Eq. (23)]; see Fig. 9. Luminosity improved by a modest 10%–20%; the vertical beam-beam parameter ξ_y increased from 0.06 to 0.09, less than what had been expected from simulations (0.15) (Funakoshi, 2014; Oide, 2014). One possible explanation for the discrepancy is residual nonlinear optics aberrations at the collision point (Funakoshi, 2014).

C. Past advances of hadron colliders

The Intersecting Storage Rings (ISR) at CERN (Johnsen, 1973) was the world's first pp collider. It was made up of two independent, interleaved normal-conducting synchrotron rings intersecting at eight points, five of which were used for experiments. The ISR physics program aimed at achieving an understanding of proton structure at the c.m.e. levels, exceeding the most powerful fixed-target machines of the SPS at CERN and the Main Ring at Fermilab (Giacomelli and Jacob, 1979), both of which were constructed after the start of ISR operation. The machine relied on a process called *momentum stacking* to accumulate record high currents (up to 60 A) and achieved luminosities in hadron collisions surpassed only two decades later (Myers, 2020). The discovery of *Schottky noise* resulting from the discrete nature of particles in the beam led to its extensive use for diagnostics of unbunched (coasting or dc) beams and allowed the first successful demonstration of stochastic cooling and reduction of beam emittances (van der Meer, 1972; Bramham *et al.*, 1975).

S$p\bar{p}$S, the next collider at CERN, was built as a modification of the SPS, with the goal of discovery of the massive neutral intermediate vector bosons (Rubbia, McIntyre, and Cline, 1977), successfully achieved in 1983 (1984 Nobel Prize in Physics, Carlo Rubbia) (Rubbia, 1985). Most critical for the success of the S$p\bar{p}$S was the stochastic cooling of antiprotons (1984 Nobel Prize in Physics, Simon van der Meer), which took place in a specially constructed 3.5 GeV antiproton accumulator ring and allowed accumulation of up to 6×10^{10} $\bar{p}$ per hour (van der Meer, 1985).

The first superconducting synchrotron in history, the Tevatron (Edwards, 1985), was also converted into a $p\bar{p}$ collider in 1985 (Dugan, 1989). It was the highest-energy collider for 25 years and its legacy includes many results for which the high energy of $\sqrt{s} = 1.96$ TeV was decisive, such as the discovery of the top quark in 1995 and precise measurements of the masses of the top quark and W boson (Quigg, 2011b). It was also a pioneering instrument that advanced the frontiers of accelerator science and technology (Holmes and Shiltsev, 2013; Lebedev and Shiltsev, 2014). Its 4.5 T dipole magnets employed Nb-Ti superconducting cable operating at 4.5 K (Tollestrup and Todesco, 2008), requiring what was then the world's largest cryogenic system (Norris and Theilacker, 1989; Fowler, 1990). The antiproton

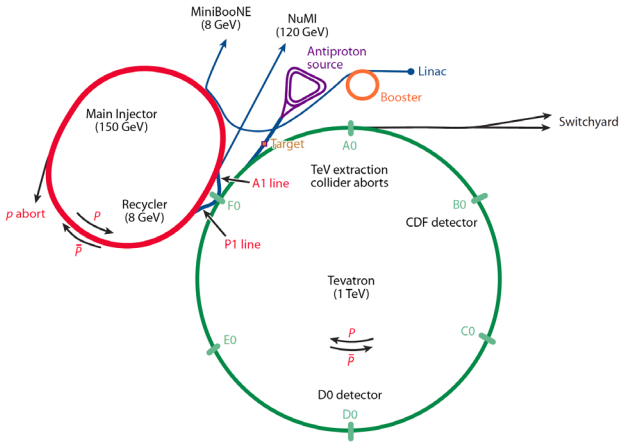

FIG. 10. Layout of the Fermilab accelerator complex. The accelerators are shown to scale; the radius of the Tevatron is 1.0 km. Proton beam energy out of the linac is 400 MeV and 8 GeV out of the Booster synchrotron; the energy of antiprotons in the antiproton source (triangular shaped Debuncher and Accumulator) is also 8 GeV. From Holmes and Shiltsev, 2013.

production complex (Church and Marriner, 1993) consisted of three 8 GeV $\bar{p}$ accelerators (the Accumulator, Debuncher, and Recycler; see Fig. 10), and employed 25 independent stochastic cooling systems and one high-energy electron cooling setup (Nagaitsev *et al.*, 2006) to accumulate up to a record high value of 25×10^{10} $\bar{p}$ per hour. Over the years, some 10^{16} antiprotons have been produced and accumulated at Fermilab (about 17 ng), more than 90% of the world's total man-made production of nuclear antimatter (Shiltsev, 2012b). Despite severe parasitic long-range interactions of the two beams, each consisting of 36 bunches placed on helical orbits by two dozen ± 150 kV HV separators, a total beam-beam tune shift parameter of $n_{\mathrm{IP}}\xi \approx 0.025 - 0.03$ was achieved, a record for hadron beams (Shiltsev *et al.*, 2005). Other notable advances included the first high-energy accelerator built with permanent magnets (the 3.3 km 8 GeV Recycler) (Jackson, 1996), advanced longitudinal beam manipulation techniques of *slip stacking* and *momentum mining* (Koba and Steimel, 2002; Bhat, 2004), and the first operational use of electron lenses (Shiltsev *et al.*, 2008; Shiltsev, 2016) for beam collimation (Zhang *et al.*, 2008; Stancari *et al.*, 2011) and for the compensation of long-range beam-beam effects (Shiltsev *et al.*, 1999, 2007). The Tevatron ultimately achieved luminosities a factor of 430 higher than the original design specification.

D. Past advances of lepton-hadron colliders

The first lepton-proton collider, the 6.4-km-long Hadron-Elektron-Ring-Anlage (HERA) at DESY in Germany (Voss and Wiik, 1994), was the first facility to employ both applications of superconductivity: 5 T magnets in the 920 GeV proton ring and srf accelerating structures to provide about 12 MW of rf power to compensate for synchrotron-radiation losses of 30 GeV lepton beams (positrons or electrons). With proper orbit and optics control, the HERA lepton beam would naturally become transversely polarized to about 60% (within about 40 min) thanks to the Sokolov-Ternov effect (Barber *et al.*, 1994). Special magnets called *spin rotators* were implemented on either side of the collider IPs to produce 30%–45% longitudinal polarization at the experiments (Buon and Steffen, 1986; Barber *et al.*, 1995). HERA operated from 1992 to 2007 at $\sqrt{s}$ of about 320 GeV and luminosities of up to $(3\text{–}5) \times 10^{31}$ cm^{-2} s^{-1} (Willeke, 2006) and allowed the investigation of deep-inelastic and photoproduction processes at then highest-energy scales (Klein and Yoshida, 2008).

III. MODERN COLLIDERS

The colliding-beam facilities of the present utilize many of the advances of past machines to operate at the energy or luminosity frontier, or both. The challenges they face are unique and formidable.

A. Modern e^+e^- colliders

1. VEPP-4M and BEPC-II

Two of the currently operational lepton colliders, VEPP-4M in Novosibirsk and BEPC-II at IHEP (Beijing, China), were constructed in the 1980s (Blinov, 1983; Xu, 1983) but went through a long series of optimizations and upgrades, continually contributing important research in modern particle physics. The Beijing Electron Positron Collider (BEPC) was built as a single-ring collider to produce tau and charm particle physics, but it was later upgraded to a double-ring high-luminosity factory, with up to 2.1 GeV per beam and some 90 bunches. The rf system comprises two SC single cavities at 500 MHz. Longitudinal instability in $\sim$1 A beams originating from high-order modes in the cavities initially limited the luminosity, though this problem was recently resolved through a bunch-by-bunch longitudinal feedback system. The machine reached a record luminosity of 10^{33} cm^{-2} s^{-1} (Qin *et al.*, 2012) at the ψ resonance with $\sqrt{s} = 3.77$ GeV (Chao and Wang, 2008). As of early 2019, the BESIII experiment at BEPC-II finished accumulating a sample of 10^{10} J/ψ events, the world's largest dataset produced directly from e^+e^- annihilations (CERN, 2019b).

The latest of several upgrades of the single-ring VEPP-4M collider operating in a wide beam energy range of 0.92–5.2 GeV is a new injection complex (Emanov *et al.*, 2018) that now comprises a 270 MeV e^- linac, a 510 MeV e^+ linac, injection channels, and a damping ring; this is followed by the 350 MeV to 2 GeV booster-accumulator VEPP-3 ring (which by itself was a e^+e^- collider for a short time in the mid 1970s) (Gaiduk and Pestov, 1976). Single-bunch currents were originally limited to about 7 mA by beam-induced wakefields in the vacuum chambers, but commissioning of the transverse feedback system allowed a manyfold increase to about 25 mA (Blinov *et al.*, 2014). Eight pairs of electrostatic separation plates allow operation of two bunches in the pretzel orbit scheme. Unique to VEPP-4M is its ability to operate over a wide range of energies and precise determination of beam energy using the resonant depolarization method, with a record high absolute accuracy of 10^{-6}. The former is used in studies of two-photon processes such as $\gamma\gamma \to$ hadrons, while the latter allows measurements of the masses of the J/ψ, $\psi(2s)$, and $\psi(3770)$ mesons, and the tau lepton with record accuracy (Aulchenko *et al.*, 2003; Shamov *et al.*, 2009; Anashin *et al.*, 2010).

2. VEPP-2000

Significant innovations in beam physics led to the latest of the Novosibirsk colliders VEPP-2000, which consists of a single ring, with two detectors and twofold symmetry (Shatunov *et al.*, 2000). The VEPP-2000 physics program in the range $\sqrt{s} = 0.3\text{–}2$ GeV includes precise measurements of the total hadronic cross section, exclusive hadronic channels, two-photon physics, tests of higher-order quantum electrodynamics processes, and studies of nucleon form factors at the threshold of the reaction $e^+e^- \to nn,\ pp$ (Shemyakin *et al.*, 2016; Achasov *et al.*, 2017). As in other beam-beam limited machines, the VEPP-2000 luminosity for a fixed machine lattice scales as $\mathcal{L} \propto \gamma^4$. The collider design exploits the *round beam concept* (Danilov *et al.*, 1996), which provides additional stability to particle dynamics, even in the presence of nonlinear beam-beam forces via conservation of angular momentum $M = xy' - yx'$. This scheme requires equal emittances $\varepsilon_x = \varepsilon_y$, equal fractional tunes $Q_x = Q_y$,

equal amplitude functions at the IPs $\beta_x = \beta_y$, and no betatron coupling in the collider arcs. This scheme was implemented in VEPP-2000 by placing two pairs of 13 T superconducting final-focusing solenoids into two interaction regions symmetrically with respect to the IPs (Shatunov *et al.*, 2016). Observations showed that an extremely high beam-beam parameter $n_{\mathrm{IP}}\xi_y = 0.25$ (similar to LEP in the presence of strong radiation damping) was achieved and that round beams led to significant luminosity enhancement (Berkaev *et al.*, 2012; Shatunov *et al.*, 2018).

3. DAΦNE

DAΦNE at Frascati, Italy (Vignola, 1996) was built in the late 1990s to operate at the energy of the ϕ resonance (1.02 GeV c.m.e.), which with high probability decays to K^+K^-, enabling precision measurements of K-meson physics (Ambrosino *et al.*, 2006; Bazzi *et al.*, 2011). In 2008, a new collision crab-waist scheme proved to be effective for decreasing β_y^* without shortening the bunch length, while also reducing the strength of beam-beam resonances at DAΦNE, tripling collider luminosity (Zobov *et al.*, 2010; Zobov, 2016). The crab-waist collision combines a large *Piwinski angle* $\Phi = \sigma_z \tan(\theta_c/2)/\sigma_x^*$ [see Eq. (23)] with the cancellation of the resulting synchro-betatron resonances that occur under conditions of $kQ_x + lQ_y + mQ_s = n$, where k, l, m, and n are integers (Piwinski, 1986) by means of electromagnetic sextupoles with special betatron phase advances to the collision point (Raimondi, 2006; Raimondi, Shatilov, and Zobov, 2007). The crab-waist collision scheme was first proposed in 2006 for the former Italian SuperB project (Raimondi, 2006). Its key concepts and resulting merits (Raimondi, Zobov, and Shatilov, 2008; Zobov, 2013) can be understood by reviewing Fig. 11, which presents two bunches colliding under a horizontal crossing angle θ. The first ingredient is a large Piwinski angle $\Phi \gg 1$,

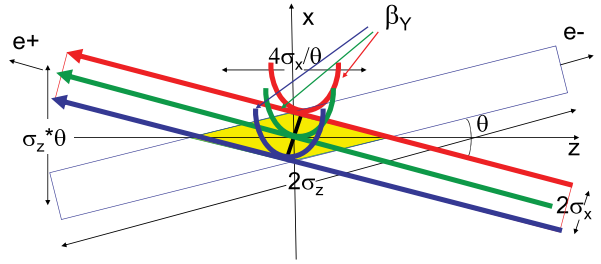

(a) Crab sextupoles OFF

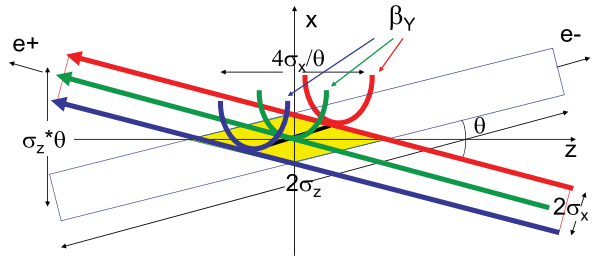

(b) Crab sextupoles ON

FIG. 11. Crab-waist collision scheme. From Raimondi, Zobov, and Shatilov, 2008.

as it had earlier been proposed for hadron colliders (Ruggiero and Zimmermann, 2002). In the crab-waist scheme, Φ is increased by decreasing σ_x^* and increasing θ_c. In this way, the luminosity increases and the horizontal tune shift decreases; the effect of any parasitic collisions around the primary collision point becomes negligible. However, the most important effect is that the overlap area of the colliding bunches is reduced since it is proportional to σ_x/θ_c (see Fig. 11). As a second ingredient, the vertical β function β_y is made comparable to the overlap area size (i.e., $\ll \sigma_z$)

$$\beta_y^* \approx \frac{2\sigma_x}{\theta_c} \cong \frac{\sigma_z}{\Phi} \ll \sigma_z. \tag{29}$$

Reducing β_y^* at the IP yields a luminosity increase at the same bunch current. In addition, if the bunch current is limited by ξ_y (which decreases when β_y^* is lowered), the bunch current can be raised to further push up the luminosity. The vertical synchro-betatron resonances are also suppressed (Pestrikov, 1993). With a finite overlap region, decreasing β_y^* does not require an associated decrease in the bunch length, as would be required in the standard collision scheme because of the hourglass effect. The possibility of a longer bunch length also improves local higher-order-mode heating and any effects of coherent synchrotron radiation. However, implementation of the previously mentioned two ingredients excites new beam-beam resonances, which may strongly limit maximum achievable tune shifts. For this reason, the crab-waist transformation was introduced (Zobov *et al.*, 2010; Zobov, 2016), as a third and final ingredient. As seen in Fig. 11 (bottom panel), the β-function waist of one beam is now oriented along the central trajectory of the other beam. In practice, the rotation of the vertical β function is accomplished by sextupoles placed on both sides of the IP in phase with the IP (modulo π) horizontally and at $\pi/2$ betatron phase difference (modulo π) vertically. The integrated strength $B_3 l$ of these sextupoles should satisfy the following condition, which depends on the crossing angle θ_c and the β functions at the IP (superscript *) and sextupole locations (subscript "sx"),

$$B_3 l = \frac{p}{e}\frac{1}{2\theta_c}\frac{1}{\beta_y^*\beta_{y,\mathrm{sx}}}\sqrt{\frac{\beta_x^*}{\beta_{x,\mathrm{sx}}}}, \tag{30}$$

where e is the particle (electron) charge and p is the design momentum. The main effect of the crab-waist transformation is the suppression of betatron and synchro-betatron resonances arising (in collisions without crab waist) due to vertical tune modulation by horizontal betatron oscillations. The collision of flat beams with $\sigma_y^* \ll \sigma_x^*$ is an essential condition for resonance suppression with the crab sextupoles (Shatilov *et al.*, 2011). The implementation of crab-waist collisions at DAΦNE provided an increase in luminosity by a factor of 3, in good agreement with numerical simulations (Zobov *et al.*, 2009; Shatilov *et al.*, 2011). All ongoing or proposed projects for next-generation circular lepton factories are based on the crab-waist scheme: SuperKEKB, the Super τ-charm factories SCT (Piminov, 2018) and HIEPA (Luo *et al.*, 2019), and finally the Higgs and electroweak factories FCC-*ee* (Bogomyagkov, Levichev, and Shatilov, 2014; Oide *et al.*, 2016; Benedikt *et al.*, 2019a) and CEPC (CEPC Study Group, 2018).

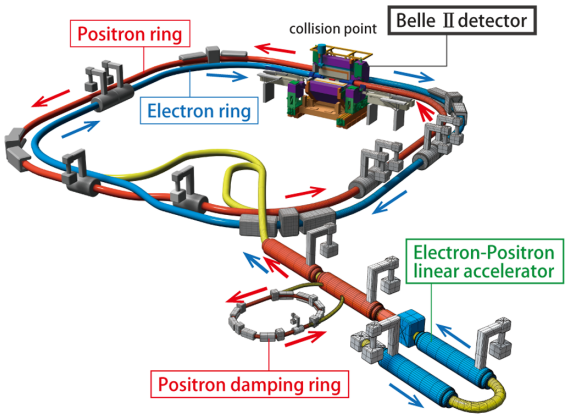

FIG. 12. Schematic of SuperKEKB.

4. SuperKEKB

The SuperKEKB at KEK is an e^+e^- collider with a design peak luminosity of 8×10^{35} cm^{-2} s^{-1} (Ohnishi *et al.*, 2013) (40 times that of the KEKB *B* factory, as previously discussed) at $\sqrt{s}$ close to the mass of the $\Upsilon(4S)$ resonance, making it a second-generation *B* factory for the Belle II experiment (Abe *et al.*, 2010). SuperKEKB is an asymmetric-energy and double-ring collider with a 7 GeV electron ring and a 4 GeV positron ring; see Fig. 12. Its mission is to seek new physics beyond the standard model with a target integrated luminosity of 50 ab^{-1}. Referring to Eq. (28), we find that the luminosity gain of 40 with respect to its predecessor KEKB is achieved with the same beam-beam parameter $\xi_y \approx 0.09$, 2 times higher beam current I_e, order-of-magnitude smaller transverse emittances, and a vertical IP beta function that is 20 times smaller than that of KEKB, namely, $\beta_y^* = 0.3$ mm. The latter realizes the *nanobeam scheme*, so named because the vertical beam sizes at the IP can be squeezed to ~50 nm. The SuperKEKB nanobeam scheme is an adaptation of the original 2006–2007 crab-waist proposal for the Italian SuperB project (Raimondi, Shatilov, and Zobov, 2007) to SuperKEKB. The scheme involves a large horizontal crossing angle between two colliding beams $\theta_x \approx 83$ mrad such that the Piwinski angle is large [$\Phi = \sigma_z \tan(\theta_x/2)/\sigma_x^* \approx 20$], with a bunch length much longer than the beta function at the IP $\sigma_z = 6$ mm $\gg \beta_y^*$ and small horizontal and vertical emittances. Unlike a head-on collision scheme, here the bunches intersect one another only at the short and narrow central parts close to the IP. The first e^+e^- collisions in SuperKEKB occurred in April 2018, eight years after the end of the KEKB operation, and successful collider commissioning is under way (Akai, Furukawa, and Koiso, 2018; Ohnishi, 2018). Since spring 2020, operating with crab-waist collisions, SuperKEKB set a new luminosity world record of 2.4×10^{34} cm^{-2} s^{-1} and reached a world record low β_y^* value of 0.8 mm. The SuperKEKB crab-waist optics has been implemented by detuning the local chromaticity correction sextupoles of the interaction region, as first proposed and developed for the FCC-*ee* design (Oide *et al.*, 2016; Benedikt *et al.*, 2019a); see Sec. IV.B.3.

Table II compares the achieved parameters of PEP-II and KEKB to the design values of SuperKEKB (Akai, Furukawa, and Koiso, 2018).

B. Modern hadron colliders

Two hadron colliders are presently in operation: the RHIC at Brookhaven National Laboratory (BNL) and the LHC at CERN. Both collide either protons (polarized protons in the case of the RHIC) or heavy ions, or protons with ions. For the LHC, a high-luminosity upgrade (HL-LHC) has been approved and will come into operation around 2026. Typical parameters of the RHIC and LHC and design parameters for the HL-LHC are compiled in Table III.

1. RHIC

The RHIC is a double ring that collides heavy ions and/or polarized protons circulating in opposite directions. It is based

TABLE III. Typical proton-proton and heavy-ion parameters of the RHIC and LHC, and design parameters for the HL-LHC upgrade.

Parameter	RHIC		LHC (2018)		HL-LHC (design)	
Species	pp	Au-Au	pp	Pb-Pb	pp	Pb-Pb
Maximum beam energy (TeV)	0.255	0.1/n	6.5	2.72/n	7	2.76/n
Circumference (km)	3.834		26.659		26.659	
Polarization	55%	n/a	n/a	n/a	n/a	n/a
Beta function at IP $\beta_{x,y}^*$ (m)	0.65	0.7	0.30 – 0.25	0.5	0.15	0.5
Transverse emittance ε_n (μm, rms, normalized)	3	2.2	1.9	2.3	2.5	1.7
IP beam size (μm)	85	115	8	19	7	17
Beam current (mA)	257	220	550	24	1100	33
Bunches per beam	111	111	2556	733	2760	1232
Bunch population (10^{10})	18.5	0.2	10–12.5	0.02	22	0.02
Bunch length (rms, cm)	60	30	8	7–10	9	8
Full crossing angle (μrad)	0	0	320–260	300	500	> 200
Beam-beam parameter or IP, ξ (10^{-3})	7.3	4.1	4.5	1.1	8.6	1.1
Luminosity (10^{30} cm^{-2} s^{-1})	245 (peak) 150 (average)	0.016 (peak) 0.009 (average)	2.1×10^4	0.007	5×10^4 (leveled)	0.006 (leveled)
Maximum integrated NN luminosity per experiment (fb^{-1})	1.3 at 250/255	0.03	169	0.04	250/y	0.43

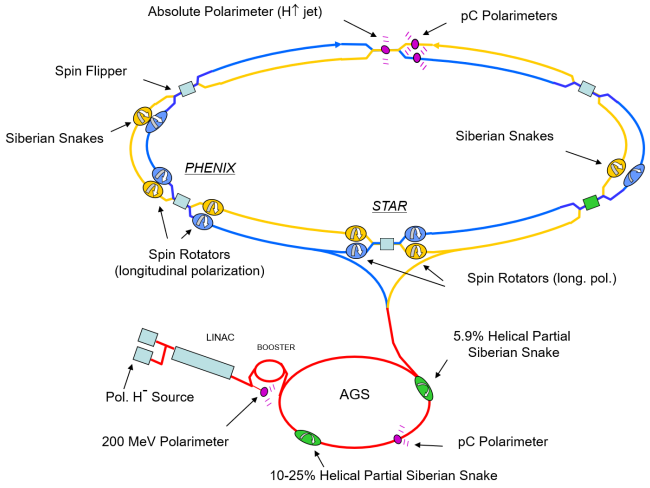

FIG. 13. Layout of the RHIC collider with its injector complex. The two RHIC rings cross at six points. The two principal experiments still running are PHENIX and STAR. The smaller experiments PHOBOS, BRAHMS, and PP2PP have been completed. The LINAC is the injector for polarized protons into the Booster-AGS-RHIC chain. A jet target is used for precision beam polarization measurements. A tandem injector for ions has been replaced by an electron-beam ion source starting with the 2012 run. Adapted from Ranjbar *et al.*, 2004.

on SC Nb-Ti dipole magnets with a field of 3.45 T and housed in the 3.84 km tunnel previously built for the abandoned ISABELLE project. The two RHIC rings cross at six IPs. Two large experiments, STAR and PHENIX, are located at the interaction points referred to as six and eight o'clock, respectively; see Fig. 13. The PHENIX experiment is presently undergoing a major upgrade to become sPHENIX.

The RHIC brings into collision combinations of fully-stripped ions such as H-H $(p$-$p)$, p-Al, p-Au, d-Au, h-Au, Cu-Cu, Cu-Au, Au-Au, and U-U over a wide energy range. The high charge per particle (+79 for gold, for instance) makes IBS of particles within the bunch a special concern, even for moderate bunch intensities.

Three-dimensional stochastic cooling of bunched ion beams was successfully implemented in the RHIC in 2012 (Blaskiewicz, Brennan, and Mernick, 2010) and is now routinely used. With stochastic cooling, steady increases in bunch intensity, and numerous other upgrades, the RHIC now operates with average luminosity in Au-Au collisions of 90×10^{26} cm^{-2} s^{-1}, which is 44 times the design value. Another special feature of accelerating heavy ions in the RHIC is that the beams cross the "transition energy" during acceleration: a point at which $\gamma = \gamma_t \equiv 1/\sqrt{\alpha_c}$ and the derivative of the revolution period with respect to the momentum is zero, leading to zero synchrotron tune and temporary formation of short and potentially unstable bunches according to Eqs. (18)–(20). This is typical for low-energy accelerators, where the necessary phase jump required of the rf system is implemented rapidly and little time is spent near this condition. In the case of RHIC accelerating heavy ions, SC magnets cannot ramp quickly and the period of time spent crossing the transition is relatively long and must be dealt with carefully. For p-p operation the beams are always above their transition energy, so this condition is completely avoided.

The RHIC physics program greatly relies on the machine's ability to accelerate and make collide polarized proton beams (Bunce *et al.*, 2000). Proton beam polarization is produced in a low-energy source (Zelenski, 2010) and must be maintained through numerous depolarizing resonances during the acceleration cycle (Bai *et al.*, 2006). A proton beam energy of 255 GeV with 55% final polarization per beam has been realized (Roser, 2008; Ranjbar *et al.*, 2017). As part of a scheme to compensate for the head-on beam-beam effect, two electron lenses were installed; in 2015, these operated routinely during polarized proton operation at 100 GeV beam energy and doubled both peak and average collider luminosity (Fischer *et al.*, 2015; Gu *et al.*, 2017).

RHIC physics searches for a critical point in the nuclear matter phase diagram (Stephans, 2006) required operation below the nominal injection energy of 10 GeV per nucleon. To reach the integrated luminosity goals, the first bunched beam electron cooler, with electrons from a high-current high-brightness rf accelerator (Kayran *et al.*, 2020), was successfully commissioned for the lowest RHIC energies (Kayran *et al.*, 2019).

2. LHC

The superconducting Large Hadron Collider is the world's highest energy collider (Evans and Bryant, 2008; Bruning, Burkhardt, and Myers, 2012). It supports a broad particle-physics program at the energy frontier (Gianotti *et al.*, 2005).

Over most of the LHC's 26.7 km circumference, the two counterrotating hadron beams are contained in two separate vacuum pipes passing through the same superconducting twin-aperture Nb-Ti accelerator magnets. The LHC beams cross at four IPs, which host two multipurpose high-luminosity experiments, ATLAS and CMS, and two special purpose experiments, ALICE (mainly devoted to heavy-ion physics) and LHCb (B-meson physics). With four crossings, as shown in Fig. 14, each beam passes half of a revolution on the outer side and the other half on the inner so that the circumferences of the two beams are identical. Construction of the LHC technical components and their subsequent installation took more than a decade (1995–2007), and the machine's cost to CERN's budget was 3756 million CHF plus 1224 million CHF of labor cost (Evans, 2009); colliding-beam operation started in 2010. Operation of the LHC machine requires some 120 MW of ac wall-plug power that is about half of 230 MW for the entire CERN, whose annual electric energy consumption is about 1.3 TW h (2015) (CERN, 2017).

Table III shows the LHC luminosity performance in pp and Pb-Pb collisions. In pp collisions the LHC has thus far reached a world record luminosity of 2.1×10^{34} cm^{-2}s^{-1}. For the LHC's ATLAS and CMS experiments, in the first ten years of the LHC operation, the Pb-Pb luminosity well exceeded the design value of 10^{27} cm^{-2} s^{-1}, while for the ALICE experiment the luminosity needed to be "leveled" around this value (Jowett, 2018). The LHC can also provide Pb-p collisions as it did in 2013 and 2016, and other ion-ion or ion-proton collisions at different energies.

In the LHC Run 2 (2015–2018), operation for HEP was conducted with 6.5 TeV protons in each beam. The LHC has set many records for both peak and annual integrated

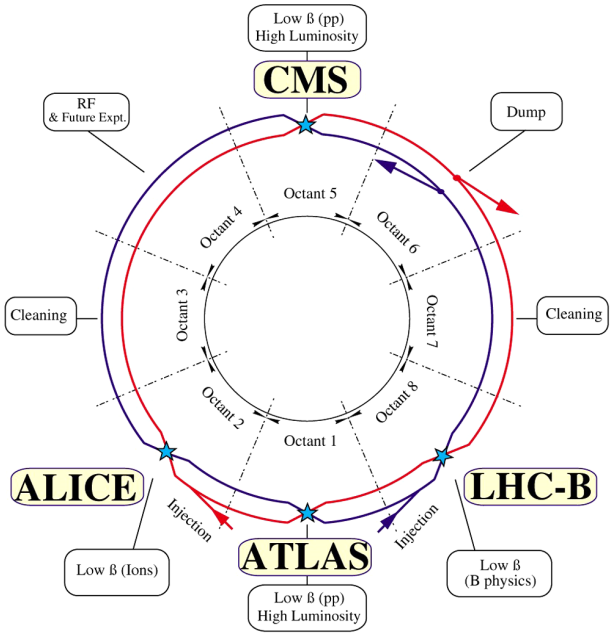

FIG. 14. Layout of the LHC double ring, with its eight long straight sections hosting two general and two special-purpose experimental detectors and/or devoted to specific accelerator functions, such as betatron collimation (cleaning), momentum collimation, beam extraction, rf systems and diagnostics, and injection.

luminosities of hadron colliders (Steerenberg *et al.*, 2019; Wenninger, 2019) (see Fig. 15), largely surpassing the total integrated luminosity of all previous hadron colliders combined. It has been predicted that the final-focusing quadrupoles around the ATLAS and CMS experiments will be destroyed by radiation from collision debris after a total integrated luminosity of around 300 fb^{-1}. More than half of this value has already been delivered. This provides motivation and guides the timing for the High Luminosity LHC (HL-LHC) upgrade (Apollinari *et al.*, 2017), scheduled for around 2025, when the final quadrupole triplets will be exchanged with new ones of larger aperture.

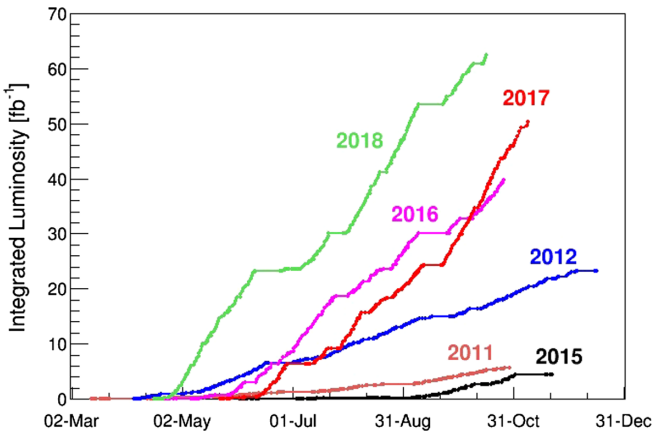

FIG. 15. LHC integrated annual luminosity between 2011 and 2018 for proton operation. From Steerenberg *et al.*, 2019.

Initial luminosity measurements were conducted by sweeping beams transversely across each other (the so-called van der Meer scan) (Balagura, 2011), as was done long ago on the ISR (van der Meer, 1968). Both total and inelastic cross sections for pp collisions were measured with high precision in the first years of LHC operation (Antchev *et al.*, 2019). These are important for beam lifetime and for *event pileup* (the number of interactions per bunch crossing) in the detectors. The LHC beam energy is known to 0.1% and the orbit circumference slowly varies due to Earth's tides by some 1.1 mm (Todesco and Wenninger, 2017).

The extremely high pp luminosities at the LHC of up to 2.1×10^{34} $\text{cm}^{-2}\,\text{s}^{-1}$ (Steerenberg *et al.*, 2019) are achieved by (1) operating high-quality beams from the injector complex, presently comprising a 50 MeV proton linac (to be replaced, in 2020, by a 160 MeV H^- linac), 1.4 GeV PS Booster (to be upgraded to 2 GeV), the 26 GeV Proton Synchrotron (PS), and the 450 GeV SPS, with transverse emittances that are more than 40% lower than the design; (2) smaller $\beta^*_{x,y}$, which decreased from the design value of 55 cm down to 25 cm in 2018, also thanks to the lower emittance allowing one to avoid the aperture limitation in the final-focus quadrupoles, where the maximum beta function grows according to Eq. (15); and (3) by a large number of bunches and a high beam current $I_b \geq 0.5$ A. An outstanding LHC optics control and reproducibility at the level of a few percent (Tomás *et al.*, 2012; Persson *et al.*, 2017b; Maclean *et al.*, 2019) enabled the aforementioned low value of β^* to be achieved with excellent beam-beam performance and guaranteed the safety of the machine.

In the LHC at energies of 5–7 TeV per proton, for the first time synchrotron radiation transforms from a curiosity to a challenge in a hadron accelerator. At design beam current, the system must remove roughly 7 kW due to synchrotron radiation. As photons are emitted, their interactions with the vacuum chamber wall can generate free electrons, with consequent *electron-cloud* development (Dominguez *et al.*, 2013). The heat load due to synchrotron radiation, electron cloud, and also beam image currents is intercepted by a special "beam screen" installed inside the magnets. The beam screen temperature of ~5–20 K is higher than the 1.9 K temperature of the magnet cold bore, which allows for efficient heat removal and for cryopumping through numerous slots in the screen's top and bottom. Overall, the LHC vacuum system comprises 150 m^3 of beam vacuum and 9000 m^3 of cryogenic vacuum; the LHC beam lifetime due to interaction with residual vacuum molecules is larger than 100 h (Cid-Vidal and Cid, 2011).

The LHC beam currents translate into total stored particles' energies of several hundreds of megajoules per beam. Component protection, beam collimation, and controlled energy deposition are consequently of high priority (Valentino *et al.*, 2012). Of particular concern is the possible failure mode of an asynchronous beam dump, where a single extraction kicker module accidentally fires. This would trigger the firing of all other kickers with some delay, but some bunches will be swept across the aperture. These errant bunches would be intercepted on primary collimators, made of robust carbon-fiber-reinforced carbon to withstand such a

catastrophic scenario. The LHC collimation system consists of more than 100 collimators, organized hierarchically. The measured cleaning performance, beam loss rates, and loss distributions have been consistent with expectations, even during the delicate phase of the β^* squeeze (Tygier *et al.*, 2019). Beam particles scattered off the short primary collimators are caught by longer secondary collimators placed at slightly larger apertures, with appropriate phase advances behind the primaries. Tertiary collimators are placed in front of the final quadrupole triplets around the collision points. Special collimators protect against errors at injection sites and, especially, at the entrance of the beam extraction channel. Still other collimators catch large amplitude debris particles coming from the collision point. The system is designed to keep any beam loss in cold magnets to a minimum, and to ensure no magnet quenches even for a proton beam lifetime as low as 12 min.

At the LHC, where the two beams are brought together into a single common beam pipe at each of the four IPs, the large number of bunches and subsequent short bunch spacing (25 ns) would lead to approximately 30 head-on collisions through 120 m of common beam pipe at each IP. A small crossing angle is thus employed, which reduces the luminosity by about 15%, with a similar reduction in the total beam-beam tune shift (Ruggiero and Zimmermann, 2002). Still, in the common beam-pipe section around each IP, the bunches moving in one direction will experience about 30 parasitic long-range encounters with counterrotating bunches. At the LHC, the beams are crossed alternatingly in the horizontal and vertical planes, so that to first order the tune shift induced by the long-range collision cancels between the IPs (Neuffer and Peggs, 1986). For the HL-LHC, it is considered to compensate for residual perturbations of particle motion due to long-range parasitic collisions (Papaphilippou and Zimmermann, 1999), e.g., with the help of current-fed wire compensators (Koutchouk, 2001; Dorda, 2008). In that scheme, 1-m-long thin current-carrying wires are placed parallel to both beams at a normalized distance not much larger than the beam-beam separation at long-range collision points and, therefore, provide a similar but opposite action. Prototype wire compensation tests at the LHC have been successful (Sterbini *et al.*, 2019).

As predicted (Zimmermann, 1997; Baglin *et al.*, 1998; Furman, 1998; Rumolo, Ruggiero, and Zimmermann, 2001), an intensity limit has indeed arisen at the LHC from the buildup of an electron cloud inside the vacuum chamber (Dominguez *et al.*, 2013). This electron cloud may drive different types of beam instabilities and creates additional significant heat loads on the beam screen inside the cold magnets. Indeed, the electron cloud is a primary source of beam instability in the LHC, especially with a proton bunch spacing of 25 ns. Beam performance tends to improve in time thanks to beam-induced surface conditioning ("scrubbing"). In addition, occasional losses of transverse or longitudinal Landau damping arise due to classical machine impedance with contributions from the resistive vacuum chamber, collimators, rf cavities, and chamber transitions. With regard to instability mitigation, the following lessons have been learned in operating the LHC (Métral *et al.*, 2014, 2017; Métral, 2016; Tomas, 2017): (i) there is a narrow range of machine settings for which the beam remains stable all along the cycle, (ii) instabilities occur if transverse betatron coupling exceeds a certain threshold value (different at different stages of operation), (iii) chromaticity settings are crucial along the cycle and cannot be relaxed, (iv) second-order chromaticity can contribute to beam stabilization (Schenk *et al.*, 2018), (v) octupole-magnet settings have to be adapted according to beam emittance, and (vi) the transverse damper is indispensable to preserving beam stability all along the acceleration cycle.

The electron cloud can drive coherent instabilities even when beams are in collision, with associated strong Landau damping. Simulations and earlier measurements at the SPS show that, for lower bunch intensities, the electron cloud in the dipoles tends to form a central stripe. At the LHC, the central density threshold of the electron-cloud-driven single-bunch head-tail instability ($\sim 5 \times 10^{11}$ m^{-3} at a chromaticity of $Q' \approx 15$) is crossed when the bunch intensity decreases; for $Q' > 20$, the threshold becomes much higher. This explanation of beam instabilities observed toward the end of LHC physics fills is also consistent with the disappearance of the phenomenon after scrubbing.

Heavy-ion luminosity at the LHC can be limited by the so-called bound-free pair production (BFPP) during the collision of Pb nuclei:

$$^{208}\mathrm{Pb}^{82+} + {}^{208}\mathrm{Pb}^{82+} \rightarrow {}^{208}\mathrm{Pb}^{82+} + {}^{208}\mathrm{Pb}^{81+} + e^+. \quad (31)$$

This process, with a large cross section of $\sigma \sim 280$ b, generates a secondary beam of $^{208}\mathrm{Pb}^{81+}$ ions, with a fractional rigidity change equivalent to a relative momentum deviation of $\delta = 0.0124$, that can potentially quench superconducting magnets downstream of the IP; see Jowett (2018) and references therein. In 2015, orbit bumps were introduced to displace the BFPP losses safely into a connection cryostat, thereby avoiding magnet quenches (Jowett, 2018).

In the coming years, the ambitious HL-LHC upgrade program (Apollinari *et al.*, 2017) aims at an order-of-magnitude increase in integrated proton-proton luminosity. The heavy-ion physics program of the LHC will also continue during the HL-LHC period, with approximately 10 times higher peak luminosities in Pb-Pb and Pb-p collisions than are available at the present LHC.

The LHC luminosity upgrade calls for doubling the proton beam current and installation of crab cavities that will restore the luminosity loss due to the crossing angle at the IPs. In addition, β^* will be squeezed even further, to as low as 10 cm, with the help of a novel *achromatic telescopic squeeze optics* (Fartoukh, 2013) (which is presently being tested and commissioned in the LHC), along with new larger aperture Nb_3Sn final quadrupoles (Rossi and Tommasini, 2019) and crab cavities. Additional collimators will be installed inside the dispersion suppressors around the main collimation (cleaning) insertion and around some of the experiments. The purpose of adding these collimators is to absorb off-energy particles generated during collisions (especially heavy-ion collisions) or by scattering off one of the existing primary or secondary collimators. The new collimator installation requires the replacement of several 8.3 T Nb-Ti dipoles by stronger and shorter 11 T dipoles made from Nb_3Sn superconducting cable

to provide the necessary space without altering the overall geometry.

According to a recent proposal (Krasny, Petrenko, and Płaczek, 2020), the collision of low-emittance calcium ion beams in the HL-LHC promises partonic luminosities similar to, or higher than, the HL-LHC pp operation, at a lower event pileup (Krasny, Petrenko, and Płaczek, 2020). The low-emittance beam would be produced by fast transverse laser cooling (∼10 s) of partially stripped calcium ions in the SPS, based on the Gamma Factory concept (Krasny, 2015; Krasny *et al.*, 2018); see Sec. IV.C.2).

IV. FUTURE COLLIDERS

Both nuclear physics and particle physics face critical questions that require next-generation colliding-beam facilities. Our understanding of protons and neutrons or nucleons (the building blocks of atomic nuclei) has advanced dramatically, both theoretically and experimentally, over the past half a century. It is known that nucleons are made of fractionally charged valence quarks, as well as dynamically produced quark-antiquark pairs, all bound together by gluons, the carriers of the strong force. A central goal of modern nuclear physics is to understand the structure of the proton and neutron directly from the dynamics of their quarks and gluons governed by the quantum chromodynamics; see National Academies of Sciences, Engineering, and Medicine (2018) and references therein.

For HEP to make significant advances, major new machines of two types will be required. The first type is *Higgs factories* with a c.m.e. of 240–250 GeV for precision studies of the Higgs boson ($m_H = 125$ GeV) and exploration of the Higgs sector in greater detail, including measurements of Higgs couplings to fermions and vector bosons, self-coupling, rare decays, mass, and width. These Higgs factories could also furnish important complementary electroweak precision measurements at other e^+e^- collision energies, such as on the Z pole, above the W-boson pair production threshold, and at energies sufficient for $t\bar{t}$ production. The second type is colliders exploring the energy frontier for potential discoveries through direct searches with c.m.e. levels significantly beyond those of the LHC. The next energy-frontier colliders would aim at producing and discovering new particles or phenomena beyond the standard model, reaching mass scales in the range of tens of TeV and offering a widely extended discovery reach for new gauge bosons Z and W, colorons, diquark scalars, supersymmetry, heavy Higgs, test for compositeness of the standard model particles, etc.

In addition, precision physics at future high-luminosity factories operating at the τ-charm energy also provides sensitivity to new physics at multi-TeV energies and beyond. Ellis *et al.* (2019) presented a comprehensive review of the emerging particle-physics landscape and its potential future.

Next we comprehensively detail colliders that are believed to be feasible (both technically and costwise) for construction over the next several decades. All of these rely mostly on currently available technologies, such as NC or SC rf and/or NC or SC magnets, and in some cases require either no or limited research and development (R&D) to assure energy reach and performance, while other machines anticipate mission-oriented development programs of substantial scope and duration.

A. Ion, *e*-*A*, and *e*-*p* colliders

1. NICA

The Nuclotron-based Ion Collider Facility (NICA) is a new accelerator complex under construction at the Joint Institute for Nuclear Research (JINR), Dubna, Russia (Kekelidze *et al.*, 2012). Its purpose is to study properties of hot and dense baryonic matter, spin physics, properties of the strong interaction vacuum, and QCD symmetries, to explore the nature and properties of strong interactions between quarks and gluons, and to search for signs of the phase transition between hadronic matter and quark-gluon plasma, plus new phases of baryonic matter (Sissakian and Sorin, 2009; Brodsky, 2016; Senger, 2016).

NICA will provide a variety of beam species, ranging from protons and polarized deuterons to massive gold ions. The collider average design luminosity in heavy-ion and light-ion collisions at $\sqrt{s_{NN}} = 4$–11 GeV is $\mathcal{L} = 1 \times 10^{27}$ cm^{-2} s^{-1} for a variety of nuclei up to $^{197}Au^{79+}$ and should be in the range $\mathcal{L} = (1$–$10) \times 10^{31}$ cm^{-2} s^{-1} for polarized proton and deuteron collisions in an energy range of $\sqrt{s} = 12$–27 GeV. The facility employs some existing injectors such as light-ion sources, an Alvarez-type linac LU-20–based source of polarized protons and deuterons, a new electron string ion source that will provide up to 2×10^9 gold ions per 7 μs pulse at a 50 Hz rate, and a linear accelerator consisting of radio-frequency quadrupole (RFQ and drift tube linac sections. The linac accelerates ions with mass-to-charge ratio $A/Z \leq 8$ up to an energy of 6 MeV/u, with efficiencies higher than 80%. A new 600 MeV/nucleon Booster synchrotron ring with a circumference of 211 m will be housed inside the historical JINR Synchrophasotron yoke. Its maximum magnetic rigidity of $B\rho = 25$ Tm is provided by forty 1.8 T SC dipole magnets operating at 4.5 K, which can be ramped at 1.2 T/s (Kostromin *et al.*, 2016). The 60 keV electron cooling system of the Booster, needed for ion accumulation and rapid (3 to 4 s) reduction of the beam emittance at up to 100 MeV/u energies, has been built and commissioned (Bubley *et al.*, 2017; Zinovyev *et al.*, 2018). Ions, protons, and deuterons are then further accelerated, up to the energy of the collider experiments, using the upgraded Nuclotron synchrotron, a 251.52 m circumference superconducting magnet ring that has been operational since 1993 (Issinsky *et al.*, 1994). This ring has a maximum field of 2 T, a ramping rate of 1 T/s for a 4 s cycle, and a maximum magnetic rigidity of 45 Tm. The collider itself will consist of two SC rings of racetrack shape, with maximum magnetic rigidity of 45 Tm and a circumference of 503.04 m. Two IPs are foreseen in opposite straight sections of the NICA collider: one for heavy-ion studies with the multipurpose detector (Golovatyuk *et al.*, 2016) and another for polarized beams, housing the spin physics detector experiment (Savin *et al.*, 2016). The maximum field of the collider dipole *superferric magnets*, which use iron to shape the field and superconductors to excite it, is 1.8 T (Khodzhibagiyan *et al.*, 2019); see Fig. 16. Intrabeam scattering is predicted to result in short emittance growth times of about 3 min at 1 GeV/nucleon and about 40 min at

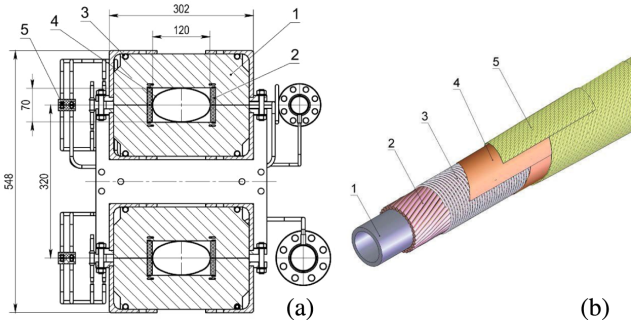

FIG. 16. Superferric 1.8 T magnets of the NICA collider. (a) Cross section of the magnet, based on a cold, window-frame iron yoke and a hollow superconductor winding. 1, lamination; 2, SC cable; 3, yoke cooling tube; 4, beam pipe; 5, current-carrying bus bars. The magnets are placed in a 4.5 K cryostat (not shown). (b) 10.4 kA SC cable. 1–3 mm diameter cooling tube; 2, Nb-Ti SC wire; 3, Ni-Cr wire; 4 and 5, insulation tapes. Adapted from Khodzhibagiyan *et al.*, 2019.

4.5 GeV/nucleon; see Table IV. Effective stochastic and electron cooling systems are required to counteract the emittance growth and to assure operation with a high average luminosity. In the energy range of 1 to 3 GeV/nucleon, a 2.5 MeV, 0.5 A electron cooling system should provide a comparatively short 10 s cooling time and will allow operation of the collider at the space-charge limit of about $\Delta Q_{\mathrm{SC}} \sim -0.05$. In the ion beam energy range of 3 to 4.5 GeV/nucleon, a stochastic cooling system will ensure characteristic cooling times of about 500 s (Kostromin *et al.*, 2012).

The projected NICA project cost is about $500 million. NICA construction started in 2013. The first beam run of its injectors is scheduled for 2020 and the first colliding beams are expected in 2022 (Kekelidze *et al.*, 2016; Syresin *et al.*, 2019).

2. Low-energy electron-ion collider proposals: ELISe at FAIR, EicC at HIAF

The electron-ion collider (EIC) experiment ELISe (Antonov *et al.*, 2011) is part of the experimental program envisaged at the international Facility for Antiproton and Ion Research (FAIR) (Gutbrod *et al.*, 2006) in Darmstadt, Germany. It will offer the unique opportunity to scatter electrons with an energy of up to 0.5 GeV off short-lived exotic nuclei with energies of up to 0.74 GeV/nucleon (Simon, 2007; Suda and Simon, 2017) in order to investigate the structure of radioactive isotopes. Figure 17 presents the schematic layout of the New Experimental Storage Ring [(NESR), circumference 222.9 m] (Dimopoulou *et al.*, 2007) for rare isotope beams and the Electron Antiproton Ring [(EAR), circumference 53.7 m, selected such that the revolution frequency of the EAR is 5 times that of one of the ions]. Electrons with energies ranging from 125 to 500 MeV will be provided by an electron linac and stored in the EAR. Antiprotons of similar momentum can be directed from a dedicated collector ring (not shown in Fig. 17) into the EAR via a separate beam line. The electron ring is placed outside the NESR so that a bypass beam line connects them and provides sufficient space for an electron spectrometer and a recoil detector system. The ion and electron or antiproton beam trajectories intersect at an IP surrounded by the electron spectrometer; auxiliary detectors for measuring reaction products are also included in the ELISe plan.

Experiments require high resolution of transferred energy and momentum in electron-ion scattering. A momentum spread of the electron beam (8 bunches, $5 \times 10^{10} e^-$ each) of about 0.036% can be achieved; its value depends mainly on IBS and statistical fluctuations due to synchrotron radiation. IBS also causes the beam size to grow and limits both luminosity and lifetime. Collision focusing optics with $\beta^*_{x,y} = 15/100$ cm allows for luminosity values ranging from $\mathcal{L} = 10^{28}$ to 10^{30} cm^{-2} s^{-1} for a wide variety of isotopes from He to U. The number of ions in each of four NESR bunches varies between 7×10^7 and 8×10^9, depending on the optimization of production and preparation of secondary beams, maximum yield, and the acceptance of the Super Fragment Separator. At high intensities, the ion population is expected to be limited by space-charge effects at a tune shift parameter of $\Delta Q_{\mathrm{SC}} \sim -0.08$; see Table IV.

Construction work on the FAIR project began in the summer of 2017. The final scope of the project, consisting

TABLE IV. Key design parameters of future ion-ion, electron-ion, and electron-proton colliders.

Parameter or collider species	NICA $ii(pp)$	ELISe i	ELISe e	EicC-I p	EicC-I e	JLEIC p	JLEIC e	eRHIC p	eRHIC e	LHeC p	LHeC e
c.m. energy $\sqrt{s}$ (GeV)	9	1.8		16.7		44.7		105		1174	
Beam energy (GeV)	4.5/n	0.74/n	0.5	20	3.5	100	5	275	10	7000	49.2
Circumference (m)	503	224	53.7	600	800	2336		3834		26700	5332
Number of bunches	24	40	8	2000		3228		1320		2808	⋯
Particles per bunch (10^{10})	0.22	8.6×10^{-4}	5	0.5	3.2	1	4.7	6	15.1	22	0.31
Emittance (H/V,rms normalized, μm)	1.1/0.8	0.07	45	1	68	0.7/0.13	83/17	9.2/1.6	20/1.3	2.5	50
Beta functions at IP $\beta^*_{x,y}$ (cm)	35	100/15	100/15	2/1	20/10	8/1.3	5.7/1	91/4	41/5	7	6.5
Bunch length (rms, cm)	60	15	4	3	10	2.5	1	6	1.9	7.6	0.006
Beam-beam parameter $\xi_{x,y}$ (10^{-3})	50	⋯	⋯	3	10	15	40	14/7	70/100	0.15	1
Space-charge param. $\lvert\Delta Q_{\mathrm{SC}}\rvert$	0.05	0.08	⋯	0.01	⋯	0.018	⋯	⋯	⋯	⋯	⋯
IBS time (horizontal or longitudinal, min)	42	⋯		8.3/3.3	⋯	0.7/2.3	⋯	126/120	⋯	∼4000	⋯
Polarization	80%	⋯		⋯		85%	80%	80%	80%	0%	80%
Facility ac power (MW)	26	10 (+82 FAIR)		150 (+80 HIAF)		n/a	n/a	28	44	100[a]	100
Luminosity (10^{30} cm^{-2} s^{-1})	0.001	0.01		10^3		1.5×10^4		1.05×10^4		0.9×10^4	

[a]Without LHC injectors.

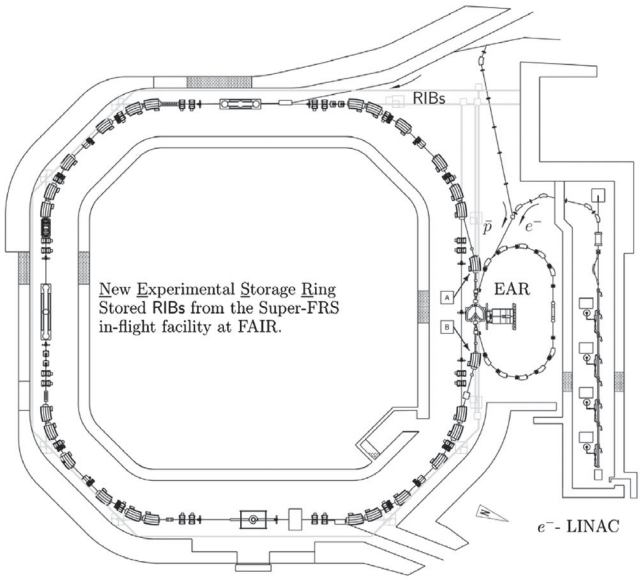

FIG. 17. Conceptual layout of the planned electron-ion or antiproton-ion collider hosting the ELISe experiment. The intersection region $A-B$ is situated in a bypass section to the New Experimental Storage Ring (NESR) and hosts a dedicated spectrometer. From Antonov *et al.*, 2011.

of many rings, and the construction schedule will depend on cost. In 2005, this was estimated to be 1262 million euros but was recently reconsidered; additional funding needed amounts to 850 million euros, not including contingencies (FAIR Project).

Conceptually similar is a proposal (X. Chen, 2018) from the Institute of Modern Physics (Lanzhou, China) to build a high-luminosity polarized electron-ion collider in China (EicC) with $\mathcal{L}=4\times10^{33}$ cm^{-2} s^{-1} at $\sqrt{s}=12$–24 GeV, based on the capabilities offered by the Heavy Ion High Intensity Accelerator Facility (HIAF) (Yang *et al.*, 2013). The Huizhou HIAF project was approved in 2015, with construction commencing in 2018; facility commissioning is expected in 2025. The 2.5 billion Chinese yuan complex will operate a 180-m-long superconducting 17 MeV/nucleon linac and a 569 m 34 Tm booster ring capable of accumulating, cooling, and accelerating ions to 4.25 GeV/nucleon or protons to 9.3 GeV. The first stage of the complex extension to the electron-ion collider calls for an additional high-current (3 to 4 A) 3.5–5 GeV electron ring to collide with up to 20 GeV HIAF protons and ions, an srf four- to five-pass recirculating linac injector, a polarized ion source, and *Siberian snakes* for the existing HIAF accelerators; see Table IV. The final stage of the EicC, called EicC-II, assumes the new construction of 1.5–2 km long, figure-8 shaped 60–100 GeV proton and 5–10 GeV electron rings in the same tunnel (J. Chen, 2018). Construction cost, as well as details of the design and schedule of the Chinese electron-ion collider, will require further study.

3. High-energy EIC proposals: JLEIC at TJNAF and eRHIC at BNL

Higher-energy electron-ion colliders can answer scientific questions that are central to completing our understanding of nuclear matter and are integral to the agenda of nuclear physics today. For example, the 2018 National Academies of Science assessment of U.S.-based EIC science (National Academies of Sciences, Engineering, and Medicine, 2018) emphasized the priority of constructing a new facility that will be flexible over a multidecade operating lifetime, and that can support exploration of nuclear physics over a wide range of center-of-mass energies and ion species with highly polarized electrons and light ions. According to the white paper (Accardi *et al.*, 2016), the requirements of an EIC include highly polarized ($P_{e,n}\sim70\%$) electron and nucleon beams (as the precision of measurements of interest scales as $\mathcal{L}P_e^2P_n^2$), a spectrum of ion beams from deuterons to the heaviest nuclei (U or Pb), variable c.m.e. values from $\sqrt{s}=20$ to 100 GeV, upgradable to ~140 GeV, high luminosities of $10^{33\text{–}34}$ cm^{-2} s^{-1}, and possibilities of having more than one interaction region. Significant accelerator R&D is needed to attain the required energy, luminosity, and polarization, including development of srf crab cavities and advanced SC magnets for collider rings and interaction region focusing, strong electron cooling of hadron beams, essential to attain luminosities 2 orders of magnitude beyond the predecessor HERA ep collider, and polarized particle sources beyond the state of the art, augmented by the development of special magnets and operational techniques to preserve the polarization through the acceleration process to the collisions.

Two multilaboratory collaborations evolved in the United States, each of which proposes site-specific conceptual EIC designs based on infrastructure already available: the Jefferson Laboratory Electron Ion Collider (JLEIC) led by the Thomas Jefferson National Accelerator Facility, and eRHIC led by Brookhaven National Laboratory.

The JLEIC was designed to take advantage of the existing 12 GeV electron srf recirculating linac CEBAF at Jefferson Lab, which would be used to provide an electron beam for the collider. Both colliding beams would be stored in two figure-8 shaped collider rings. One ring, made of NC magnets, stores electrons at 3 to 12 GeV, with an average beam current of up to 3 A (below 7 GeV). The second ring, consisting of 6 T SC magnets, stores either fully stripped ions, with up to 80 GeV per nucleon, or protons with energies ranging from 30 to 200 GeV. The two collider rings and the additional 13 GeV/c high-energy ion or proton booster ring are stacked vertically, have nearly identical circumferences of 2.3 km, and are housed in the same underground tunnel next to the CEBAF facility, as illustrated in Fig. 18. The unique figure-8 shape of the collider allows complete cancellation of spin precession between the left and right arcs, in which guiding vertical magnetic fields are in opposite directions, thus resulting in zero net spin tune independent of energy. This shape is chosen for optimization and preservation of ion spin polarization during acceleration in the booster and collider rings, as well as during beam storage. The crossing angle of the tunnels is 77.4° and electron and ion beam lines intersect at an angle of $\theta_c=50$ mrad in two long straights next to the crossing point, allowing for accommodation of two detectors. The CEBAF 1.5 GHz linac will serve as a full-energy injector into the 3–12 GeV electron ring, requiring no upgrade for energy, beam current, or polarization. An entirely new hadron-beam

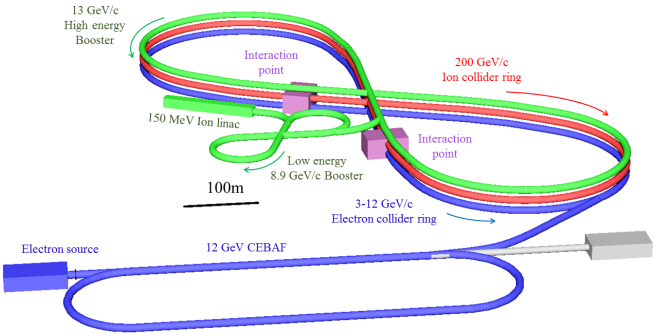

FIG. 18. Layout of the Jefferson Lab Electron-Ion Collider (JLEIC). Adapted from Zhang, 2019.

complex is required for proton and ion beam generation and acceleration. This complex includes sources for polarized light ions and for nonpolarized light to heavy ions; a 150 MeV srf linac for protons, a compact figure-8 8.9 GeV/c low-energy booster ring, and the 13 GeV/c high-energy booster ring, which injects into the main 200 GeV/c proton (or 80 GeV/nucleon ion) ring. Key design parameters of the JLEIC are presented in Table IV. The JLEIC upgrade to 140 GeV c.m.e. will require an increase of the proton energy to 400 GeV through the installation of new 12 T SC magnets.

The JLEIC luminosity performance is determined by different limits depending on the c.m.e. (Fig. 19). At 20–35 GeV energies it is limited by space-charge effects for the hadron beams, in the range of 35–60 GeV, by beam-beam effects on both beams at higher energies by synchrotron radiation of the high-energy electron beam (Zhang, 2019). Synchrotron radiation results in emittance growth and also limits the maximum electron current. The electron current, which is 3 A at energies below 7 GeV, decreases to less than 0.5 A at 12 GeV, if the total radiation power is limited to

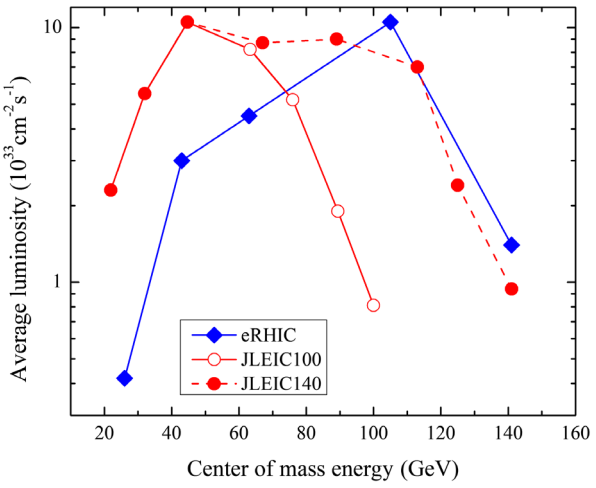

FIG. 19. Average e-p luminosity of JLEIC and eRHIC as a function of c.m.e. The JLEIC average luminosity takes into account a 75% operational duty factor and is given for both baseline design (open circles) and a potential future upgrade with a 400 GeV proton ring (solid circles). The eRHIC luminosity is averaged over the data-taking cycle and equals 95% of the peak luminosity.

10 MW. Hadron-beam cooling is needed to combat IBS and to reduce or preserve beam emittances. It, therefore, is critical for the JLEIC e-p and e-i luminosities. A three-stage electron cooling has been proposed that includes a conventional 50 kV dc cooler in the low-energy booster ring (for ions), a state-of-the-art 1.1–4.3 MeV dc cooler in the high-energy booster ring, and a 43–109 MeV ERL-based cooler in the collider ring (the electron energy range indicates values for lead ions and protons). The required cooling rates call for electron bunches with 3.2 nC charge supplied at the 476.3 MHz repetition rate of the ion bunches, resulting in a 1.5 A beam current, far higher than what has ever been demonstrated in an ERL. To reduce the average electron cooling current, a circulating cooler ring concept has been proposed that circulates the high charge bunches 11 times through the cooler before returning them to the ERL (Benson *et al.*, 2018). This novel concept needs further development and testing of its key parts, such as the fast transverse kicker needed to kick electrons in and out of a 60 m circulator ring, and the magnetized electron-beam generation and transport to assure a low temperature of the electrons and, therefore, a high cooling efficiency.

A beam crossing angle of 50 mrad is necessary to avoid parasitic collisions due to short bunch spacing, make space for machine elements, improve detection, and reduce detector background. To prevent a factor of ∼12 luminosity loss caused by the crossing angle, srf crab cavities will need to be installed on both sides of each IP, and for both beams, to restore head-on collisions in the center-of-mass frame.

The eRHIC design (Willeke *et al.*, 2019) aims at polarized electron-proton collisions in the c.m.e. range 29–141 GeV that are accomplished by colliding 41 to 275 GeV protons delivered by the existing "yellow ring" of the RHIC heavy-ion collider and the entire existing hadron-beam injector chain, with 5–18 GeV electrons from a new electron storage ring installed in the RHIC tunnel. The eRHIC peak luminosity reaches about 10^{34} cm^{-2} s^{-1} at $\sqrt{s} = 100$ GeV; see Fig. 19. Key parameters of the eRHIC are given in Table IV. Polarized electrons are provided by a full-energy spin-transparent rapid-cycling synchrotron (RCS) (Ranjbar *et al.*, 2018) using normal-conducting rf cavities, located in the 3.8 km RHIC tunnel. The RCS is specifically designed to be free of intrinsic resonances over the entire acceleration range from 400 MeV at injection to 18 GeV. Spin transparency is achieved by a high superperiodicity of the RCS focusing lattice of $P = 96$, and an integer tune of $[Q_y] = 50$. With such parameters, intrinsic spin resonances, which occur under the condition (Lee, 1997)

$$G\gamma = nP \pm [Q_y] \tag{32}$$

(here n is an integer, $G = 0.001\,159\,65$ is the anomalous gyromagnetic ratio of the electron, and γ is the relativistic Lorentz factor), are avoided over the entire energy range of the RCS and the simulated polarization transmission efficiency is about 97%, even in the presence of magnet misalignments as large as 0.5 mm rms.

Focusing for the electron storage ring is achieved through 16 FODO cells in each of the six arcs. To obtain the required design emittance over the entire energy range from 5 to 18 GeV, the ring operates with different betatron phase

advances per FODO cell: 90° at 18 GeV, and 60° at 10 GeV and below. The bending sections in these cells are realized as *superbends*, with each section consisting of three individual dipoles, namely, two 2.66-m-long dipoles with a short (0.44-m-long) dipole in between. At beam energies of 10 GeV and above, all three segments are powered uniformly for a smooth, uniform bend, while at 5 GeV the polarity of the short center dipole is reversed, resulting in additional synchrotron radiation in this configuration to provide the required fast radiation damping enabling the high electron beam-beam parameter ξ_y of 0.1. The total electron-beam intensity is set by a 10 MW power limit on the ring srf system, which must restore the synchrotron-radiation losses. Arbitrary spin patterns in the electron storage ring (with simultaneous storage of bunches with spin "up" and bunches with spin "down" in the arcs) are achieved by injecting polarized electron bunches with the desired spin orientation at full storage energy. Since the Sokolov-Ternov effect (Sokolov and Ternov, 1964) leads to depolarization of bunches with spins parallel to the main dipole field, a frequent replacement of individual bunches is required, at a rate of about one bunch per second, to keep the time-averaged polarization sufficiently high.

The beams of electrons and ions or protons collide in one or two interaction regions at a 25 mrad crossing angle. Different frequency choice for the eRHIC crab cavity systems have been considered. For example, a combination of 200 and 400 MHz for the long proton bunches and 400, 800, 1200, and 1600 MHz for the shorter electron bunches would enable avoiding the luminosity reduction due to the crossing and minimize hadron-beam emittance growth to less than 5%/h. An alternative, technically simpler option would be to use 200 MHz crab rf systems for both protons and electrons (Verdu-Andres and Wu, 2019). A dedicated fill pattern ensures that each bunch collides only once per turn. This way, luminosity can be shared equally between two detectors without exceeding the beam-beam limit. To maximize luminosity, the beams are focused to flat cross sections $\sigma_x^* \gg \sigma_y^*$ at the IP. Sophisticated interacting region optics (see Fig. 20) provides sufficient separation of the hadron beam from the 5 mrad forward neutron cone, separates the electron beam from the Bethe-Heitler photons used for luminosity measurements, and allows for a safe passage of the synchrotron-radiation fan generated upstream of the IP through the detector.

The hadron-beam parameters are similar to what has been achieved in the RHIC, with the exception that the number of bunches will be increased from 110 in the present RHIC up to 1320 or 1160 in the eRHIC, while the total hadron-beam current will be increased by a factor of 3. The higher current could cause unacceptable heating of the cryogenic stainless-steel beam pipes. A thin layer of copper will, therefore, be added to improve the beam-pipe surface conductivity. A much thinner layer of amorphous carbon will next be deposited on top of the copper coating to reduce secondary electron yield and, therefore, suppress the formation of electron clouds. A broad spectrum of desired center-of-mass collision energies implies operation over a wide range of ion energies and, therefore, substantially different ion velocities. To maintain the synchronization between electron and hadron beams, the

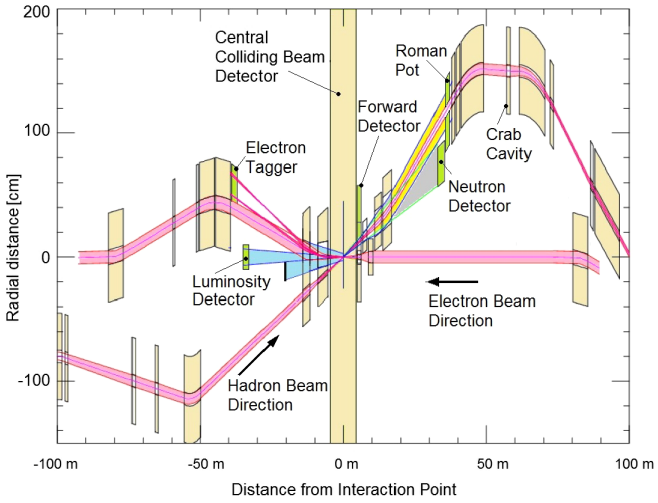

FIG. 20. Layout of the eRHIC interaction region. The length scales for the horizontal and vertical axes are significantly different. Beams cross with a crossing angle of 25 mrad. The IR design integrates focusing magnets for both beams, luminosity and neutron detectors, electron taggers, spectrometer magnets, near-beam detectors (Roman pots for hadrons), crab cavities, and spin rotators for both beams. From Willeke *et al.*, 2019.

circumference of one of the two rings has to be adjusted. This is accomplished by two methods: between 100 and 275 GeV proton energy, a ± 14 mm radial orbit shift is sufficient to account for variations in velocity of the hadron beam. For proton beam operation at 41 GeV, the beam will travel through the inner "blue" arc of the RHIC between interaction regions IR12 and IR2 instead of the outer "yellow" arc, thus reducing the circumference by 93 cm.

Usable store length in the eRHIC collider is limited by an IBS growth time of approximately 2 hours. Since the turn-around time between stores is of the order of 30 min, average luminosity would only be about half the peak value. To counteract the fast emittance growth due to IBS and, hence, to increase usable store length, strong hadron cooling with some 1 h cooling time is required. Two cooling schemes are currently under consideration: a somewhat conventional cooling with a bunched electron beam and variations of *coherent electron cooling*, where an electron beam is used as a pickup and kicker in a high bandwidth stochastic cooling scheme (Litvinenko and Derbenev, 2009). The feasibility of the former, based on the electron rf photoinjector system, has recently been demonstrated (Kayran *et al.*, 2019, 2020), but the required high beam intensities for a bunched beam electron cooler for eRHIC far exceed the capabilities of present-day electron guns. An alternative scheme in which the electron beam is stored in a small storage ring equipped with strong damping wigglers is being evaluated. Coherent electron cooling has not yet been demonstrated experimentally. An alternative could, therefore, be to use the existing "blue" ring as a full-energy injector to cool proton or ion bunches at or slightly above 25 GeV injection energy, which is much easier due to the strong energy dependence of cooling forces, and then to ramp the blue ring and replace the entire fill in the "yellow" storage ring every 15 min. Yet another possible design scenario, without any hadron cooling, results

in optimized machine parameters yielding a peak luminosity of 0.44×10^{34} cm^{-2} s^{-1}. In general, hadron cooling is one of the most important topics in the ongoing eRHIC R&D program, together with the development of the required crab cavities, efficient srf for the electron storage ring, and fast kickers to manipulate the significantly increased number of bunches.

Early in 2020, the U.S. DOE announced that the Electron-Ion Collider will be built at Brookhaven National Laboratory in Upton, New York (Cho, 2020).

4. LHeC, HE-LHeC, and FCC-*eh*

Deep-inelastic scattering of electrons on protons or nuclei has traditionally proven to be the best means to probe the inner structure of nucleons and nuclei. A unique opportunity for this can be offered by colliding 7 TeV protons circulating in the LHC with 60 GeV electrons from an ERL (Kuze, 2018). Since such a Large Hadron Electron Collider (LHeC) (Abelleira Fernandez *et al.*, 2012) uses a beam of the already built hadron collider, it can be realized at an affordable cost and can run concurrently with hadron-hadron collision experiments. The LHeC can provide a much cleaner collision environment at $\sqrt{s} = 1.3$ TeV and would be another powerful tool for studying Higgs boson properties (Mellado, 2013; Zimmermann, Bruning, and Klein, 2013).

The electron ERL has a racetrack shape accommodating two 10 GeV SC linacs in the straights, connected by arcs with a bending radius of about 1 km. The LHeC linacs employ SC bulk Nb cavities with a frequency of 800 or 400 MHz. Three acceleration passages are required to attain the design electron energy of 60 GeV at the IP, followed by three turns of deceleration for energy recovery (the basic ERL principle is sketched in Fig. 39). The total circumference of the baseline LHeC is exactly one-third of the LHC, easing the introduction of electron bunch gaps for ion clearing without perturbing the proton beam. Smaller circumferences (one-fourth, one-fifth) are also possible at the cost of lower electron-beam energy.

The IP beam size of the LHeC is determined by the emittance and minimum β^* of the proton beam; see Table IV. Luminosity is then set by the electron-beam current. A luminosity of the order of 10^{34} cm^{-2} s^{-1} is required for Higgs boson physics studies (Zimmermann, Bruning, and Klein, 2013), demanding a high average electron-beam current of 20–50 mA at the collision point that in turn can be achieved only with energy recovery. The three-pass beam recirculation including energy recovery implies a 6 times higher current in the SC linacs, which simultaneously accelerate three beams of different energies and decelerate three other beams. Construction of a high-current multiturn 500 MeV ERL test facility for the LHeC, called PERLE, is planned at LAL in Orsay, France (Angal-Kalinin *et al.*, 2018). PERLE will demonstrate the technical feasibility of the LHeC concept. At the end of 2019, an already constructed multipass ERL test facility of a different type, Cornell-BNL ERL Test Accelerator (CBETA) at Cornell University, has achieved four turns of acceleration followed by four turns of deceleration (Brookhaven National Laboratory, 2020), albeit at a much lower beam current than required for the LHeC; see also Sec. V.B. The cost and ac wall-plug power estimates for a 9 km, 60 GeV LHeC are 1.8 billion CHF and 100 MW for the e^- branch, respectively (Bruning, 2018). A smaller 5.3 km, 50 GeV version of the LHeC has recently become the new baseline (Agostini *et al.*, 2020). A 30 GeV electron ERL version of the LHeC will cost close to 1.1 billion CHF and has been considered a possible first stage, under the assumption that the electron-beam energy can later be increased to 50 GeV, for another 0.3 billion CHF.

The same or a similar ERL could also be used to realize electron-hadron collisions at the High-Energy LHC [(HE-LHeC), which has twice the LHC's proton energy] or at the FCC-*hh* [(FCC-*eh*), which has 7 to 8 times more energetic protons]; see Sec. IV.C. The luminosities for HE-LHeC and FCC-*eh* are above 10^{34} cm^{-2} s^{-1} at $\sqrt{s} = 1.8$ and 3.5 TeV, respectively (Bruning *et al.*, 2017).

B. Lepton colliders studying Higgs boson, electroweak sector, QCD, and neutrino physics

Higgs factory proposals generally aim at improving the measurement precision for properties of the Higgs boson, top quark, W, and Z by an order of magnitude or more compared with previous studies.

The International Linear Collider (ILC), with a center-of-mass energy of 250 GeV in e^+e^- collisions, has been under consideration for more than two decades and could potentially be upgraded to $\sqrt{s} = 500$ GeV or even 1 TeV. CERN's CLIC design, in development since the mid 1980s, also includes possible upgrades, from an initial 380 GeV c.m.e. to ultimately 3 TeV, which would enable searches for new particles of significantly higher masses.

Two proposals for circular e^+e^- colliders have appeared more recently: the Future Circular Collider (FCC-*ee*) at CERN (Benedikt *et al.*, 2019a) and the Circular Electron-Positron Collider (CEPC) in China (CEPC Study Group, 2018). These ambitious, large-scale projects based on well-established technologies are not extendable to TeV or multi-TeV energies, but they offer several important advantages that include the potential for much higher luminosities and, thus, higher precision, the ability to operate multiple experiments simultaneously, and the fact that their 100 km circular tunnels could later house $O(100\ \text{TeV})$ hadron colliders.

At lower energies, the main aim of the proposed Super Tau-Charm Factories is the production and precise study of charmonium states and of the tau lepton.

1. Super τ-charm factories

Two super tau-charm factories are being proposed, in Russia (SCT) (Piminov, 2018) and China (HIEPA) (Luo *et al.*, 2019). They will provide excellent possibilities in the search for new physics and for detailed studies of known phenomena. Both proposals consider double-ring e^+e^- colliders operating at a c.m.e. between about 2 and 7 GeV. Their design luminosity is 2 or 1 times 10^{35} cm^{-2} s^{-1}, achieved with $\beta_y^* = 0.5$ (0.6) mm and a crab-waist collision scheme. The expected beam lifetime is about 10 min, supported by top-up injection, requiring a positron production rate of up to 10^{11}/s. The electron beam can be longitudinally polarized at the collision point. Preliminary conceptual designs are available for both

projects. Numerous synergies and complementarity exist between the two super τ-charm factory projects, the already constructed SuperKEKB and the proposed future higher-energy circular e^+e^- Higgs factories FCC-ee and CEPC; see Sec. IV.B.3.

2. Linear e^+e^- colliders for Higgs sector: ILC and CLIC

As previously noted, linear colliders are almost free of synchrotron-radiation losses, and their energy scales with the gradient and length of their accelerating sections; see Eq. (4). Beam acceleration by a sequential array of rf cavities is by itself a straightforward technique for reaching the c.m.e. required for Higgs boson studies in e^+e^- collisions. The main challenge in designing a high-energy, high-luminosity single pass collider is the power requirement. Indeed, luminosity of a linear collider is constrained by three limiting factors (in parentheses)

$$\mathcal{L} = (N_e n_b f_{\mathrm{r}}) \left(\frac{1}{\sigma_y^*}\right) \left(\frac{N_e}{\sigma_x^*}\right) \frac{H_D}{4\pi}, \tag{33}$$

where the first factor is proportional to the total beam current, set by particle sources (especially challenging is the positron production; discussed later), by coherent beam instability concerns, and most importantly by the available rf power. If the total ac wall-plug power of the collider is P_{wall} and the efficiency of converting it into beam power is $\eta \equiv P_b/P_{\mathrm{wall}}$, then $N_e n_b f_{\mathrm{r}} = \eta P_{\mathrm{wall}}/eE_{\mathrm{c.m.e.}}$. The efficiency of the rf system, the largest and most critical part of total efficiency η, is usually less than 10% (Delahaye, 2016), and it constitutes the biggest technological challenge for linear colliders. For superconducting linear colliders like the ILC, the efficiency of the cryoplants becomes another important contribution to the overall electrical power budget. The cryoplant efficiency is characterized by the coefficient of performance (COP), defined as the amount of heat removed at the cryogenic temperature divided by the electrical input power required to remove this heat. The ILC technical design report (TDR) (Adolphsen *et al.*, 2013) assumes a COP of 700 W/W at 2 K (for comparison, the present LHC cryogenic system achieves 900 W/W), which translates into a total cryogenics power of about 14 MW for the 250 GeV ILC baseline (List, 2019).

The second factor in the luminosity equation calls for ultrasmall vertical beam size at the IP σ_y^*, which in turn requires record small beam emittances formed in dedicated damping rings (Emma and Raubenhemier, 2001), precise $O(10\ \mu\mathrm{m})$ mechanical and beam-based alignment, stabilization of focusing magnets and accelerating cavities at the nanometer level (Baklakov *et al.*, 1993; Sery and Napoly, 1996; Baklakov *et al.*, 1998; Shiltsev, 2010a), and beam position monitors (BPMs) with 0.1 μm resolution, in order to obtain the rms beam sizes of 8 nm (vertical) and 520 nm (horizontal) at the ILC IP and of 3 nm/150 nm at the CLIC IP (Raubenheimer, 2000; Kubo, 2011; Pfingstner, Adli, and Schulte, 2017).

The third factor in Eq. (33) (N_e/σ_x) defines the beam energy spread and the degradation of the luminosity spectrum arising from the beamstrahlung radiation of photons in the strong electromagnetic (EM) fields of the tightly compressed opposite bunch (Chen, 1992; Bell and Bell, 1995). This effect grows with collision energy. For example, it amounts to $\delta E/E \sim 1.5\%$ in the 250 GeV c.m.e. ILC, while in the 380 GeV CLIC already some 40% of the collider luminosity is more than 1% away from the maximum c.m.e. The management of P_{wall} leads to an upward push on the bunch population N_e and, therefore, on the number of beamstrahlung photons emitted per $e^{\pm}$, which is given by $N_\gamma \approx 2\alpha r_e N_e/\sigma_x^*$, where α denotes the fine-structure constant (Zimmermann, 2001b). Typically, one aims for $N_\gamma \lesssim 1$ to retain a significant luminosity fraction close to the nominal energy. A consequence is the use of flat beams, where N_γ is controlled by the beam width σ_x^* and the luminosity is adjusted through the beam height σ_y^*, resulting in the extremely small vertical small sizes at both ILC and CLIC. The final factor in Eq. (33) H_D represents the enhancement of luminosity due to the *pinch effect*, i.e., the additional focusing occurring during the collision of oppositely charged bunches; H_D typically assumes values between 1 and 2.

The ILC TDR (Adolphsen *et al.*, 2013) foresaw a baseline c.m.e. of 500 GeV, with a first stage at 250 GeV and upgrade provision for 1 TeV, at luminosity values comparable to the LHC's. Recent revisions, motivated by the low mass of the Higgs boson, have established new optimized configurations for collisions at 250 GeV (Evans and Michizono, 2017; Aihara *et al.*, 2019). The ILC employs 1.3 GHz srf cavities made of bulk Nb, operating at an accelerating gradient of 31.5 MV/m at 2 K, and its initial stage requires some 110 MW of site power for the accelerator facility; see the key machine parameters in Table V. The 1.3 GHz pulsed srf technology of the ILC was developed for the TESLA project (Aune *et al.*, 2000) and successfully applied for the European X-Ray Free-Electron Laser (Altarelli *et al.*, 2006). Progress toward higher field gradients and Q values of SC cavities continues to be made, with nitrogen doping, nitrogen-diffusion techniques, and Nb_3Sn cavities as recent examples (Grassellino *et al.*, 2013; Dhakal *et al.*, 2015; Padamsee, 2019).

Figure 21 presents a schematic overview of the ILC with its main subsystems. The accelerator extends over 20.5 km, dominated by the main electron and positron linacs and another ~5 km of beam delivery and final-focus system. It consists of two main arms intersecting at a 14 mrad crossing angle. Electrons with 90% polarization are produced by an electron gun, where a Ti:sapphire laser pulse hits a photocathode with a strained GaAs/GaAsP superlattice structure. The baseline solution for ILC positron production employs a 320-m-long SC helical undulator with 5.85 mm diameter beam aperture, located at the end of the 125 GeV electron main linac (Moortgat-Pick *et al.*, 2008; Alharbi *et al.*, 2019). When the main electron beam passes through this undulator it produces polarized photons that are converted to positrons, in a rapidly rotating target (2000 rounds per minute), resulting in 30% longitudinal positron polarization. An alternative design that does not require a fully operational main linac instead utilizes a separate, dedicated 3 GeV electron accelerator to produce positrons via conventional e^+e^- pair production, when the electron beam hits a target (no positron polarization is provided in that case). After acceleration to 5 GeV, electrons and positrons are injected into the centrally placed

TABLE V. Tentative parameters of selected future e^+e^- high-energy colliders.

Species	FCC-*ee* (Benedikt *et al.*, 2019a) e^+e^-			CEPC (CEPC Study Group, 2018) e^+e^-		ILC (Aihara *et al.*, 2019) e^+e^-		CLIC (Aicheler *et al.*, 2019) e^+e^-	
Beam energy (GeV)	45.6	120	183	45.5	120	125	250	190	1500
Circumference, length (km)		97.75		100		20.5	31	11	50
Interaction regions		2 or 4		2		1		1	
Integrated luminosity/expt. (ab^{-1}/yr)	26	0.9	0.17	4	0.4	0.2	0.3	0.2	0.6
Peak luminosity (10^{34} cm^{-2} s^{-1})	230	8.5	1.55	32	3	1.4	1.8	1.5	5.9
Repetition rate (Hz, f_{rev} for rings)		3067		3000		5		50	
Polarization (%)	≥ 10	0	0	5–10	0	80, 30% (e^-, e^+)		80%, 0%	
Time between collisions (μs)	0.015	0.75	8.5	0.025	0.68	0.55	0.55	0.0005	0.0005
Energy spread (rms, 10^{-3})	1.3	1.65	2.0	0.8	1.3	1.9, 1.5 (e^-,e^+)	1.2, 0.7 (e^-,e^+)	3.5	3.5
Bunch length (rms, mm)	12.1	5.3	2.5	8.5	4.4	0.3	0.3	0.07	0.044
Normalized rms emittance (H,V μm)	24, 0.09	148, 0.3	520, 1.0	16, 0.14	284, 0.6	5, 0.035	10, 0.035	0.9, 0.03	0.66, 0.03
β^* at IP (H,V cm)	15, 0.08	30, 0.1	100 0.16	20, 0.1	36, 0.15	1.3, 0.041	2.2, 0.048	0.8, 0.01	0.69, 0.007
Horizontal IP beam size (μm)	6.4	14	38	6.0	21	0.52	0.47	0.15	0.04
Vertical IP beam size (nm)	28	36	68	40	60	8	6	3	1
Full crossing angle (mrad)		30		33		14		20	
Crossing scheme		Crab waist		Crab waist		Crab crossing		Crab crossing	
Piwinski angle Φ	28.5	5.8	1.5	23.8	2.6	0		0	
Beam-beam parameter ξ_y (10^{-3})	133	118	128	79	109				
rf frequency (MHz)	400	400	400 and 800	650	650	1300	1300	11 994	11 994
Particles per bunch (10^{10})	17	18	23	8	15	2	2	0.52	0.37
Bunches per beam	16 640	328	48	12 000	242	1312	1312	352	312
Average beam current (mA)	1390	29	5.4	461	17.4	0.021	0.021	0.014	0.009
Injection energy (GeV)	On energy (top up)			On energy (top up)		5.0 (linac)		9.0 (linac)	
rf gradient (MV/m)	1.3	9.8	19.8	3.6	19.7	31.5	31.5	72	100
SR power loss (MW)		100		33.5	60				
Beam power/beam (MW)						5.3	10.5	3	14
Facility ac power[a] (MW)	247	270	342	157	308	129	163	168	589
Novel technology required						High gradient SC rf		Two-beam acceleration	

[a]The values for the facility ac power do not include the experiment(s) and the associated data centers.

3.2-km-long damping rings, each equipped with 54 SC wigglers, needed to assist fast damping of the beam's initially large normalized emittances to 20 nm (4 μm) in the vertical (horizontal) plane within the 200 (100) msec time between collider shots with repetition frequency $f_r = 5$ (10) Hz. Next is the ring-to-main-linac (RTML) system that includes beam lines to transport the low-emittance beams to the beginning of the main accelerators where two-stage bunch compressors squeeze the longitudinal bunch length to 0.3 mm and the beam energy increases from 5 to 15 GeV before the beams are sent into the main linacs to be accelerated to 125 GeV each.

The main linacs accelerate the beams in SC Nb cavities, each 1.04 m long and having nine cells, with a mean accelerating gradient of $31.5 - 35$ MV/m; see Fig. 5. Cryomodules with a length of 12 m provide cooling and thermal shielding of the cavities; these contain all necessary

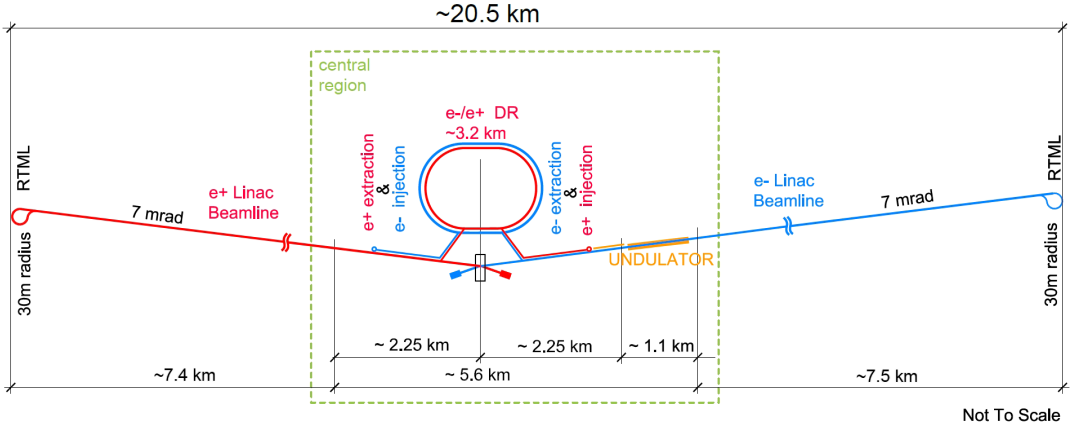

FIG. 21. Schematic layout of the ILC in the 250 GeV staged configuration. From Bambade *et al.*, 2019.

pipes for liquid and gaseous helium at various temperatures and house nine or eight such cavities plus a quadrupole unit for beam focusing. The rf power for the cavities is generated by commercially available 10 MW klystrons, with a peak efficiency of 65%. Finally, the beam-delivery system focuses the beams to the required size of 516×7.7 nm^2 at 250 GeV c.m.e. It is expected that the electron-beam polarization at the IP will be 80% (i.e., only 10% off its original level), and that the vertical beam emittance will not be more than ~75% above its original damping ring value. A feedback system, which profits from the relatively long train of 1312 bunches with interbunch separation of 554 ns, will ensure the necessary beam-beam pointing stability at the IPs. The ILC is designed to allow for two detectors mounted on movable platforms and operated in a *push-pull mode*; these detectors can be moved into and out of the beam within a day or two.

In addition to energy upgrades to $\sqrt{s} = 0.5$ and 1.0 TeV, luminosity upgrades are also possible by doubling the number of bunches per pulse to 2625 at a reduced bunch separation of 366 ns (which would require 50% more klystrons and modulators and an increased cryogenic capacity), and by an increase in the pulse repetition rate f_r from 5 to 10 Hz (which would require a significant increase in cryogenic capacity, or running at a reduced accelerating gradient after an energy upgrade). The corresponding points are indicated in Fig. 22.

After the discovery of the Higgs boson in 2012, the Japan Association of High Energy Physicists made a proposal to host the ILC in Japan and the Japanese ILC Strategy Council conducted a survey of possible sites for the ILC in Japan, eventually selecting a suitable one in the Kitakami region of northern Japan (Bambade *et al.*, 2019). The cost of the 250 GeV ILC project in Japan is estimated at 700 billion Japanese yen (with ±25% uncertainty, including the cost of labor).

The CLIC is a TeV-scale high-luminosity linear e^+e^- collider proposal that envisions three stages of construction and operation at c.m.e.'s of 380 GeV, 1.5 TeV, and 3 TeV, and a site length ranging between 11 and 50 km. What makes it distinct from the ILC is its novel two-beam acceleration scheme, in which NC copper high-gradient 12 GHz accelerating structures are powered by a high-current 1.9 GeV drive beam to efficiently enable an accelerating gradient of 100 MV/m, which is about 3 times the gradient of the ILC. For the first CLIC stage at $\sqrt{s} = 380$ GeV, which is suitable for Higgs boson studies, the optimum gradient turns out to be

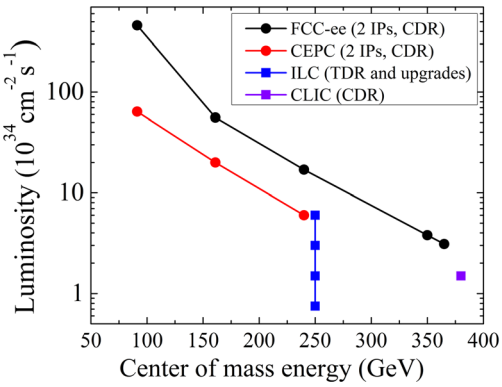

FIG. 22. Luminosity of the proposed Higgs and electroweak factories vs center-of-mass energy $\sqrt{s} = 2E_b$.

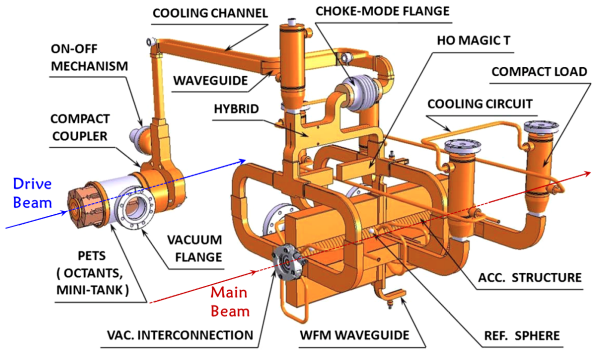

FIG. 23. Three-dimensional model of the CLIC two-beam rf module. Adapted from Aicheler *et al.*, 2012.

slightly lower, $G = 72$ MV/m (Robson *et al.*, 2018), and for this stage an alternative rf power drive option with 12 GHz klystron powering is also being considered (Aicheler *et al.*, 2019). The main parameters of CLIC are given in Table V.

The CLIC two-beam configuration is implemented by using two distinct parallel linear rf accelerating structures some 0.6 m apart, connected by a waveguide network; see Fig. 23. A low-impedance power extraction and transfer structure about 0.3 m long with a 23 mm aperture resonantly decelerates the drive beam consisting of bunches at 12 GHz repetition rate with an average gradient of about −6.5 MV/m. The kinetic energy of the drive beam is efficiently converted into the energy of 12 GHz EM waves that are extracted and sent to power two high-impedance accelerating structures (each 23 cm long with 5 mm aperture) to accelerate the main beam with a gradient of up to $G = 100$ MV/m. The maximum gradient must be achieved at nominal pulse length and shape (156 ns flat top, 240 ns full length) and with a breakdown rate (BDR) of less than $\sim 10^{-6}$, which is low enough for the reliable operation of some 20 000 structures in two linacs. This is one of the CLIC challenges, as an empirical scaling law (Braun *et al.*, 2003; Grudiev, Calatroni, and Wuensch, 2009; Dolgashev *et al.*, 2010) relates the breakdown rate, the gradient G, and the rf pulse length τ_{rf} via

$$\mathrm{BDR} \propto G^{30}\tau_{rf}^{5}. \tag{34}$$

Figure 24 presents a schematic layout of the CLIC complex. The main spin-polarized e^- beam is produced on a strained GaAs cathode in a conventional rf source and accelerated to 2.86 GeV. The beam emittance is then reduced in a damping ring. For positron beam production, a dedicated 5 GeV linac sends electrons onto a crystal to produce energetic photons, which in turn hit a second target to produce e^+. These positrons are captured, accelerated to 2.86 GeV, and sent through a series of two emittance damping rings. The CLIC RTML system accelerates 352 bunches, with 0.5 ns bunch spacing, in each electron and positron beam to 9 GeV and compresses their bunch lengths to 70 μm rms (or 44 μm for higher c.m.e.).

After the main linacs have accelerated the beams to 190 GeV, collimators in the beam-delivery system remove any transverse tails and off-energy particles, and finally the

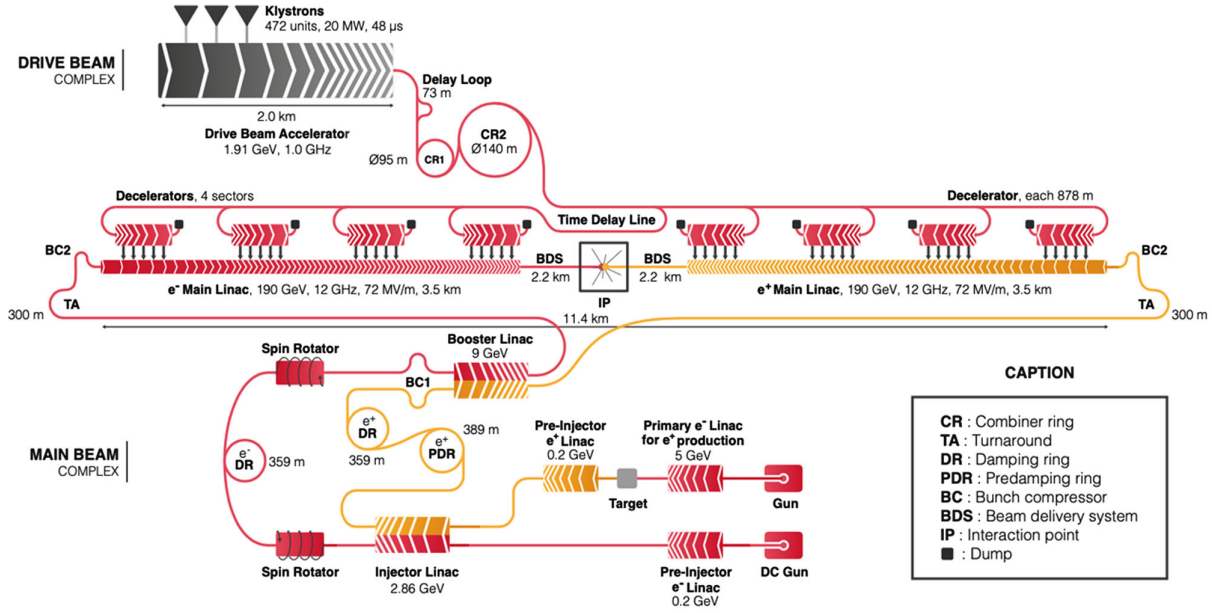

FIG. 24. CLIC accelerator complex layout at $\sqrt{s} = 380$ GeV (Stapnes).

final-focus magnets compress the beams to the required small transverse sizes at the collision point. After the collision, the spent beams are transported to a beam dump.

Every $1/f_r = 1/(50\ \text{Hz}) = 20$ ms, the 20 MW drive beam (1.91 GeV, 101 A) is generated in a 48-μs-long pulse of bunches spaced by 0.6 m in a central complex with a 1 GHz fundamental frequency of its 472 klystrons. After a sequence of longitudinal manipulations involving a delay line and two combiner rings, the initial beam is transformed into two series of four 244-ns-long final subpulses with a 12 GHz bunch spacing of 2.5 cm (i.e., 24 times the initial beam current) that are sent in opposite directions to power the two linacs; see Fig. 24. The first subpulse in each linac powers the first drive-beam decelerator, running in parallel to the colliding beam. When this subpulse reaches the decelerator end, the second subpulse has reached the beginning of the second drive-beam decelerator and will power it, running in parallel to the colliding beam, etc.

The CLIC luminosity critically depends on beam emittances (particularly vertical ones) at collision at the IP, requiring generation of e^+ and e^- beams with a minimum emittance and their tight preservation during acceleration and focusing. The latter calls for control of all relevant imperfections, such as prealignment of all the main linac and beam-delivery system components at the 10 μm level, suppression of vibrations of the quadrupoles due to ground motion to the level of 1.5 nm at frequencies above 1 Hz for the main linac (and to 0.2 nm above 4 Hz in the final-focus system) (Collette *et al.*, 2010), novel beam-based trajectory tuning methods to minimize the effect of dynamic and static imperfections using submicron resolution BPMs (Eliasson, 2008; Balik *et al.*, 2013), and mitigation of the effect of wakefields caused by high-current beams passing through misaligned accelerating structures. As a net result, between the damping ring and the IP, the CLIC vertical normalized emittance increases by less than a factor of 4.

CLIC accelerator design, technical developments, and system tests have resulted in a maximized energy efficiency and a correspondingly low power consumption of around 170 MW for the 380 GeV stage, and a total machine cost estimate of approximately 6 billion CHF (Aicheler *et al.*, 2019).

There has been significant progress in linear-collider R&D in recent years. Beam accelerating gradients met the ILC goal of 31.5 MV/m at the Fermilab FAST facility in 2017 (Broemmelsiek *et al.*, 2018) and at KEK in 2019, and they exceeded CLIC specifications at the CLEX facility at CERN, where the drive beam was used to accelerate the main beam with a maximum gradient of 145 MV/m (Robson *et al.*, 2018). The Accelerator Test Facility in KEK has also demonstrated attainment of the required vertical beam emittance in the damping ring and focusing of that beam onto 40 nm vertical rms beam size (Bambade *et al.*, 2010).

Higgs factory proposals based on linear e^+e^- colliders offer several advantages: they are based on mature technologies of NC rf and srf that have been well explored at several beam test facilities. Their designs have been developed to a sufficient level of detail. At present the ILC design is described in a TDR and the design of CLIC in a comprehensive conceptual design report (CDR). Advantageous for HEP research is also beam polarization (80% for e^- and 30% for e^+ at the ILC, 80% for e^- and 0% for e^+ at CLIC). Linear colliders are expandable to higher energies (ILC to 0.5 and 1 TeV, CLIC to 3 TeV). Both proposals have well-established international collaborations, which indicates readiness to start construction soon; their demand for ac wall-plug power of 110–170 MW is less than that of the LHC complex (~200 MW).

At the same time, one has to pay attention to the following factors: (i) the cost of these facilities equals or somewhat exceeds the LHC cost; (ii) the ILC and CLIC luminosity projections are in general lower than those for rings (see Fig. 22 and the ensuing discussion), and luminosity upgrades (such as those via a twofold increase of the number of bunches n_b and doubling the repetition rate from 5 to 10 Hz in the ILC) will probably come at additional cost; (iii) operational

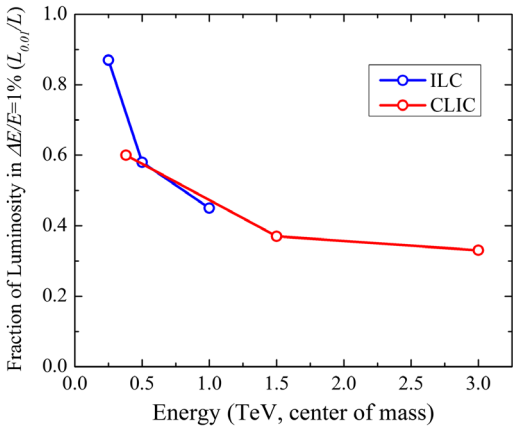

FIG. 25. Beamstrahlung effects in ILC and CLIC luminosity—fraction of the luminosity within 1% of c.m.e. vs energy.

experience with linear colliders is limited to SLAC's SLC, whose ten-year commissioning experience hints at the possible operational challenges; (iv) the CLIC's two-beam scheme is quite novel (klystrons are, therefore, a backup rf source option); and (v) ac wall-plug power demand may grow beyond 200 MW for the proposed luminosity and energy upgrades.

Linear e^+e^- colliders for TeV and multi-TeV c.m.e.'s face even more formidable challenges: their lengths grow to 40–50 km, ac power requirements become 300–600 MW (see Table V), the beamstrahlung leaves only 30%–40% of the luminosity within 1% of maximum energy (see Fig. 25) and project costs grow to $17 billion for 1 TeV ILC (the TDR cost estimate) and 18.3 billion CHF for 3 TeV CLIC (CDR).

To reach their design luminosities, both CLIC and ILC require unprecedented rates of positron production. The ILC baseline foresees about 40 times the world record set by the SLC positron source, and the ILC luminosity upgrade calls for improvement by another factor of 4. Figure 26 compares the demonstrated e^+ production rates at the SLC, KEKB, and SuperKEKB to the needs for top-up injection at future circular e^+e^- colliders, and at the collision point of future linear e^+e^- colliders.

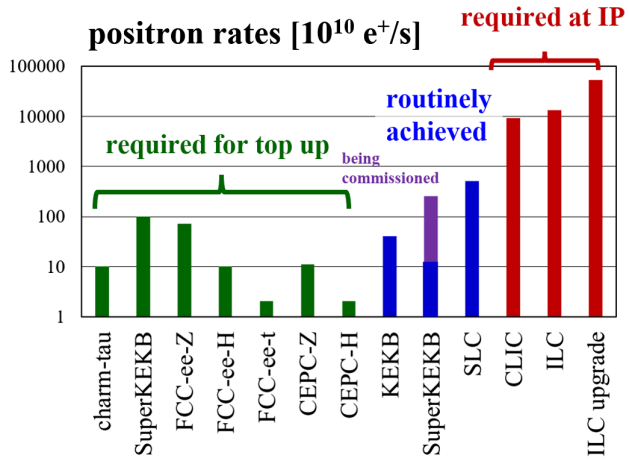

FIG. 26. Positron production rates achieved at the SLC, KEKB, and SuperKEKB compared with the need for top-up injection at future circular and linear e^+e^- colliders. Adapted from Benedikt *et al.*, 2020.

3. Circular e^+e^- colliders for the electroweak sector: FCC-*ee* and CEPC

The 2012 discovery of the Higgs boson at the LHC has stimulated interest in circular Higgs factories (Blondel *et al.*, 2013), and, in particular, in the construction of a large circular tunnel which could host a variety of energy-frontier machines, including high-energy electron-positron, proton-proton, and lepton-hadron colliders. Such projects are being developed by the global Future Circular Collider (FCC) collaboration hosted at CERN (Benedikt *et al.*, 2019a) and, in parallel, by the Circular Electron-Positron Collider (CEPC) study group based in China (CEPC Study Group, 2018), following an earlier proposal for a Very Large Lepton Collider (Sen and Norem, 2002) in the United States, which would have been housed in the 230-km-long tunnel of the Very Large Hadron Collider (VLHC) (Ambrosio *et al.*, 2001).

To serve as a Higgs factory, a new circular e^+e^- collider needs to achieve a c.m.e. of at least 240 GeV (Benedikt *et al.*, 2019b). The unprecedentedly high target luminosity $\mathcal{L}$ of FCC-*ee* and CEPC implies a short beam intensity lifetime

$$\tau_{\text{beam}} \le \frac{n_b N_e}{n_{\text{IP}} \sigma \mathcal{L}} \tag{35}$$

of the order of 1 h, due to the unavoidable radiative Bhabha scattering with a cross section of $\sigma \approx 200$ mb (Burkhardt and Kleiss, 1995). In Eq. (35) n_b signifies the number of bunches, n_{IP} indicates the number of collision points, and N represents the bunch population. The short beam lifetime due to radiative Bhabha scattering, which can be further reduced by beamstrahlung (discussed later), is sustained by quasicontinuous top-up injection. The technique of top-up injection was routinely and successfully used at both PEP-II and KEKB (Satoh, 2010; Seeman, 2015), where physics runs with nearly constant beam currents and constant luminosity were only occasionally interrupted (a few times per day) by fast beam aborts due to hardware failures. Top-up injection for FCC-*ee* or CEPC calls for a full-energy fast-ramping booster ring, with the same circumference as the collider, i.e., installed in the same tunnel.

At high energy, the performance of a circular collider is limited by synchrotron radiation. The maximum allowed beam current is directly proportional to synchrotron-radiation power P_{SR} and to the bending radius ρ, and it scales with the inverse fourth power of the beam energy E_b or the Lorentz factor γ, that is, $I_b = P_{\text{SR}}/\Delta E_{\text{SR}} \propto P_{\text{SR}}\rho/\gamma^4$; see Eq. (9). Correspondingly, the luminosity equation (28) scales as the product of the ring radius ρ, the energy-dependent beam-beam parameter ξ_y, the inverse of the IP beta function $1/\beta_y^*$, the rf power P, and with the inverse of E_b^3. The maximum beam-beam parameter increases with beam energy E_b, possibly close to linearly (Assmann and Cornelis, 2000), but it may ultimately be limited to about $\xi_y = 0.13$ by a new type of beam-beam instability occurring for collisions with a nonzero crossing angle (Ohmi *et al.*, 2017; Kuroo *et al.*, 2018). Average beam energy loss per turn due to the synchrotron radiation varies between 0.1% and 5% (from Z energy to 365 GeV), and at the higher energies it is significantly larger than the equilibrium energy spread due to beamstrahlung,

which can be of the order of 0.1%–0.2%. It is worth noting that, in the lower-energy running modes of the circular Higgs and electroweak factories (Z and WW runs), the beamstrahlung significantly increases the energy spread and bunch length, by up to a factor of 3 of 4 over what would be obtained without collisions, i.e., with the natural bunch length set by the quantum fluctuation in the low-field collider arcs. This large relative increase of the energy spread due to beamstrahlung is due to the weak radiation damping at these lower energies, where each electron or positron emits multiple beamstrahlung photons during one radiation damping time. At the higher beam energies, especially for $t\bar{t}$ operation, radiation damping is stronger and the energy spread increase due to beamstrahlung becomes much less pronounced. However, here the single emission of hard beamstrahlung photons at the collision point introduces an additional limit on the beam lifetime (Telnov, 2013), which is about 20 min even in a sophisticated crab-waist optics, with $\beta_y^* = 0.8$–1.6 mm, that features a large energy acceptance (Bogomyagkov, Levichev, and Shatilov, 2014).

The FCC-ee would be installed in a ∼100 km tunnel, which can afterward host a 100 TeV hadron collider (FCC-hh; discussed later). The FCC complex would be connected to the existing CERN infrastructure. CEPC is a project under development in China (CEPC Study Group, 2018) that is similar to FCC-ee. CEPC would also be followed by a highest-energy hadron collider in the same tunnel, called the Super Proton-Proton Collider (SppC).

FCC-ee operation is staged, starting on the Z pole (91 GeV c.m.e.) with approximately 10^5 the luminosity of the previous LEP collider, then operating at the WW threshold (160 GeV), followed by the Higgs production peak (240 GeV), and finally at the $t\bar{t}$ threshold (365 GeV). An optional FCC-ee run at 125 GeV for direct Higgs production with monochromatization (Valdivia García and Zimmermann, 2019) could access the Higgs-electron Yukawa coupling (d'Enterria, 2017; Blondel and Janot, 2019). This possibly constitutes the only available path to address the origin of the electron mass. On the Z pole and at the WW threshold, radiative self-polarization allows for an extremely precise c.m.e. energy calibration, at the 10^{-6} level, based on resonant depolarization (Blondel *et al.*, 2019). Even at the highest FCC-ee collision energy, 365 GeV c.m.e., the luminosity, limited by 100 MW of synchrotron-radiation power, would still exceed 10^{34} cm^{-2} s^{-1} at each of two or four collision points. The FCC-ee srf system is optimally adapted for each mode of operation; i.e., it is optimized for the respective beam current and the rf voltage required. Specifically, at the Z pole, the FCC-ee deploys single-cell 400 MHz Nb/Cu cavities, while at the WW threshold and the ZH production peak 400 MHz five-cell Nb/Cu cavities will operate at 4.5 K. For $t\bar{t}$ running they will be complemented by additional 800 MHz bulk Nb cavities at 2 K. In addition, at the $t\bar{t}$ energy, all the rf cavities are shared by the two beams, in common rf straights, which saves cost and is possible thanks to the small number of bunches in this mode of operation.

CEPC operation is scheduled to start at the Higgs production peak (240 GeV c.m.e.), continues on the Z pole (91 GeV), and ends with the WW threshold (160 GeV). Operation at the $t\bar{t}$ energy is not foreseen; see Fig. 22. CEPC deploys the same two-cell 650 MHz bulk Nb cavities at all beam energies. However, the total number of installed rf cavities varies from 240 (240 GeV) to over 120 (91 GeV) to 216 (160 GeV) in the three modes of operation. At the highest initial center-of-mass energy of 240 GeV the 240 installed cavities are shared by the two beams. The impedance and higher-order mode power of the 650 MHz rf cavities limit the projected CEPC luminosity at the Z pole to a value about a factor of 7 lower than for FCC-ee (Fig. 22).

The optics designs of FCC-ee (Oide *et al.*, 2016) and CEPC contain several novel features, which boost their performance. For the crab-waist collision scheme, a large crossing angle is needed and 30 mrad was found to be optimal for FCC-ee; for CECP a similar value of 33 mrad has been chosen. The two colliding beams always approach the IP from the inside, with bending magnets on the incoming side selected to be so weak that, for the FCC-ee, the critical energy of the photons emitted toward the detector stays below 100 keV over the last 450 m from the IP, even at the highest beam energy for $t\bar{t}$ operation (365 GeV c.m.e.). Similarly, for CEPC in ZH production mode (240 GeV), the critical energy of the synchrotron-radiation photons is less than 120 keV over the last 400 m upstream of the IP.

As a result, the FCC-ee and CEPC final-focus optics are asymmetric; see Fig. 27 for the FCC-ee. Figure 28 illustrates how asymmetric bending also separates the FCC-ee collider IP from the beam line of the full-energy top-up booster by more than 10 m, leaving sufficient space for the experimental detector. The CEPC layout is similar.

Stronger magnets and a shorter final-focus system are installed on the outgoing side of the IP. Each final focus accommodates a pair of sextupoles, separated by a *minus identity* ($-I$) optics transformer, to accomplish a local correction of the vertical chromaticity. Thanks to the $-I$ transformer, geometric aberrations can be exactly canceled between the two sextupoles of a pair. However, by design, the dominant aberration generated when reducing the strength

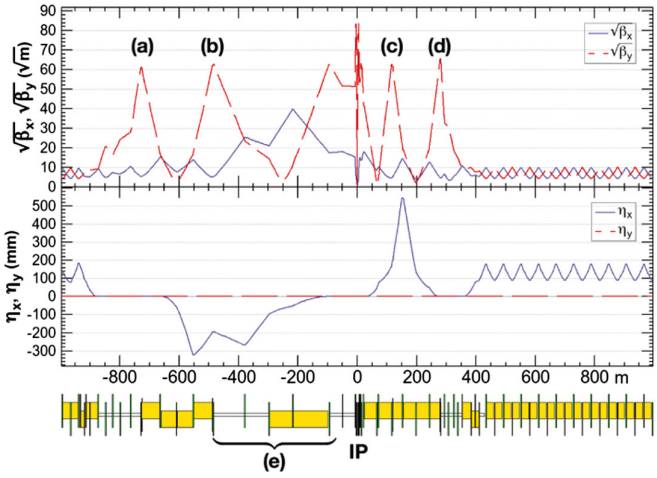

FIG. 27. Asymmetric final-focus optics of FCC-ee, featuring four sextupoles (a)–(d) for local vertical chromaticity correction combined with a virtual crab waist (see the text for details) (Oide *et al.*, 2016; Benedikt *et al.*, 2019a).

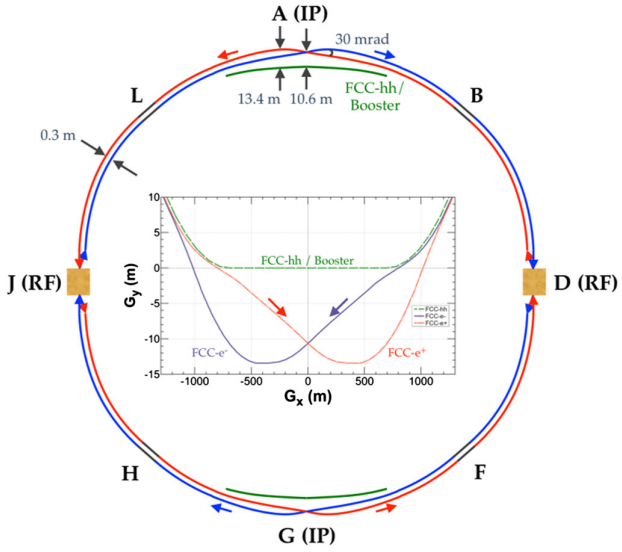

FIG. 28. Layout of the FCC-*ee* double-ring collider with two long rf straights and two interactions points, sharing a tunnel with the full-energy top-up booster (Oide *et al.*, 2016; Benedikt *et al.*, 2019a).

of the outer sextupole of the pair results in the desired crab waist at the IP, while maintaining the chromatic correction. Hence, instead of adding one more sextupole as for the crab-waist implementation in other colliders, the FCC-*ee* utilizes an elegant and novel *virtual crab-waist* scheme. Here, the total number and strength of nonlinear magnets is even reduced, compared with the case of no crab waist, with a positive effect on the dynamic aperture.

The synchrotron-radiation power incident per unit length in the arcs of the circular Higgs factories is significantly lower than at several previous colliders and storage-ring light sources. However, for the highest beam energy of 182.5 GeV at FCC-*ee*, the critical photon energy of 1.06 MeV in the arcs exceeds the corresponding value of 0.83 MeV reached at LEP2 [a maximum value of 1.4 MeV was considered during the LEP design (Nelson and Tuyn, 1979)]. As in LEP, the high-energy fraction of the synchrotron photons will activate surrounding material through (γ, n) reactions. According to simulations, for FCC-*ee* operation at 365 GeV c.m.e., the residual dose rate will reach a few tens of μSv/h along the beam line immediately after the beam is stopped, which would decay to less than 1 μSv/h within a few days (Benedikt *et al.*, 2019a).

Both FCC-*ee* and CEPC proposals call for high srf power transfer to beams (100 MW in FCC-*ee* and 60 MW in CEPC), leading to total site power of about 300 MW (Table V). Cost estimate of the FCC-*ee* is 10.5 billion CHF (plus an additional 1.1 billion CHF for the option to operate at the higher $t\bar{t}$ energy) and \$5 billion to \$6 billion for the CEPC ("less than 6 billion CHF" is cited in the CEPC CDR).

The advantages of circular Higgs factories include a mature srf acceleration technology, with vast operational experience from numerous other rings, suggesting a lower performance risk, along with a higher luminosity and better luminosity-to-cost ratio. They can also host detectors at several (2 to 4) IPs, which could further strengthen their role as *electroweak factories*. The 100-km-long tunnels can be reused, and are required, by follow-up future pp colliders.

Transverse polarization occurs naturally at Z and W energies and can be employed, with the help of pilot bunches and, possibly, polarization wigglers at the Z energy, for precise energy calibration at the 100 keV level.

The FCC Collaboration has issued a CDR (Benedikt *et al.*, 2019a) that addresses key design points and indicates a possible start date of 2039. The schedule of the CEPC CDR (CEPC Study Group, 2018) is more aggressive and foresees a start of machine operation some 7–9 yr sooner. Prior to this, the FCC and CEPC R&D programs are expected to address several important items, such as high-efficiency rf sources (such as targeting over 85% for 400 and 800 MHz klystrons, up from the current 65%), high-efficiency srf cavities (to achieve a 10–20 MV/m cw gradient and a high cavity quality factor Q_0, and to develop new technologies like advanced Nb-on-Cu or Nb_3Sn cavities), the exploration of the crab-waist collision scheme (the SuperKEKB experience will be extremely helpful in this regard), energy storage and release (so that the energy stored in cycling magnets can be reused), and the efficient usage of excavated materials (some 10×10^6 m^3 will need to be taken out of a 100 km tunnel).

Circular machines like FCC-*ee* and CEPC make the same particle bunches collide over many turns. The luminosity of these colliders is almost directly proportional to the total electric power, both of which can be varied through changing the number of bunches. In the proposed energy range from the Z pole up to the $t\bar{t}$ threshold, the circular machines can operate with a high efficiency in terms of total luminosity per electrical power (Ellis *et al.*, 2019; Benedikt *et al.*, 2020). However, the beam energy lost per turn due to synchrotron radiation increases with the fourth power of energy [Eq. (9)], and this effect ultimately limits the maximum energy of circular colliders, via the available rf voltage, at about 400 GeV c.m.e. To raise the collision energy further, up to 600 GeV, or to boost the e^+e^- luminosity, a possible ERL-based upgrade of a circular collider like FCC-*ee* has been proposed (Litvinenko, Roser, and Chamizo-Llatas, 2020), where a low-emittance beam is accelerated and decelerated over several turns, before and after the collision, respectively; see also Sec. V.B. This proposal is in an early, exploratory stage. By contrast, the long-established linear-collider designs of ILC or CLIC presented in Sec. IV.B.2 can reach e^+e^- collision energies of 1 TeV or above.

C. Energy-frontier colliders (HE-LHC, FCC-*hh*, SppC, and muon colliders)

Several hadron and lepton colliders have been proposed to extend the energy reach beyond the present LHC at CERN. The physics program that could be pursued by a next-energy-frontier collider with sufficient luminosity would include understanding the mechanism behind mass generation, the Higgs mechanism, and the role of the Higgs boson in the electroweak symmetry breaking; answering the question as to whether the Higgs boson is a fundamental or composite particle; searching for, and possibly discovering, supersymmetric or other exotic particles, which could be part of the Universe's dark matter; and hunting for signs of extra

spacetime dimensions and quantum gravity (Arkani-Hamed *et al.*, 2016; Quigg, 2019). As previously alluded to, ambitious plans have been proposed to upgrade the FCC and CEPC to hadron colliders (FCC-*hh* and SppC, respectively) by means of next-generation or next-next-generation SC magnets installed in the arc sections of the 100 km rings, so as to enable collision energy of the order of 100 TeV or above (CEPC Study Group, 2018; Benedikt *et al.*, 2019b). As for the lepton colliders, there is a growing community interest in cost-efficient muon colliders that can possibly provide collision energies ranging from 3 to 14 TeV, which is significantly beyond the reach of practical e^+e^- linear colliders.

1. Post-LHC hadron colliders

Circular hadron colliders are known as discovery machines. Their discovery reach is determined by beam energy, which depends on only two parameters: the dipole magnetic field B and the bending radius ρ, $E_{\mathrm{c.m.}} \propto \rho B$; see Eq. (5). Historically, new colliders have always been larger and used stronger magnets than their predecessors. The Tevatron near Chicago was the first hadron collider based on SC magnet technology, with a dipole field of 4.2 T, and it was installed in a 6.3 km ring. In comparison, the LHC uses 8.3 T dipoles in a 26.7 km tunnel. A proposed high-energy "upgrade" of the LHC based on 16 T Nb_3Sn SC magnets [the High-Energy LHC (HE-LHC)] would allow for 27 TeV c.m.e. hadron collisions reusing the LHC tunnel (Zimmermann *et al.*, 2019). A further increase in the collider size by a factor of about 4 relative to the LHC, i.e., to a circumference of roughly 100 km, yields a c.m.e. of 100 TeV with similar 16 T dipole magnets (Future Circular Collider, hadron version "FCC-*hh*") (Benedikt *et al.*, 2019c). This goal defines the overall infrastructure requirements for the FCC accelerator complex. A proton-electron collision option (FCC-*he*) calls for a 60 GeV electron beam from an ERL (the same as for the LHeC), which would collide, at a single interaction point, with one of the two 50 TeV proton beams circulating in the FCC-*hh*; see Sec. IV.A.4.

CEPC and SppC are two colliders similar to FCC-*ee* and FCC-*hh* that are being studied by another international collaboration, centered at IHEP Beijing (CEPC Study Group, 2018). These two machines have almost the same circumference as the FCC, about 100 km. Several possible locations in China are under study. The SppC hadron collider relies on 12 T (later 24 T) iron-based high-temperature superconducting magnets, which could be installed in the same tunnel as the CEPC. Table VII compiles key parameters of the HE-LHC, FCC-*hh*, and SppC.

Figure 29 indicates the proposed location of the FCC in the Lake Geneva basin, connected to the existing CERN-LHC accelerator complex. The principal structure for the successively installed FCC lepton and hadron colliders (FCC-*ee* and FCC-*hh*) is a quasicircular 97.75-km-long tunnel composed of arc segments interleaved with straight sections. Approximately 8 km of bypass tunnels, 18 shafts, 14 large caverns, and 12 new surface sites are also planned. The tunnel location and depth were optimized by taking the local geology into account.

Collider luminosity should ideally increase with the square of the energy since cross sections decrease as the inverse square of energy. However, because of the nonlinear parton distribution inside the colliding protons, even a lower luminosity can produce exciting physics, with the most important parameter of a hadron collider remaining its energy. Nevertheless, at a given energy the discovery reach grows with higher luminosity (Teng, 2001; Salam and Weiler, 2019): this is one of the motivations for upgrading the LHC to the HL-LHC. The LHC design has already dramatically increased luminosity relative to previous machines. Much higher luminosities are still expected for the proposed HE-LHC and FCC-*hh*, and also for the approved HL-LHC, which will lower its peak luminosity by *leveling* in order to make it acceptable for the physics experiments (Benedikt, Schulte, and Zimmermann, 2015). A high instantaneous luminosity would result in an event pileup per bunch crossing of the order of 500 (from up to 50 in LHC), and for the HL-LHC experiments this could significantly degrade the quality of the particle detector data collected for the physics analysis. The technique of luminosity leveling allows one to sustain the operational luminosity, and the associated event pileup, at a constant level over a significant length of time via one of several techniques: (i) a gradual reduction of the beta function at the interaction point β^*, (ii) crossing angle variation, (iii) changes in the rf voltage of crab cavities or more sophisticated crabbing schemes (Fartoukh, 2014), (iv) dynamic bunch-length reduction, or (v) controlled variation of the transverse separation between the two colliding beams. Of note is that the luminosity of the highest-energy hadron colliders, such as HE-LHC and FCC-*hh*, profits from significant radiation damping due to the associated high beam energies and magnetic fields. This radiation damping will naturally level their luminosity evolution.

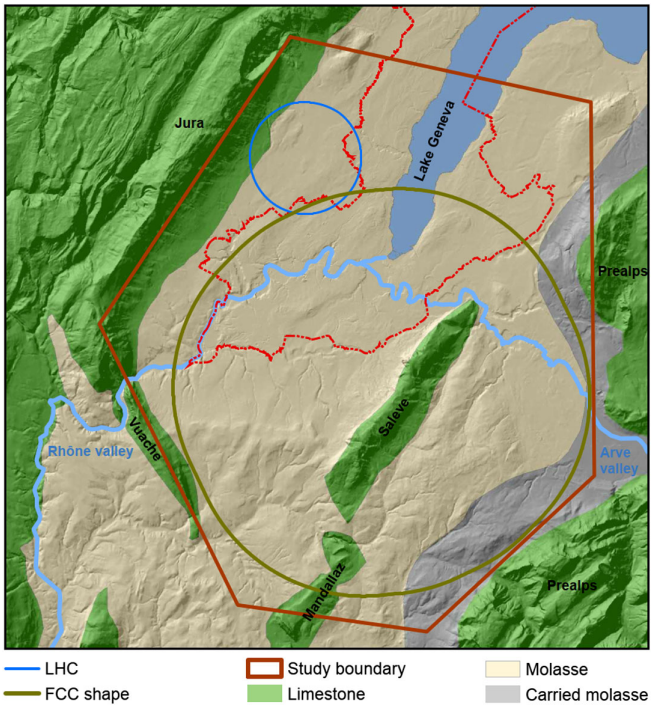

FIG. 29. Study boundary (red polygon) showing the main topographical and geological structures, LHC (blue line) and FCC tunnel trace (brown line) (Benedikt *et al.*, 2019a, 2019c).

Hadron-collider luminosity will increase linearly with energy due to the shrinking beam sizes $\sigma^*_{x,y} = \sqrt{\beta^*_{x,y}\varepsilon_{nx,y}/\gamma}$ when the normalized beam emittances, beam currents, the beta functions at the IP, $\beta^*_{x,y}$, and beam-beam tune shift are kept constant. Even higher luminosity can be achieved by reducing the IP beta functions. To date all hadron colliders, starting from the ISR, have operated with similar beta functions, with minimum values of about 0.3 m (see Table VI). With a value of 0.15 m (or even 0.10 m) the HL-LHC will set a new record. An ongoing study aims at pushing the FCC-*hh* β^* down to 5 cm (Martin *et al.*, 2017).

For proton-proton colliders with many bunches, such as the HL-LHC and FCC-*hh*, a crossing angle is required to avoid or mitigate parasitic beam-beam collisions. This crossing angle needs to be increased as $\beta^*_{x,y}$ is reduced. Without countermeasures, this would dramatically degrade the geometric overlap of the colliding bunches and all but eliminate any benefit from reducing the IP beam size. To avoid such a degradation, the HL-LHC, HE-LHC, and FCC-*hh* will all use novel crab cavities (Verdu-Andres *et al.*, 2016). In 2018, the first beam tests of such crab cavities with protons were successfully performed at the CERN SPS (Carver *et al.*, 2019).

Future hadron colliders will be characterized by record high stored beam energy, rendering machine protection a paramount concern. A challenging multistage collimation system is needed to avoid local beam loss spikes near cold magnets, which would induce magnet quenches. Beam injection and beam extraction are particularly sensitive operations, as injection or dump kickers are among the fastest elements in the machine. The collider design must be robust against the sudden asynchronous firing of a kicker unit. The collimators are likely to be the first element to be hit by the beam in case of any fast failure and must be able to withstand the impact of one or a few bunches. The primary and secondary collimators of the LHC are based on carbon–carbon composite material. For the HL-LHC and future hadron colliders, ever stronger materials are being developed and examined that also feature higher conductivity and, hence, lower impedance. More advanced options include the use of short bent crystals as primary collimators (Scandale *et al.*, 2016) and the deployment of *hollow electron-beam lenses* as nondestructible collimators (Stancari *et al.*, 2011). Acceptable performance of the collimation system, along with small IP beta function, also requires excellent optics control.

TABLE VI. Beta-function values β^* at IPs of hadron colliders. Adapted from Tomas, 2017.

Collider	β^*_x (m)	β^*_y (m)
ISR	3.0	0.3
S$p\bar{p}$S	0.6	0.15
HERA-*p*	2.45	0.18
RHIC	0.50	0.50
Tevatron	0.28	0.28
LHC	0.3	0.3
HL-LHC	0.15 (0.10)	0.15 (0.10)
HE-LHC	0.25	0.25
FCC-*hh*	1.1 → 0.3 (0.05)	1.1 → 0.3 (0.05)
SppC	0.75	0.75

In view of the substantial ring circumference and the associated low momentum compaction, hadron-beam intensity in large accelerators may be limited by conventional instabilities. In particular, the resistive wall instability becomes a concern due the low revolution frequency, and TMCI could appear at injection due to the low synchrotron tune (Burov *et al.*, 2000; Shiltsev, 2015).

For future higher-energy hadron colliders, synchrotron-radiation damping becomes significant. In such a situation, longitudinal emittance needs to be kept constant during the physics store through controlled longitudinal noise excitation in order to maintain longitudinal Landau damping (Zimmermann, 2001a). At the same time, the transverse emittance shrinks due to strong radiation damping, while proton intensity rapidly decreases as a result of the *burn off* due to the high luminosity. The initial proton burn-off time can be computed as

$$\tau_{\rm bu} = \frac{N_p n_b}{\mathcal{L}_0 \sigma_{\rm tot} N_{\rm IP}}, \tag{36}$$

where N_p denotes the proton bunch population, $\mathcal{L}_0$ indicates the initial luminosity, $\sigma_{\rm tot}$ is the total proton-proton cross section, n_b denotes the number of bunches per beam, and $N_{\rm IP}$ is the number of high-luminosity IPs; $N_{\rm IP} = 2$ for all three colliders under consideration. The total hadron cross section grows with the c.m.e. collision energies [see Tanabashi *et al.* (2018), Chap. 46], which implies shorter beam lifetimes for higher-energy hadron colliders even at a constant target luminosity and could strain requirements on the machines' injector chains.

For the FCC-*hh*, the emittance damping time is shorter than the proton burn-off time. As a result, the total beam-beam tune shift $N_{\rm IP}\xi$ increases during the store. At some point, the beam-beam limit is reached, and, from this point onward, the transverse emittance must be controlled by transverse noise excitation, so as to keep the beam-beam tune shift at or below the empirical limit. This limit determines the further luminosity evolution during the store and the optimum run-time (Benedikt, Schulte, and Zimmermann, 2015). By contrast, at the HE-LHC, the proton burn-off time is slightly shorter than the radiation damping time. This situation is qualitatively different than that of the FCC-*hh*. For the HE-LHC, there is almost a natural luminosity leveling, while the beam-beam tune shift naturally decreases during the store.

The primary technology for future hadron colliders will be high-field magnets, both dipoles and quadrupoles. Magnets made from Nb-Ti superconductors were the core technology of the present LHC, Tevatron, RHIC, and HERA. Nb-Ti magnets are limited to maximum fields of about 8 T. The HL-LHC will, for the first time in a collider, use some tens of dipole and quadrupole magnets with a peak field of 11 to 12 T, based on a new high-field magnet technology using a Nb_3Sn superconductor. This will prepare the ground for the development of 16 T Nb_3Sn magnets, and for the later production of about 5000 Nb_3Sn magnets required by the FCC-*hh*. The Chinese SppC magnets will utilize cables based on an iron-based high-temperature superconductor, a material discovered at the Tokyo Institute of Technology in 2006 (Kamihara *et al.*,

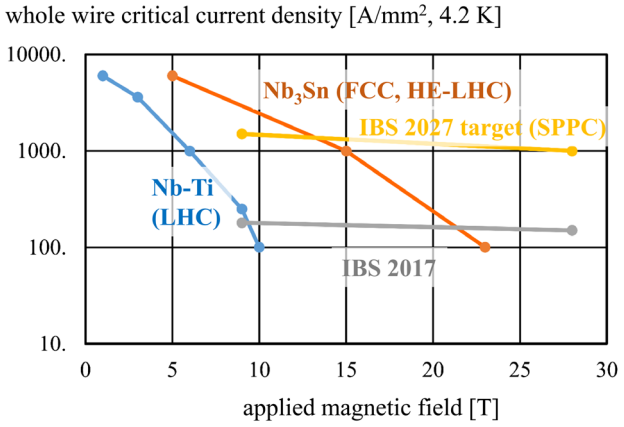

FIG. 30. Field limits for LHC-type Nb-Ti conductor, Nb_3Sn conductor as used for HL-LHC, FCC-*hh*, and HE-LHC, and iron-based superconductor (present and 10-yr forecast) for SppC [after Lee (2019)], and private communication with Gao (2017). From Benedikt and Zimmermann, 2018.

2006). Figure 30 sketches the respective current densities and field limits. It is clear that Nb_3Sn can approximately double the magnetic field reached with Nb-Ti. The R&D target for SppC looks aggressive. The SppC goal is to increase magnet performance 10 times while simultaneously reducing its cost by an order of magnitude. If successful, the iron-based HTS magnet technology could become a game changer for future hadron colliders.

Also important is the minimum field of SC magnets allowing for efficient operation. This minimum field is determined by balancing various considerations, such as the injected beam size and magnet aperture, the magnetic field quality at injection, machine protection against accidental beam loss due to injection-system failures, beam losses, injection kicker system strength and rise time, severity of beam instabilities, and overall cost. Typically, the dynamic range (energy swing) of SC circular accelerators lies in the range 10–20. An increase in c.m.e. might imply additional acceleration stages in the injector complex, thereby potentially affecting the overall cost, the collider filling time, and the overall machine efficiency.

Recently several important milestones were accomplished in the development of high-field Nb_3Sn magnets. In the United States, a Fermi National Accelerator Laboratory (FNAL) team completed a 15 T accelerator dipole short-model demonstrator (Zlobin *et al.*, 2019). Following a staged approach, as a first step this magnet was prestressed for a maximum field of about 14 T, and in 2019 its field indeed reached 14.1 T at 4.5 K (Zlobin *et al.*, 2020). In 2020 a field of 14.5 T was achieved at 1.9 K. In addition to development of optimized magnet design concepts (Caspi *et al.*, 2014), a higher field can be facilitated by using a higher-quality conductor. Advanced U.S. wires with artificial pinning centers (APCs) produced by two different teams (FNAL, Hyper Tech Research, and Ohio State University, and NHMFL Collaboration along with Florida A&M University and Florida State University) have reached the target critical current density for FCC of 1500 A/mm^2 at 16 T (Balachandran *et al.*, 2019; Xu *et al.*, 2019), which is 50% higher than for the HL-LHC wires. The APCs allow for better performance; they decrease magnetization heat during field ramps, improve the magnet field quality at injection, and reduce the probability of flux jumps (Xu *et al.*, 2014).

Another important technology is the cryogenic beam vacuum system, which has to cope with unusually high levels of synchrotron radiation (about 5 MW in total for FCC-*hh*) in a cold environment. The design of the beam screen intercepting the radiation inside the cold bore of the magnets and the choice of its operating temperature (50 K, which is significantly higher than the 5–20 K chosen for the LHC beam screen) are key ingredients of the FCC-*hh* design. The first hardware prototypes for FCC-*hh* were tested in 2017 at the Karlsruhe Institute of Technology ANKA-KARA facility at Karlsruhe, Germany, with synchrotron radiation from an electron beam whose spectrum and flux resembled those of the FCC-*hh*. These beam measurements at the ANKA-KARA facility validated the basic design assumptions (Gonzalez *et al.*, 2019). The latest version of the FCC-*hh* beam screen design is shown in Fig. 31.

Other key technologies of energy-frontier hadron colliders include the collimators, the kicker and septa required for the extremely high beam energy, and the SC rf systems for acceleration and for compensation of synchrotron-radiation energy losses, as well as for ever more demanding crab cavities.

The tunnel is a core element of any new collider. The FCC-*hh* (FCC-*ee*) and SppC (CEPC) tunnels are to be constructed differently, using tunnel boring machines and drill or blast techniques, respectively. The tunnel shapes and sizes are also different, as illustrated in Fig. 32. The HE-LHC must fit into the existing LHC tunnel, with a diameter of 3.8 m. The HE-LHC dipole magnets must, therefore, be made as compact as possible, with a maximum outer diameter of 1.2 m. In addition, half-sector cooling is proposed to reduce the diameter of the cryogenics lines and relax tunnel integration, calling for additional 1.8 K refrigeration units. The new round tunnel for the FCC-*hh* will have a significantly larger diameter of 5.5 m, to host the possibly larger 16 T magnets and enlarged

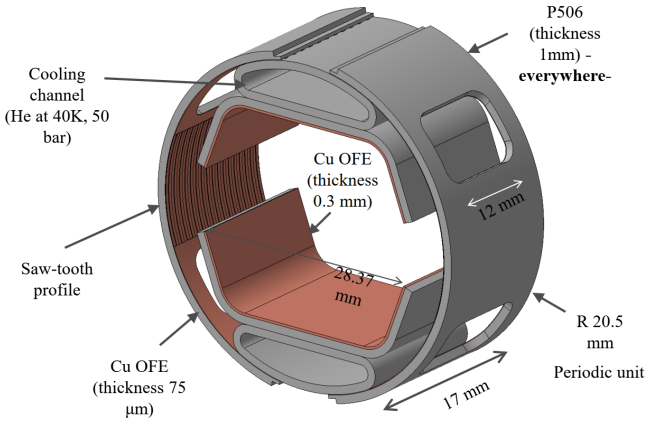

FIG. 31. A periodic unit of the FCC-*hh* vacuum beam screen, which will be mounted inside the magnet cold bore (1.9 K) (Bellafont *et al.*, 2020). This beam screen will be operated at an elevated temperature of about 50 K for efficient removal of the heat from synchrotron radiation.

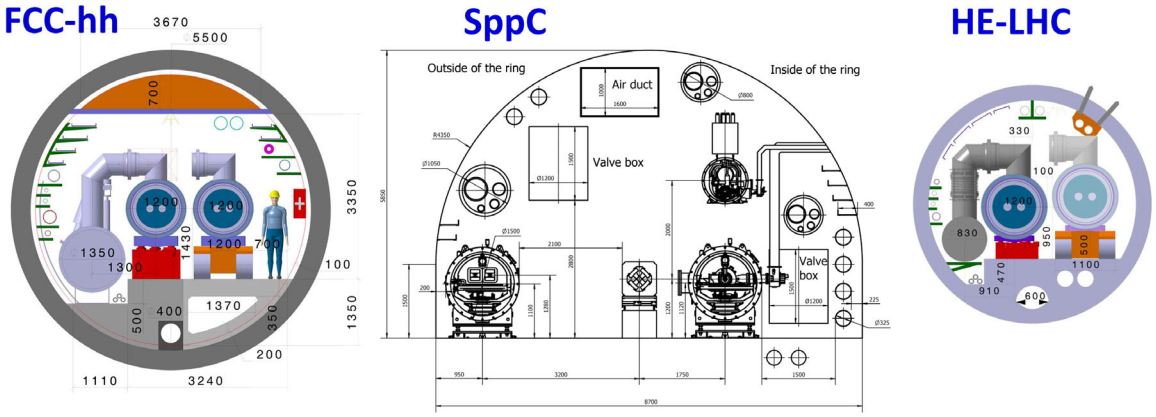

FIG. 32. Tunnel cross sections for FCC-*hh*, SppC, and HE-LHC depicted approximately to scale. From Benedikt and Zimmermann, 2018.

cryogenics lines and allow for additional safety features, such as smoke extraction, ventilation, and escape passages. This tunnel still does not offer enough space to accommodate both a lepton and a hadron machine at the same time. If the FCC-*ee* is built as a first step, it will need to be disassembled prior to the installation of the FCC-*hh* hadron collider. The SppC tunnel is even larger, with a transverse width of 8.7 m. It is meant to provide enough space for both lepton and hadron machines, also including a lepton booster ring for top-up injection, which, in principle, could all be operated in parallel.

The HE-LHC cryogenic system reuses the existing LHC helium refrigerators, which will be upgraded by doubling the number of 1.8 K refrigeration units (two units per sector instead of one) and by adding specific refrigeration units for temperatures above 40 K to handle, in particular, the beam-induced heat load on the beam screens, which is dominated by the synchrotron-radiation power of about 190 kW. It should be noted that by 2040 some of the existing LHC cryoplants will be 50 years old, and that the associated aging issues need to be carefully studied. In view of their much larger circumference and high synchrotron-radiation power, the FCC-*hh* and SppC will both still need substantially larger cryogenic facilities. Specifically, the FCC-*hh* foresees ten cryoplants, each with 50–100 kW at 4.5 K including 12 kW at 1.8 K, and requiring a helium inventory of 800 tons, about 6 times the helium inventory of the present LHC. The FCC-*hh* will use a cryogenics system based on a neon-helium mixture (nelium), which leads to electrical energy savings of about 10% with respect to the LHC-type helium cryogenics infrastructure The electrical power consumption of the FCC-*hh* cryoplants is about 200 MW (Chorowski *et al.*, 2017).

To summarize, the key challenges for the energy-frontier pp colliders such as the HE-LHC, FCC-*hh*, and SppC are associated with the need for long tunnels (27, 100, and 100 km, respectively), high-field SC magnets (16, 16, and 12 T, respectively), and total ac site wall-plug power ranging from about 200 MW (HE-LHC) to ∼500 MW. The cost estimates extend from 7.2 billion CHF for the HE-LHC to 17.1 billion CHF for the FCC-*hh* (assuming that the 7 billion CHF tunnel is available); see Table VII. In all these options, the detectors will need to operate at luminosities of $O(10^{35}\ \mathrm{cm}^{-2}\,\mathrm{s}^{-1})$ and the corresponding pileup of events per crossing will be $O(500)$. A 12–18-yr-long R&D program is foreseen to address the most critical technical issues, such as (i) development of accelerator quality 16 T dipole magnets based on Nb_3Sn (or 12 T iron-based HTS magnets for the SppC), (ii) effective interception of synchrotron radiation (5 MW in FCC-*hh* and 1 MW in SppC), (iii) beam halo collimation with circulating beam power 7 times that of the LHC, (iv) choice of optimal injector (such as a new 1.3 TeV SC SPS, or a 3.3 TeV ring in either the LHC tunnel or the FCC tunnel, for the FCC-*hh*), and (v) overall machine design issues (IRs, pileup, vacuum, etc.), power and cost reduction, etc. It is noteworthy that such machines can additionally be used for ion-ion or ion-proton collisions; high-energy proton beams can also be made to collide with high-intensity $O(60)$ GeV electrons from an ERL.

2. Muon colliders

The lifetime of the muon, 2.2 μs in the muon rest frame, is sufficient to allow fast acceleration to high energy before the muon decays into an electron, a muon-type neutrino, and an electron-type antineutrino ($\mu^- \to e^- \nu_\mu \bar{\nu}_e$) and storage for some $300 \times B$ turns in a ring with average field B (tesla). The muon-to-electron-mass ratio of 207 implies that all synchrotron-radiation effects are smaller by a factor of about $(m_\mu/m_e)^4 \approx 2 \times 10^9$. Even a multi-TeV $\mu^+\mu^-$ collider can be highly power efficient while being circular, and therefore may have quite a compact geometry that will fit on existing accelerator sites or tunnels. The c.m.e. spread for 3 to 14 TeV $\mu^+\mu^-$ colliders is $dE/E < 10^{-3}$ (see the parameters of such facilities in Table VII), which is an order of magnitude smaller than for an e^+e^- collider of the same energy. As in e^+e^- colliders, the muon collider center-of-mass energy $\sqrt{s}$ is entirely available to produce short-distance reactions rather than being spread among proton constituents. A 14 TeV muon collider with sufficient luminosity might be effective as a direct exploration machine, with a physics potential similar to that of a 100 TeV proton-proton collider; see Fig. 33.

In general, muon colliders are predicted to be significantly less expensive than other energy-frontier hadron or e^+e^- machines (Shiltsev, 2014). They need lower ac wall-plug power (Delahaye, 2018; Boscolo, Delahaye, and Palmer,

TABLE VII. Tentative parameters of selected future high-energy hadron and muon colliders. Parameters of the $\mu^+\mu^-$ Higgs factory are given for reference only. An estimate for SppC ac power is not yet available.

	HE-LHC	FCC-*hh*	SppC	$\mu\mu$ collider		
Species	*pp*	*pp*	*pp*		$\mu^+\mu^-$	
Beam energy (TeV)	13.5	50	37.5	0.063	3	7[a]
Circumference (km)	26.7	97.75	100	0.3	6	26.7
Interaction regions	2 (4)	4	2	1	2	2
Peak luminosity (10^{34} cm^{-2} s^{-1})	15	5 – 30	10	0.008	12	33
Integrated luminosity per expt. (ab^{-1}/yr)	0.5	0.25–1.0	~0.4	0.001	1.0	3
Time between collisions (μs)	0.025	0.025	0.025	1	20	90
Events per crossing	800	170 – 1000	~300	...	...	...
Energy spread (rms, 10^{-3})	0.1	0.1	0.2	0.04	1	1
Bunch length (rms, mm)	80	80	75.5	63	2	1
IP beam size (μm)	6.6	6.8 (initial)	6.8 (initial)	75	1.5	0.6
Injection energy (GeV)	1300	3300	2100		On energy	
Transverse emittance (rms normalized, μm)	2.5	2.1 (initial)	2.4 (initial)	200	25	25
β^*, amplitude function at IP (cm)	45	110 – 30	75	1.7	0.25	1
Beam-beam tune shift/ IP (10^{-3})	5	5 – 15	7.5	20	90	100
rf frequency (MHz)	400	400	400/200	805	805	805
Particles per bunch (10^{10})	22	10	15	400	200	200
Bunches per beam	2808	10 600	10 080	1	1	1
Average beam current (mA)	1120	500	730	640	16	4
Length of standard cell (m)	137	213	148	...	...	...
Phase advance per cell (deg)	90	90	90	...	...	...
Peak magnetic field (T)	16	16	12 (24)	10	10	16
SR power loss/beam (MW)	0.1	2.4	1.2	0	0.07	0.5
Longitudinal damping time (h)	3.6	1.1	2.4	...	...	...
Initial burn-off time (h)	3.0	17 – 3.4	13	...	...	...
Total facility ac power (MW)	200	580	...	200	270	290
Novel technology	16 T magnets	16 T magnets	HTS magnets	μ production/10–16 T magnets		

[a]The 14 TeV c.m.e. muon collider design has not yet been completed; the numbers are a projection (Neuffer and Shiltsev, 2018).

2019) and, due to their compact size, a smaller number of elements requiring high reliability and individual control for effective operation (Shiltsev, 2010b). In addition, a $\mu^+\mu^-$ Higgs factory would have the advantages of a large Higgs production cross section via *s*-channel production, and of a beam energy equal to about half of the standard e^+e^- Higgs production mode at 240–250 GeV c.m.e. (i.e., 2×63 GeV for $\mu^+\mu^- \to H_0$). It would, therefore, offer a small footprint, a low energy spread in nonradiating muon beams $O(3\ \mathrm{MeV})$, and a low total site power of ~200 MW (Ankenbrandt *et al.*, 1999; Alexahin, Gianfelice-Wendt, and Kapin, 2018). Finally, a neutrino factory could potentially be realized during the course of its construction (Geer, 1998, 2009; Boscolo, Delahaye, and Palmer, 2019).

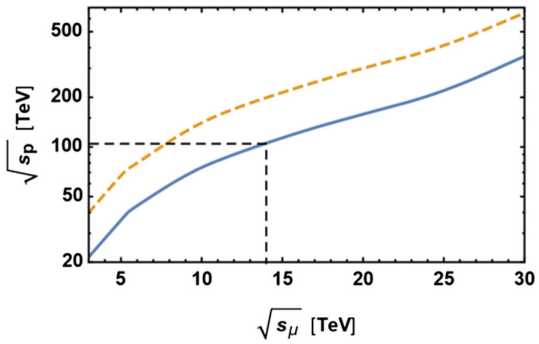

FIG. 33. Energy reach of muon-muon collisions: the energy at which the proton collider cross section equals that of a muon collider. Pair production cross sections for heavy particles with mass M approximately equal to half the muon collider energy $\sqrt{s_\mu}/2$ are compared. The dashed yellow line assumes comparable processes for muon and proton production, while the solid blue line accounts for the possible QCD enhancement of the proton production. From Delahaye *et al.*, 2019.

Muon colliders were proposed by Tikhonin and Budker in the late 1960s (Tikhonin, 1968; Budker, 1970a, 1970b) and conceptually developed later by a number of researchers and collaborations [comprehensive lists of references were given by Geer (2009) and Boscolo, Delahaye, and Palmer (2019)]. Figure 34 presents a possible layout of a multi-TeV c.m.e. high-luminosity $O(10^{34}\ \mathrm{cm}^{-2}\,\mathrm{s}^{-1})$ muon collider consisting of (i) a high power proton driver (srf 8 GeV 2–4 MW H^- linac); (ii) pretarget accumulation and compressor rings in which high-intensity 1–3 ns long proton bunches are formed; (iii) a liquid mercury target for converting the proton beam into a tertiary muon beam with an energy of about 200 MeV; (iv) a multistage ionization cooling section that reduces the transverse and longitudinal emittances and thereby creates a low-emittance beam; (v) a multistage acceleration (initial and main) system, with the latter employing *recirculating linear accelerators* (RLAs) to accelerate muons in a modest number of turns up to 2 TeV using superconducting rf cavities; and, finally, (vi) a roughly 2 km diameter collider ring located some 100 m underground, where counterpropagating muon beams

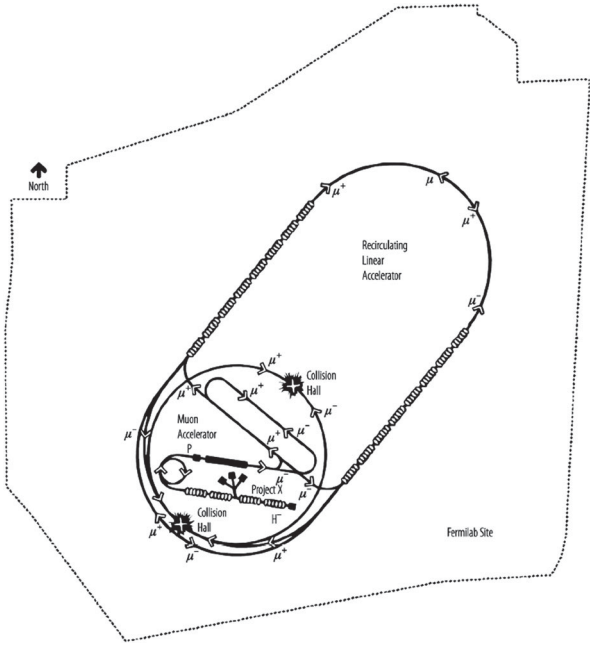

FIG. 34. Schematic of a 4 TeV muon collider on the 6×7 km^2 FNAL site. From Myers and Schopper, 2013.

are stored and collide over the roughly 1000–2000 turns corresponding to the muon lifetime.

Since muons decay quickly, large numbers of them must be produced to operate a muon collider at high luminosity. Collection of muons from the decay of pions produced in proton-nucleus interactions results in a large initial 6D phase-space volume for the muons, which must be reduced (cooled) by a factor of 10^6 for a practical collider. Without such cooling, the luminosity reach will not exceed $O(10^{31}\ \mathrm{cm^{-2}\,s^{-1}})$. The technique of ionization cooling proposed by Ado and Balbekov (1971), Skrinsky and Parkhomchuk (1981), and Neuffer (1983) is fast and uniquely applicable to muons because of their minimal interaction with matter. It involves passing the muon beam through some material absorber in which the particles lose momentum essentially along the direction of motion via ionization energy loss, commonly referred to as dE/dx. Both transverse and longitudinal momenta are reduced via this mechanism, but only longitudinal momentum is then restored by reacceleration, leaving a net loss of transverse momentum (transverse cooling). The process is repeated many times to achieve a large cooling factor.

The rate of change of the normalized transverse emittance $\varepsilon_{x,y} = \varepsilon_\perp$ as the beam passes through an absorber is given by

$$\frac{d\varepsilon_\perp}{dz} \simeq -\frac{\varepsilon_\perp}{\beta^2 E_\mu}\left|\frac{dE_\mu}{dz}\right| + \frac{\beta_\perp (13.6\ \mathrm{MeV}/c)^2}{2\beta^3 E_\mu m_\mu X_0}, \qquad (37)$$

where βc denotes the muon velocity, E_μ indicates the muon energy, $|dE_\mu/dz|$ is the mean energy loss per unit path length, X_0 denotes the radiation length of the absorber, and $\beta_\perp$ is the transverse betatron function at the absorber. The first term of this equation describes the cooling effect by ionization energy loss and the second describes the heating caused by multiple Coulomb scattering. Initially the cooling effect dominates over the heating one, leading to a small equilibrium emittance. The energy spread acquired in such a process due to fluctuation of ionization losses (*Landau straggling*) can be reduced by introducing a transverse variation in the absorber density or thickness (such as a wedge) at a location where there is dispersion $D_{x,y}$ and, thus, a correlation between transverse position and energy. This method results in a corresponding increase of transverse phase space, represents an exchange of longitudinal and transverse emittances, and allows cooling in all dimensions thanks to the fast transverse cooling (Palmer, 2014).

Theoretical studies (Palmer *et al.*, 1996; Sessler, 1998) and numerical simulations (Sayed, Palmer, and Neuffer, 2015) showed that, assuming realistic parameters for cooling hardware, ionization cooling can be expected to reduce the phase-space volume occupied by the initial muon beam by a factor of 10^5 to 10^6. A complete cooling channel would consist of 20 to 30 cooling stages, each yielding about a factor of 2 in 6D phase-space reduction; see Fig. 35.

The ionization cooling method, though relatively straightforward in principle, faces some practical implementation challenges. These include rf breakdown suppression and attainment of high accelerating gradients in relatively low frequency NC rf cavities immersed in strong magnetic fields. The International Muon Ionization Cooling Experiment (MICE) (Sandström, 2008; Adams *et al.*, 2019) at RAL (United Kingdom) has recently demonstrated an effective $O(10\%)$ reduction of transverse emittance of initially dispersed 140 MeV/c muons passing through an ionization cooling-channel cell consisting of a sequence of LiH or liquid hydrogen absorbers within a lattice of up to 3.5 T solenoids that provide the required particle focusing (Mohayai, 2018; Bogomilov *et al.*, 2020).

Constructing and operating a muon collider with usable luminosity requires one to surmount significant technical challenges associated with the production, capture, cooling, acceleration, and storage of muons in large quantities and with appropriate phase-space densities. Palmer (2014) and Boscolo, Delahaye, and Palmer (2019) provided comprehensive overviews of the significant progress achieved in

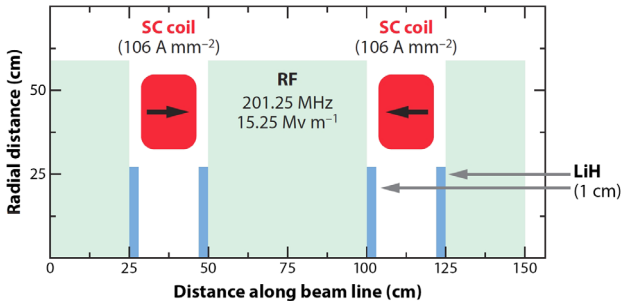

FIG. 35. Ionization cooling-channel section. 200 MeV muons lose energy in lithium hydrate (LiH) absorbers (blue) that is replaced when the muons are reaccelerated in the longitudinal direction in rf cavities (green). The few-tesla SC solenoids (red) confine the beam within the channel and radially focus the beam on the absorbers. Some representative component parameters are also shown. From Geer, 2009.

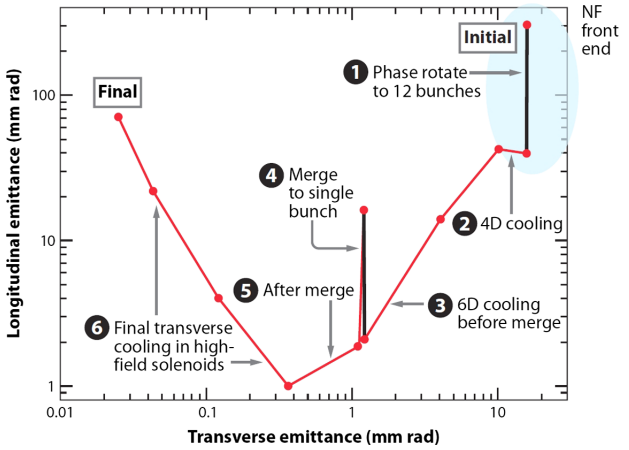

FIG. 36. Simulated six-dimensional (6D) cooling path (Palmer, 2014) corresponding to one particular candidate muon collider cooling channel. The first part of the scheme (blue ellipse) is identical to the present baseline neutrino factory front end. From Geer, 2009.

developing the concepts and technologies needed for high-luminosity energy-frontier muon colliders. In addition to the pioneering demonstration of ionization cooling by MICE, muon collider R&D has led to a number of noteworthy advances in the past decade. The Mercury Intense Target Experiment (McDonald *et al.*, 2009) successfully injected a high-intensity proton beam from the CERN proton synchrotron into a liquid mercury jet inside a 15 T solenoid, proving the feasibility of beam power in excess of 4 MW on such targets. Accelerating gradients of 50 MV/m were obtained in vacuum and pressurized gas-filled NC rf immersed in a 3 T magnetic field at Fermilab (Chung *et al.*, 2013; Bowring *et al.*, 2020). Also at Fermilab, rapid-cycling HTS magnets achieved a record field ramping rate of 12 T/s (Piekarz *et al.*, 2019). The first rf acceleration of muons was demonstrated at the JPARC MUSE RFQ (Bae *et al.*, 2018). Some 16–20 T small bore HTS solenoids were built at BNL, an important step toward the 30–40 T magnets needed for the final muon cooling stage (Gupta *et al.*, 2014). The U.S. Muon Accelerator Program collaboration and its international partners successfully carried out complete 6D muon ionization cooling simulations (see Fig. 36), as well as overall facility feasibility studies, demonstrating that muon colliders can be built with present-day SC magnet and rf technologies, and developed initial designs for 1.5, 3, 6, and 14 TeV colliders; see Table VII.

Under active study are concepts for muon collider detectors that must operate in the presence of various backgrounds originating from muon decay and effective measures to control neutrino radiation (Bartosik *et al.*, 2019). Any straight section within the collider ring produces a beam of muon-decay neutrinos in the direction of the straight section. These neutrinos exit Earth at some point, perhaps a few tens of kilometers away if the ring is deep. At the exit point, neutrino interactions within the rock create radiation at the surface. The radiation level increases rapidly with the stored muon energy. In addition to the straightforward approach of placing the collider-ring tunnel at sufficient depth, there are several mitigation ideas on how to keep neutrino radiation below the commonly accepted limit of 1 mSv/yr. For example, the radiation density can be reduced by about an order of magnitude by adding a vertical collider orbit variation of a few millimeters.

Further improvement could potentially be obtained by using the recently proposed positron-driven muon production scheme. It calls for using 45 GeV positrons to generate muon pairs through e^+e^- annihilation just above threshold (Antonelli *et al.*, 2016), allowing low-emittance beams to be obtained directly, without any cooling. This scheme may allow operation of a high-energy muon collider with manageable neutrino radiation on and off the site. Major directions of the R&D to evaluate the possible luminosity reach of this concept and to address key issues of corresponding technologies were outlined by Boscolo, Delahaye, and Palmer (2019).

Another novel approach, called the *Gamma Factory* (GF) (Krasny, 2015; Krasny *et al.*, 2018), could potentially help make a muon collider become reality. The GF would generate frequent bursts of gamma rays by causing repeated collisions for a partially stripped heavy-ion beam circulating in the LHC, or in a future higher-energy hadron storage ring like the FCC-*hh*, with a conventional laser pulse, profiting from two Lorentz boosts. Impinging on a suitable target, the GF's intense gamma bursts could produce positrons or muons at an unprecedented rate. Thereby the GF could deliver positrons at the rate required for the aforementioned positron-based muon production or, alternatively, it could directly provide a low-emittance muon beam (Zimmermann, 2018). In 2018, the first beam tests confirmed the predicted long beam lifetime of more than a day for a partially stripped heavy-ion beam stored in the LHC at top energy (Schaumann *et al.*, 2019). The next series of proof-of-principle GF experiments, consisting of laser-beam collisions in the SPS, is planned for 2021.

V. ADVANCED COLLIDER CONCEPTS

A. Acceleration in plasma and plasma-based collider proposals

Since about the mid 1950s, it has been understood that collective plasma-based accelerators offer the promise of extremely large accelerating gradients (Veksler, 1957). Ionized plasmas can sustain electron plasma density waves with electric fields in excess of $E_0 = cm_e\omega_p/e$ or

$$E_0 \approx 96\ [\mathrm{V/m}]\sqrt{n_0\ [\mathrm{cm^{-3}}]}, \tag{38}$$

[the so-called cold nonrelativistic wave-breaking field (Dawson, 1959)], where n_0 denotes the ambient electron number density, $\omega_p = \sqrt{e^2 n_0/m_e\varepsilon_0}$ is the electron plasma frequency, m_e and e are the electron rest mass and charge, respectively, c is the speed of light in vacuum, and ε_0 is the electrical permittivity of free space. For example, a plasma density of about 10^{18} cm^{-3} yields $E_0 \sim 100$ GV/m, which is approximately 3 orders of magnitude greater than the ~100 MV/m value obtained in conventional breakdown limited rf structures.

Such gradients can be effectively excited by either powerful external pulses of laser light or electron bunches if they are

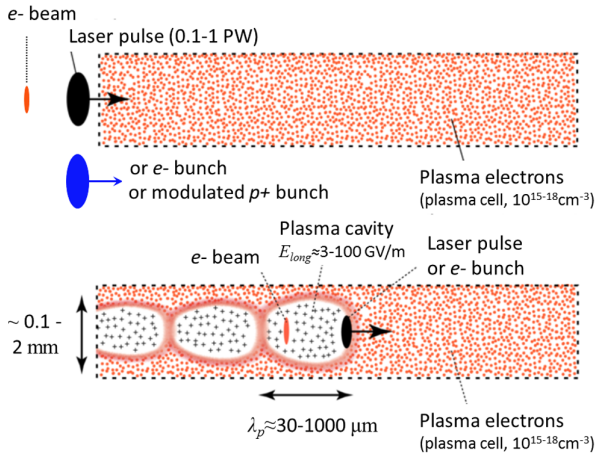

FIG. 37. Concept of the plasma wakefield acceleration driven by a short laser pulse, a short electron bunch, or long(er) modulated proton bunch. Adapted from Assmann and Grebenyuk, 2014.

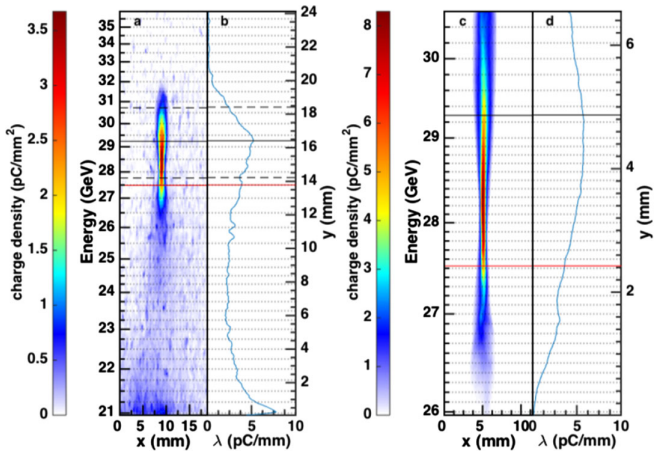

FIG. 38. A 0.1 nC electron bunch gained a maximum energy of 9 GeV in a 1.3-m-long electron plasma wakefield accelerator driven by a 20.35 GeV e^- beam at the FACET facility at SLAC. (a)–(d) Energetically dispersed transverse charge density profile spectra and the horizontally integrated spectral charge density profiles as observed on the wide field of view Cherenkov screen and on the order-of-magnitude more sensitive Lanex screen, respectively. From Litos *et al.*, 2016.

shorter than the plasma wavelength $\lambda_p = c/\omega_p \approx 1\ \text{mm} \times \sqrt{10^{15}\ \text{cm}^{-3}/n_0}$, or by longer beams of charged particles if their charge density is modulated with the period of λ_p. Figure 37 illustrates the concept of plasma acceleration. The plasma response to a short laser pulse is as follows (Tajima and Dawson, 1979): (i) the laser pulse enters the plasma and transversely accelerates plasma electrons (ponderomotive force as transverse driving force), (ii) the plasma ions move a negligible amount and a positively charged ion channel is formed along the laser path, (iii) after the passage of the laser pulse, the plasma electrons rush back in, attracted by the transverse restoring force of the positively charged ion channel, pass the center of the ion channel, rush back out and are attracted back by the ion channel, and (iv) a space-charge-driven oscillation is formed, leaving alternating regions of negative and positive net charge with strong induced longitudinal fields behind the laser pulse (*plasma wakefields*). If a short test bunch of charged particles, e.g., electrons, is placed behind the laser pulse at a proper distance, then it will be accelerated with high gradient. The process could be limited by a depletion of laser pulse power, dephasing between the relativistic test bunch and the wake-field, and the Rayleigh length of the laser beam (unless counteracted by self-guiding or external guiding of the laser in a plasma channel). Similar concepts have been proposed for plasma wakefields driven by short electron bunches (Chen *et al.*, 1985) and by self-modulated high-energy proton bunches with an rms bunch length of the order of 10 cm (Caldwell *et al.*, 2009).

The three plasma driver technologies have been explored theoretically and experimentally, and corresponding reviews and references were given by Esarey, Schroeder, and Leemans (2009), Adli and Muggli (2016), and Hogan (2016). In the past decade, we have seen substantial progress of the plasma wakefield acceleration of high-quality beams. A laser-driven electron energy gain of about 8 GeV over 20 cm of plasma with density $3 \times 10^{17}\ \text{cm}^{-3}$ was demonstrated at the BELLA facility at the Lawrence Berkeley National Laboratory (Gonsalves *et al.*, 2019). Short electron bunches were used to boost the energy of externally injected electron bunches by 9 GeV over 1.3 m of $\sim 10^{17}\text{cm}^{-3}$ plasma at the FACET facility in SLAC (Litos *et al.*, 2016); see Fig. 38. The AWAKE experiment at CERN used self-modulating long 450 GeV proton bunches to accelerate electrons to 2 GeV over 10 m of $10^{15}\ \text{cm}^{-3}$ plasma (Adli *et al.*, 2018).

In principle, the plasma wakefield acceleration scheme has the potential to be staged; e.g., several plasma cells of the same kind can be placed in series, resulting in higher beam energy (Steinke *et al.*, 2016). That makes possible attainment of high energies and designs of TeV or multi-TeV e^+e^- colliders, such as those proposed by Leemans and Esarey (2009), Schroeder *et al.* (2010), and Adli *et al.* (2013). The primary advantage that a plasma wakefield accelerator could present is a considerably greater compactness, and hence a much lower "real-estate" investment for the collider. Collisions of intrinsically short bunches (a fraction of the plasma wavelength) are also advantageous for the reduction of beamstrahlung effects (Himel and Siegrist, 1985; Schroeder, Esarey, and Leemans, 2012).

There are a number of critical issues that need to be resolved along that path (Assmann and Grebenyuk, 2014; Lebedev, Burov, and Nagaitsev, 2016; Schulte, 2016), including acceleration of positrons (which are defocused by the positively charged ion cavity when accelerated in a plasma; see Fig. 37), instabilities in accelerated beams and beam emittance control in scattering media, final focusing of e^+ and e^- bunches with significant energy spread acquired during acceleration, and efficiency of staging [beam transfer and matching from one $O(1\ \text{m})$-long plasma cell to another]. Indeed, strong transverse focusing gradients $O(10\ \text{MT/m})$ are generated inside the ion channel of plasma accelerators. Such focusing is equivalent to small beta functions $\beta_{x,y}$ in the range of a couple of centimeters to a few millimeters for high-energy beams accelerated in the $n_0 = 10^{14-17}\ \text{cm}^{-3}$ plasma.

Matching electrons and positrons in and out of these multiple plasma cells is difficult, comparable to low-β insertions of traditional colliders, and transverse injection error tolerances $O(1\ \mu\text{m})$ become highly demanding.

A comparative analysis of initial straw man designs of high-luminosity 3 to 10 or 30 TeV laser-driven and beam-driven e^+e^- colliders (Adli *et al.*, 2013; Cros and Muggli, 2019) with that of CLIC does not show any significant advantage in ac-to-beam-power efficiency of the advanced schemes; ac wall-plug power needs are ~0.5 GW for 10 TeV c.m.e. and over 1 GW for 30 TeV c.m.e. machines. The total facility length would still be considerable [6–8 km for $\sqrt{s} = 3$ TeV and 10–18 km for 10 TeV, subject to further optimization (U.S. Department of Energy, Office of Science, 2016)] and the beamstrahlung effect would ultimately be severe: the expected rms energy spread at the IP is about 30% for 10 TeV machines and 80% for 30 TeV colliders.

Caldwell and Wing (2016) proposed a LHC upgrade for a high-energy 9 TeV c.m.e. electron-proton collider using a 3 TeV electron beam accelerated by the proton-driven plasma wakefields. In this scenario, one of the two 7 TeV LHC proton beams is used as the proton driver to create plasma wakefields accelerating electrons to 3 TeV, which then collide with the other 7 TeV LHC proton beam. Assuming 3000 LHC bunches per fill with a 30 min machine cycle time, 10^{11} electrons and 4×10^{11} protons per bunch (about twice the value foreseen for the LHC luminosity upgrade), and a transverse rms beam size of 4 μm, a relatively low luminosity of 4×10^{28} $\text{cm}^{-2}\,\text{s}^{-1}$ can be reached.

Plasma wakefield acceleration concepts have not yet achieved the level of a reliable conceptual design for an affordable high-luminosity multi-TeV e^+e^- collider. The ILC and CLIC studies have emphasized that the performance reach of a linear collider is essentially proportional to the beam power [see Eq. (33)], and at present the plasma wakefield acceleration technology is far from the wall-plug efficiency of NC and srf linacs. This reflects the current state of the plasma driver technologies, while Esarey, Schroeder, and Leemans (2009), Litos *et al.* (2014), and Schroeder *et al.* (2016) indicated that sufficiently high plasma to beam efficiency can be attained.

Correspondingly, the focus of the current R&D activities carried out by several groups and collaborations (Cros and Muggli, 2019), including EuPRAXIA (European Plasma Research Accelerator with Excellence in Applications) (Walker *et al.*, 2017) and the Advanced Linear Collider Study Group (Muggli and Cros, 2018), is less on breaking the accelerating gradient records and more on mundane but critical issues such as energy transfer efficiency, production of high-quality high repetition rate beams with the various driver technologies, positron acceleration, staging, and exploration of the possibilities offered by recent advances in high peak power laser technologies (Mourou *et al.*, 2013; Dawson and Polyanskiy, 2018; Tajima, Yan, and Ebisuzaki, 2020) [similar to how *chirp pulse amplification* (Mourou, 2019), which resulted in the 2018 Nobel Prize in Physics, boosted the laser plasma acceleration technique]. A number of beam test facilities addressing these major scientific challenges are operating, coming on line, or in the planning phase. In the United States, road maps of advanced accelerator R&D have been developed with the primary long-term goal of a TDR of a multi-TeV collider in the 2035–2040 time period and a secondary, nearer-term goal of the completion of a TDR for potential early application of these acceleration techniques in the 2025–2030 time period (Colby and Len, 2016).

B. Other advanced approaches for colliding-beam schemes

In addition to the previously presented designs and concepts, many ideas and approaches have been proposed to extend the energy reach of future particle colliders, reduce their cost, and improve their luminosity and energy efficiency. We now present some that have shown promise and have been considered in at least some detail for applications in future nuclear physics or particle-physics colliders.

Economical magnets for large hadron colliders.—The potential benefits of using modest or relatively low-field magnets to reach ultrahigh proton beam energies in extremely large circular colliders were first discussed by Fermi, who in the mid 1950s thought of an Earth-encircling "Globaltron" with a circumference of $C = 40\,000$ km and energy reach of 5000 TeV (5 PeV) (Cronin, 2004). Attempts to figure out a cost-feasible variation of such a concept include the "Collider in the Sea" ($C = 1900$ km, underwater in the Gulf of Mexico, $\sqrt{s} = 500$ TeV with economical 3.2 T SC magnets) (McIntyre *et al.*, 2016), the 300 km circumference 300 TeV "Eloisatron" with 10 T magnets (Zichichi, 1990; Barletta, 1996), and the 233-km-long VLHC (Ambrosio *et al.*, 2001). In the VLHC design, the Stage 1 machine was to accelerate 20 TeV proton beams in a 2 T double-aperture superferric SC magnet synchrotron ring and have them collide at $\sqrt{s} = 40$ TeV. Afterward the Stage 1 complex would act as an injector accelerator to a 200 TeV c.m.e. collider in the same tunnel based on 12 T Nb_3Sn magnets. A 1.5-m-long single turn 100 kA SC transmission line twin-aperture combined function dipole-magnet prototype for VLHC Stage 1 was built at Fermilab and demonstrated good field quality at the design 2 T field (Piekarz *et al.*, 2006). Opportunities to reduce the cost of the 100 km FCC-*hh* collider by using 6–8 T economical Nb-Ti SC magnets (resulting in $\sqrt{s} = 37.5$–50 TeV) are also being discussed. As mentioned previously, in China prospects of having inexpensive 12–24 T iron-based HTS superconductors have initiated machine design studies of the SppC in the 100 km CEPC tunnel (Tang, 2017; Benedikt and Zimmermann, 2018).

ERLs.—Another promising and actively developing technology is that of RLAs and ERLs. RLAs are accelerators in which the accelerating structure of an rf linac is used a few to dozens of times to accelerate the same beam. Return beam lines that are needed to take the beam out of the linac and to reinject it back at proper phase tend to be much cheaper to build than additional rf linac length, thus offering a cost-effective option to achieve the highest possible energy from a given rf installation. Such a hybrid arrangement of linac and ring also allows superior electron-beam quality compared to a storage ring. Indeed, the beam dwells a short time in the accelerator and avoids many storage-ring processes leading to emittance growth (due to synchrotron radiation) or depolarization. With proper care for beam dynamics, electron-beam brightness is then determined by the electron source and

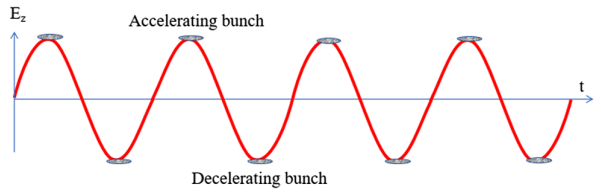

FIG. 39. Basic ERL principle. Accelerating bunches take energy from a srf linac, while decelerating bunches return energy.

can thus be high; see Merminga, Douglas, and Krafft (2003), Ben-Zvi (2016), and Myers and Brüning (2016), Chap. 39. In instances where high average current is required, such as for high-luminosity colliders, the RLA concept can be augmented with a reverse process of energy recovery: the energy invested in accelerating a beam is returned to the device powering the acceleration by decelerating the beam after it has been put to some use. The basic principle of the energy recovery process is illustrated in Fig. 39.

The original idea of a srf ERL is attributed to Tigner (1965), but only in the past two decades has the srf technology matured enough to render the full potential of ERLs accessible (Liepe and Knobloch, 2006). Superconducting rf cavities allow efficient operation in either a cw or a long pulse regime due to high quality factor $O(10^{10})$. Thanks to lower frequency and high gradients, which can potentially exceed 50 MV/m (Grassellino *et al.*, 2018), they offer larger stored energy and lower beam impedances than in commonly used NC rf structures and lower beam impedances, therefore reducing the risk of detrimental instabilities at high beam current. Envisioned srf ERL applications include accelerators for the production of synchrotron radiation and free electron lasers (Gruner *et al.*, 2002), high-energy electron cooling devices, and e-p and e-ion colliders (Ben-Zvi, 2016).

ERL applications for the JLEIC electron cooling system and in the LHeC and FCC-eh electron-proton colliders are presented in Sec. IV. An alternative option of an ERL-based eRHIC design was studied in sufficient detail and summarized in the CDR document (Aschenauer *et al.*, 2014). The 10 mA polarized e^- ERL in the RHIC tunnel needs 12 passes through a 1.32 GeV srf linac to produce 15.9 GeV polarized electrons that then collide with 250 GeV protons with high e-p luminosity of the order of 10^{33-34} cm^{-2} s^{-1}. The major challenges of such an approach include (a) the need to suppress excitation of HOMs by the beam passing the ERL's srf cavities to avoid current-limiting beam breakup instability, (b) generation of high average current of a polarized electron beam out of a rf gun, (c) halo and beam loss control in the ERL to avoid undue heating and potential damage, (d) collective effects due to *coherent synchrotron radiation* and space-charge effects, (e) precise magnetic field quality control in numerous return beam lines of the ERL, and (f) an eRHIC design specific coherent electron cooling scheme for hadron beams (Litvinenko and Derbenev, 2009). In 2019, a demonstrator facility, the CBETA, has accelerated electrons from the initial 6 MeV to 42, 78, 114, and 150 MeV in four passes through the srf cavities and subsequently decelerated them during four additional passes through the same cavities back to their original 6 MeV energy (Brookhaven National Laboratory, 2020). CBETA was also the first accelerator to use a single beam line with fixed magnetic fields to transport seven different accelerating and decelerating energy beams (Michnoff *et al.*, 2019).

ERL-based Higgs factories and $\gamma\gamma$ colliders.—A similar concept was also proposed as an option for the FCC-ee ring collider in a 100 km tunnel in which two 33.7 GeV linacs would accelerate e^+ and e^- beams in four passes to $\sqrt{s} =$ 250 GeV needed for Higgs boson physics research (Litvinenko, Roser, and Chamizo-Llatas, 2020). Flat electron and positron beams with emittances 2 orders of magnitude smaller than those in the ring-ring FCC-ee design (see Sec. IV.B and Table V) would be generated in 2 GeV cooling rings with top-up injection, then extracted out of the rings with the frequency required by the collider and accelerated to collision energy in a four- to six-pass ERL bypassing the interaction regions. Each path requires an individual 100 km arc made of either permanent magnets or low-cost, low power consumption 0.04 T electromagnets. As the top energy beams collide at the IPs, their phases are changed to deceleration and they return up to 81% of the energy back into the srf cavities. Some 14 GeV of beam energy will be lost to synchrotron radiation in the arcs, but given that the total required beam current is small, total SR power losses will be an order of magnitude lower than in the FCC-ee design, i.e., only ~10 MW for a design luminosity of a few 10^{34} cm^{-2} s^{-1}. Low average current would render the ERL relatively free of HOMs and coherent instability concerns, but preservation of the ultrasmall beam emittances over hundreds of kilometers of beam lines might be as challenging as for linear e^+e^- colliders.

The idea of a photon-photon collider through near-IP conversion of high-energy electron beams into intense γ beams by backward Compton scattering of a high power laser was put forward in the early 1980s (Ginzburg *et al.*, 1983). The spectrum of the resulting γ's will be close to the incident electron energy, so with a proper laser system such a scheme (see Fig. 40) can obtain $\gamma\gamma$ and γe collisions with energy and luminosity comparable to electron-position luminosity, will be free of the beamstrahlung effect, and would not

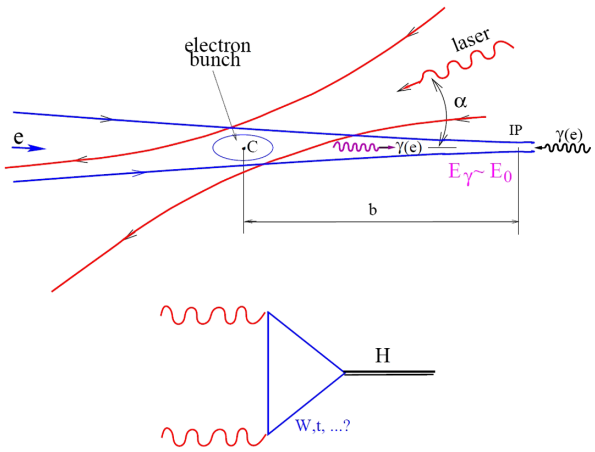

FIG. 40. Top panel: scheme of $\gamma\gamma$, γe collider. Bottom panel: Higgs production diagram of $\gamma\gamma$ collisions. From Telnov, 2014.

need a positron beam production complex (Telnov, 1995). An additional advantage for Higgs physics studies is that the energy of photons has to be only half of the m_H for the direct production reaction $\gamma\gamma \to H$, i.e., about 62.5 GeV, requiring lower initial electron-beam energy of only ~80 GeV vs $E_e =$ 125 GeV in the e^+e^- collider Higgs factory designs. Besides elimination of the positron production system and reduced electron energy, ERL-based concepts for facilities that could reach the Higgs mass in $\gamma\gamma$ collisions offer additional opportunities to minimize accelerator costs by using a flat beam electron gun instead of electron damping rings and minimizing the total required accelerating voltage of rf sections (Bogacz *et al.*, 2012; Gronberg, 2014). To lower beam energy losses due to synchrotron radiation in the ERL arcs, such Higgs factories should be placed in longer circumference tunnels. Two examples are the HFiTT proposal to employ a total of 10 GeV of srf accelerators in the existing 6.3 km circumference Tevatron tunnel at Fermilab (Chou *et al.*, 2013) and the SAPPHiRE proposal with 22 GeV of srf linacs in the 9-km-long LHeC racetrack tunnel (Bogacz *et al.*, 2012). Of concern for such machines is the problem of emittance dilution due to synchrotron radiation and other effects in their long arcs (Telnov, 2014). The pulse structure of the ERL-based $\gamma\gamma$ Higgs factories with a short distance between collisions is well suited to fiber lasers, and breakthroughs in coherent amplification of short pulses in such lasers (Mourou *et al.*, 2013) may eventually spark serious interest in the $\gamma\gamma$ colliders (Takahashi, 2019).

"Cold" normal-conducting rf.—The concept of a TeV-class linear e^+e^- collider based on NC copper accelerating cavities operating at liquid nitrogen temperature offers the promise of significantly lower linac cost and power per GeV than in the ILC (srf cavities at 2 K) and CLIC (room temperature rf structures) (Bane *et al.*, 2018). The linac design is based on two features: a 5.7 GHz accelerator structure with a separate feed to each cavity permitting the iris to be optimized for a high gradient (117 MV/m) and lower breakdown rate, and linac rf operation at 77 K, causing Cu or Cu alloy conductivity to increase and reducing rf power requirements by about a factor of 2.5. Preliminary design studies indicate some 342 MW of total ac power would be needed for a 2 TeV c.m.e. collider with luminosity 5×10^{34} cm^{-2} s^{-1}.

Dielectric wakefield accelerators (DWFA).—Substantial research efforts have been carried out to extend the two-beam acceleration scheme (similar to that of CLIC) through feeding resonant dielectric accelerating structures are fed by ultrashort rf pulses of wakefields driven by either collinear or preceding high charge electron bunches (Gai *et al.*, 1988; Gai, 2009; Jing, 2016). In the latter case, electromagnetic power is radiated by an ultrashort, intense "driving" electron bunch propagating in a high-impedance environment and then used to accelerate another "witness" bunch. Better breakdown properties of some dielectric materials (quartz, ceramics, diamond) and improvement of the BDR with shorter rf pulse length $\tau_{\rm rf}$ [see Eq. (34)] allow gradients in excess of 1 GV/m for picosecond exposure times, as demonstrated with simple $O(0.1\ \text{mm})$ diameter hollow dielectric tubes driven by short, narrow, and intense 28.5 GeV SLAC linac bunches (Thompson *et al.*, 2008). For collider applications, much longer pulses are needed to drive many bunches and attain high average currents. For example, in the 3 TeV c.m.e. e^+e^- Argonne Flexible Linear Collider proposal (Gai, Power, and Jing, 2012), some 20-ns-long 26 GHz rf pulses (12 times shorter than in CLIC) are generated by 32 50 nC drive-beam bunches out of 0.86 GeV 1.3 GHz rf linacs passing through decelerating structures. This scenario should allow 270 MV/m operational accelerating gradients for the main beams. The beam accelerating gradient achieved in 26 GHz alumina structures is currently about 30 MV/m (1.8 MeV acceleration over 6.5 cm) and some 70 MV/m in 11.7 GHz structures (4.9 MeV over 7 cm) (Shao *et al.*, 2018). Application of this concept to colliding beams faces many challenges, such as fabrication of efficient dielectric high-gradient rf structures, drive-beam production with bunch charge an order of magnitude greater than typically achieved in the most common efficient rf guns, and wakefield damping to assure main beam stability and attainment of overall ac power to beam efficiency comparable or exceeding that of CLIC (Jing, 2016; Schulte, 2016). Design, construction, and testing of a smaller module for free electron laser applications (Zholents *et al.*, 2016) may help to greatly advance DWFA technology.

Dielectric laser accelerators (DLAs).—Micron-size dielectric accelerating structures can be driven not by conventional rf but rather by a laser (Peralta *et al.*, 2013), and they can support accelerating fields an order of magnitude higher than can rf cavity-based accelerators. For example, some 35 keV electron energy gain over only 50 μm (700 MV/m gradient) was achieved in a fused silica DLA structure with an 800 nm grating period driven by a 90 fs, 800 nm Ti:sapphire laser pulse (Wootton *et al.*, 2016). Despite relatively modest accelerating gradients relative to plasmas, the prospects of using commercial lasers, which are smaller and less expensive than the rf klystrons powering present-day accelerators, as a power source and low-cost fabrication lithographic techniques for mass production of optical structures, like the one depicted in Fig. 41, have generated interest in DLA-based linear

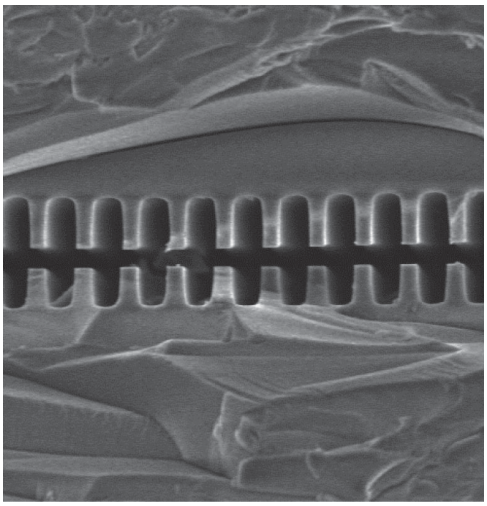

FIG. 41. Scanning electron microscope image of the longitudinal cross section of a dielectric laser acceleration structure with a 400 nm gap (Peralta *et al.*, 2013).

electron-positron colliders (England *et al.*, 2014). Straw man parameter tables for 3 TeV and 30 TeV DLA machines presented by Cros and Muggli (2019) indicate that a path exists to high luminosities of $10^{34–36}$ cm^{-2} s^{-1} via a combination of high repetition rate ($f_r = 20$ MHz) operation of 2 μm wavelength fiber lasers, a small bunch population of some 30 000 electrons and positrons per bunch, and small emittances, nanometer bunch length and spot sizes at the IP, etc. In such a scheme, beamstrahlung-induced energy spread is minimal, while the luminosity enhancement factor H_D of about 10 is due to the pinching effect from the beam-beam interaction at the IP. The required ac wall-plug power is 360 MW for 3 TeV and 30 GW for 30 TeV machines, and it scales with luminosity. In addition to critical issues of production of ultrasmall emittance beams, which will be particularly challenging for positrons, and preservation of these small emittances over many kilometers of optical linacs, the overall power efficiency of the DLA-based collider scheme will require extensive research and development on laser power generation and distribution to achieve a level comparable to or better than that of CLIC or ILC.

Linear muon crystal colliders.—Wakefield acceleration of muons (instead of electrons or hadrons) channeling between the planes in crystals (Tajima and Cavenego, 1987) or inside carbon nanotubes (CNTs) (Shin, Still, and Shiltsev, 2013) with charge carrier density $\sim 10^{20–22}$ cm^{-3} holds the promise of the maximum theoretical accelerating gradients of 1–10 TeV/m [see Eq. (38)], allowing envisioning of a compact 1 PeV linear crystal muon collider (Chen and Noble, 1997; Shiltsev, 2012a). The choice of muons is beneficial because of small scattering on solid media electrons, absence of beamstrahlung effects at the IP, and continuous focusing while channeling in crystals, i.e., acceleration to final energy can be done in a single stage. Muon decay becomes practically irrelevant in such fast acceleration gradients as muon lifetime quickly grows with energy as 2.2 $\mu s \times \gamma$. Initial luminosity analysis of such machines assumes a small number of muons per bunch ($\sim 10^3$), a small number of bunches (~ 100), high repetition rate (~ 1 MHz), and ultimately small sizes and overlap of the colliding beams (~ 1 Å). Excitation of plasma wakefields in crystals or nanostructures can be possible by short submicron high density bunches of charged particles or x-ray laser pulses (Zhang *et al.*, 2016; Wheeler, Mourou, and Tajima, 2019), by heavy high-Z ions, or by premodulated or self-modulated high-current bunches (Shiltsev, 2019). The concept of acceleration in the crystal or CNT plasma requires a proof-of-principle demonstration (Shin, Lumpkin, and Thurman-Keup, 2015), extensive theoretical analysis, modeling, and simulations (Shiltsev and Tajima, 2019).

VI. CONCLUSIONS

High-energy particle colliders are unique facilities in many ways. They are the pinnacle of almost a century of developments in accelerator and beam physics. Most advances in physics and in technologies of single beam accelerators for various branches of contemporary science have been utilized in colliders over their half-century-long history. The opposite is true too: many breakthroughs in the development of the collider method are widely used in modern accelerators for industry, medicine, and scientific research in biology, chemistry, and solid-state and nuclear physics. Numerous technological advances from other fields of science and technology (most notably from solid-state physics, lasers, plasma, high-energy physics, computers and information technology, cryogenic devices and rf generation, radiation control, and ultrahigh vacuum, among others) have effectively been applied to construct better and more powerful colliders. The center-of-mass energy of colliding-beam facilities has grown by 5 orders of magnitude and their luminosity by about 7 orders of magnitude. Collisions of high-energy particles offer unique opportunities to answer the most fundamental questions of modern science regarding the composition and evolution of the Universe, and there is a growing aspiration for colliders with order-of-magnitude higher energies and luminosities.

The physics community of the seven currently operational colliders is wide and includes the majority of the world population of some 33 000 high–energy physicists and a large fraction of 24 000 nuclear physicists (Battiston *et al.*, 2019). Several colliding-beam facilities are either under construction or entering the construction project phase (NICA in Russia, Electron Ion Collider in the United States, etc.). It is easy to see that these mostly aim at serving nuclear physics research needs. One of the main nonscientific reasons for such projects to proceed is their relatively modest energy reach (several to hundreds of GeV of the center-of-mass energy $\sqrt{s}$) and, as a result, affordable cost in the sub-billion dollar to $1 billion to $2 billion range.

The situation differs for the next generation of HEP colliders. At present, aspirations of the HEP community are focused on two opportunities offering interesting physics prospects, namely, future Higgs or electroweak factories, and energy-frontier (EF) colliders. There are four feasible, widely discussed concepts: linear e^+e^- colliders, circular e^+e^- colliders, pp/ep colliders, and muon colliders. These all have limitations in energy, luminosity, efficiency, and cost. The most critical requirement for a Higgs factory is high luminosity, and four proposals generally satisfy it: the ILC at 250 GeV c.m.e., CLIC at 380 GeV, CEPC, and FCC-ee. The next level criteria include facility cost, required ac wall-plug power, and technical readiness. The construction cost, if calibrated to performance (i.e., in units of CHF per ab^{-1} of the integrated luminosity) is the lowest for the FCC-ee, followed by the CEPC (by a factor of 4), then the ILC (another factor of 10), then CLIC (another factor of 2); see Table VIII. The expected ac site power consumption if calibrated to performance (i.e., in units of ab^{-1}/TW h) also is the lowest for the FCC-ee, followed by the CEPC (factor of 2), then the ILC (another factor of 2), and then CLIC (another factor of 2). As for readiness to start construction, the ILC is somewhat ahead of other proposals (it has TDR versus CDRs for CLIC, CEPC, and FCC-ee) and is technologically quite mature, with well understood plans for industrial participation. On the other hand, the FCC-ee and CEPC proposals are based on concepts and beam dynamics parameters that have already been proven at many past and presently operating circular colliders.

The most critical requirement for the EF colliders is the center-of-mass energy reach. There are four proposals that

TABLE VIII. Main parameters of proposed colliders for high-energy particle-physics research: center-of-mass energy, number of detectors in simultaneous operation N_{det}, total integrated luminosity in these detectors, expected collider operation time, average ac wall-plug power, cost estimate, the cost per ab^{-1} of integrated luminosity and integrated luminosity per TW h of electricity consumption. Most of the parameters are taken from the input documents submitted to the European Particle Physics Strategy Update (Ellis *et al.*, 2019, Appendix C) and from a report prepared for the CERN Scientific Policy Committee (Bordry *et al.*, 2018). Cost estimates are given with some 20%–30% accuracy. Note that the cost accounting is not uniform across the projects, as well as the currency. For example, the ILC cost is given in "ILC units.": 1 ILCU was defined as 1 U.S. dollar (USD) in January, 2012.

	Type	Energy	N_{det}	$\mathcal{L}_{int}$	Time	Power	Cost	Cost/$\mathcal{L}_{int}$	$\mathcal{L}_{int}$/power
Project		(TeV, c.m.e.)		(ab^{-1})	(yr)	(MW)		(billion CHF/ab^{-1})	(ab^{-1}/TW h)
ILC	e^+e^-	0.25	1	2	11	129	4.8–5.3 billion ILCU	2.7	0.24
		0.5	1	4	10	163(204)	8.0 billion ILCU	1.3	0.4
		1	1			300			
CLIC	e^+e^-	0.38	1	1	8	168	5.9 billion CHF	5.9	0.12
		1.5	1	2.5	7	370	+5.1 billion CHF	3.1	0.16
		3	1	5	8	590	+7.3 billion CHF	2.0	0.18
CEPC	e^+e^-	0.091 and 0.16	2	$16+2.6$	$2+1$	149	5 billion USD	0.27	7.0
		0.24	2	5.6	7	266		0.21	0.5
FCC-*ee*	e^+e^-	0.091 and 0.16	2	$150+10$	$4+1$	259	10.5 billion CHF	0.065	20.5
		0.24	2	5	3	282		0.064	0.9
		0.365 and 0.35	2	$1.5+0.2$	$4+1$	340	+1.1 billion CHF	0.07	0.15
LHeC	ep	1.2	1	1	12	(+100)	1.37[a] billion CHF	1.37	0.14
HE-LHC	pp	27	2	20	20	220	7.2 billion CHF	0.36	0.75
FCC-*hh*	pp	100	2	30	25	580	17(+7) billion CHF	0.8	0.35
FCC-*eh*	ep	3.5	1	2	25	(+100)	1.75 billion CHF	0.9	0.13
Muon collider	$\mu\mu$	14	2	50	15	290	10.7[a] billion CHF	0.21	1.9

[a]Estimates for LHeC and muon collider are extrapolated from the costs of other projects; see Bruning (2018) and Agostini *et al.* (2020), and Neuffer and Shiltsev (2018), respectively.

generally satisfy it (in order of energy reach): 3 TeV CLIC, HE-LHC, 6–14 TeV muon collider, and FCC-*hh* or SppC. The next level criteria for EF machines are cost, the facility's ac wall-plug power, machine efficiency, and attainable annual integrated luminosity, the total annual running cost (including manpower), and the level of R&D effort needed to bring the concept to the level of construction readiness (the level of comprehensive TDR). The construction cost is lowest for the HE-LHC and muon collider, followed by the 3 TeV CLIC (factor of 2) and FCC-*hh* (another factor of 1.5). The estimated ac site power requirement is lowest for the HE-LHC and the muon collider, followed by CLIC (factor of 2), then by FCC-*hh* (another factor of 1.5). As for required duration and scale of R&D efforts to reach the TDR level of readiness, the 3 TeV CLIC project is ahead of other proposals as it requires ~10 yr of R&D versus about twice that for the HE-LHC, FCC-*hh* or SppC, and muon collider (the last at present being the only concept without a comprehensive CDR, but with a plan to initiate an international design study to address key challenges such as the production of intense beams of cooled muons).

Another important factor for any large-scale facility is operating cost. Design efforts need to be made, starting from the early concept stage, to enable a sustainable operational efficiency. The history of large-scale collider infrastructures such as at Fermilab and CERN reveals a trend of steadily decreasing normalized operating costs and number of personnel. For example, at the peak of LEP operation CERN had 3300 staff members, while in the era of LHC, which together with its injectors is a much more complex machine, the laboratory staff has shrunk to 2300 employees. Such a manifestation of progress in technology, operation, and maintenance concepts will need to continue for the energy-frontier machines. Their designs should place an emphasis on conceiving the individual systems and subsystems such that they can be monitored, maintained, and repaired by service suppliers as much as reasonably possible, on investing early on in a modular architecture of basic components and equipment to enable streamlined operation, service, and repair, and on in-kind, collaborative operation.

Arguably the biggest technical challenge for EF hadron and muon colliders is the development of bending magnets with a maximum field up to 16 T. There are fundamental challenges in getting the required current density in SC cables and in dealing with the ultimate magnetic pressures and mechanical stresses in the superconductor and associated components. Some experts estimate that at least 15–20 years might be needed for new approaches to mature and for developing the technology required to overcome the aforementioned limits through continuous R&D efforts. Lowering the maximum field requirement to 12–14 T or even to 6–9 T could greatly reduce the time needed for short-model R&D, prototyping, and preseries work with industry. To realize even higher fields (beyond 16 T, if needed) HTS technology will inevitably be required. At present, the most critical constraint for the HTS conductor is its much higher cost, even relative to the Nb_3Sn superconductor.

Impressive advances of exploratory plasma wakefield acceleration R&D over the past decade make it important to find out whether a feasible "distant-future" lepton collider option for particle physics can be based on that technology. We note that laser- or beam-driven plasma wakefield accelerators have a significant potential for non-HEP applications and have drawn significant interest and support from the

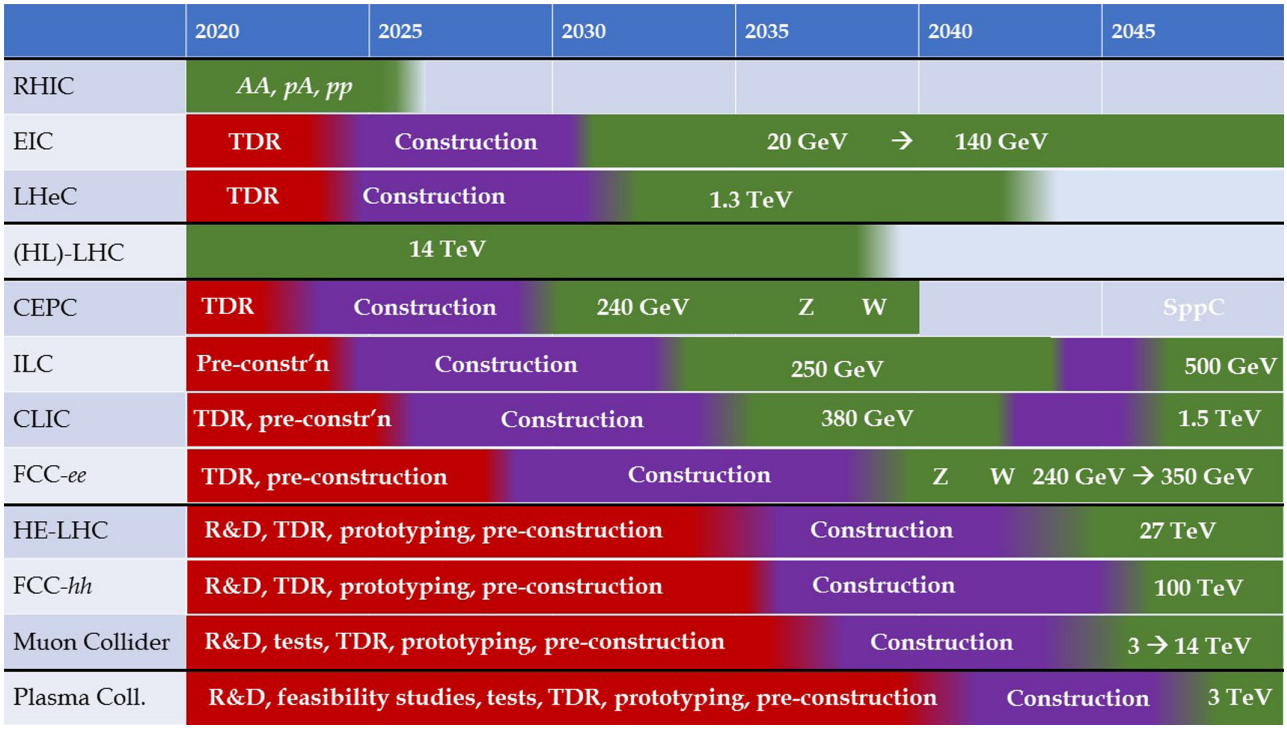

FIG. 42. Approximate technically limited timelines of future large colliding-beam facilities.

broader community, most notably because of their possible use in medicine and for generation of x rays (Albert and Thomas, 2016; Uesaka and Koyama, 2016). Several research and test facilities have already been built and are in operation, and many more are being planned (Nghiem *et al.*, 2019). It will be important for HEP accelerator designers to learn from experience, understand the applicability of PWFA advances for particle colliders, and encourage further technological development of the method. The push for more effective and cost-efficient methods of particle acceleration continues in several directions, ranging from the use of exotic particles like muons, over more advanced magnets and rf cavities, to compact high-gradient acceleration in dielectric structures or solid media plasmas.

Figure 42 illustrates approximate technically limited timelines of future large colliding-beam facilities for the next three decades based on the presentations by their proponents given and briefly discussed at the European Particle Physics Strategy Update Symposium (May 13–16, 2019, Granada, Spain) (Ellis *et al.*, 2019); also see Colby and Len (2016). In Fig. 42, each of the proposed colliders is considered individually, without any possible interference or interconnection between them, such as a sequential scenario of FCC-*hh* construction following the completion of FCC-*ee* operation, as foreseen in the FCC integrated project plan (Benedikt *et al.*, 2020). A staged construction of the FCC would be consistent with the 2020 Update of the European Strategy for Particle Physics (European Strategy Group, 2020), which recommends that "Europe, together with its international partners, should investigate the technical and financial feasibility of a future hadron collider at CERN with a centre-of-mass energy of at least 100 TeV and with an electron-positron Higgs and electroweak factory as a possible first stage."

Several factors are expected to play a role in the actual development: (i) a decisive move (for instance, the approval of any of the four Higgs factory projects will have an impact on the others); (ii) a better understanding of performance, timeline, and cost feasibility for the energy-frontier collider proposals after further R&D and more detailed project cost evaluation; and (iii) new discoveries at the LHC or other related particle-physics experiments, which might provide clear guidance and preferences for the next generation of accelerator-based HEP programs.

Under circumstances where projects under consideration in the field are becoming so large and costly that no single country or a group of countries can carry them out in isolation, coordination of efforts on regional and global levels becomes ever more critical. Discussion forums on the future of high-energy accelerators such as the Snowmass workshops (Brock *et al.*, 2014) and the Particle Physics Project Prioritization Panel in the US (Ritz *et al.*, 2019), the European Particle Physics Strategy Updates (Ellis *et al.*, 2019; European Strategy Group, 2020), the European and Asian Committees for Future Accelerators (Asian Committee for Future Accelerators, 2019; European Committee for Future Accelerators, 2019), the Nuclear Physics European Collaboration Committee (Nuclear Physics European Collaboration Committee, 2019) and a number of European Union cofunded accelerator development and coordination projects [such as TIARA (Test Infrastructure and Accelerator Research Area, 2019), ARIES (Accelerator Research and Development for European Science and Society, 2019), E-JADE (Europe-Japan Accelerator Development Exchange Programme, 2019), and EuPRAXIA (European Plasma Research Accelerator with Excellence in Applications, 2019)] transcend national or regional boundaries. Even more globally, the International Committee for

Future Accelerators (Bhat and Rubinstein, 2019), created in 1976 by the International Union of Pure and Applied Physics (International Union of Pure and Applied Physics, 2019), plays an important role as a facilitator of international collaborations, such as on the LHC, the ILC, and CLIC in the recent past, and promotes international efforts in all phases of construction and exploitation of future global accelerator facilities for particle physics.

In this review, we have presented only the most promising options for particle colliders; there are many more ideas and avenues that remain to be explored. Collider beam physics, an astonishingly fertile and dynamic research field, is still breaking new ground. We are certain that some two decades from now accelerator and beam physicists will have achieved noteworthy accomplishments resulting in better, more effective, and more economical colliding-beam facilities, as they have done repeatedly over the past 60 years.

ACKNOWLEDGMENTS

We acknowledge fruitful discussions on particle colliders with many colleagues whom we have collaborated with over the years. Special thanks go to our colleagues who provided valuable input and shared their views on various topics of this review, including G. Arduini, R. Assmann, M. Bai, S. Belomestnykh, M. Benedikt, P. Bhat, C. Biscari, A. Blondel, A. Bogacz, J. Brau, O. Brüning, A. Canepa, W. Chou, P. Collier, D. Dannheim, A. Grasselino, J. P. Delahaye, D. Denisov, V. Dolgashev, W. Fischer, J. Gao, A. Grasselino, E. Gschwendtner, M. Klein, W. Krasny, W. Leemans, E. Levichev, B. List, V. Litvinenko, I. Meshkov, E. Métral, H. Montgomery, M. Morrone, P. Muggli, D. Neuffer, K. Ohmi, K. Oide, H. Padamsee, M. Palmer, R. Palmer, N. Pastrone, N. Phinney, Q. Qin, T. Raubenheimer, L. Rivkin, A. Romanenko, M. Ross, T. Roser, L. Rossi, G. Rumolo, D. Schulte, M. Seidel, T. Sen, A. Seryi, D. Shatilov, H. Simon, S. Stapnes, M. Syphers, V. Telnov, Y. Tikhonov, S. Verdu-Andres, F. Willeke, V. Yakovlev, A. Yamamoto, J. Yang, K. Yokoya, Y. Zhang, A. Zlobin, and M. Zobov. We are grateful to P. Derwent and V. Higgins for carefully reading through the manuscript and helpful feedback. Some of this material has appeared in other forms. Many of the ideas and proposals outlined in the review were presented and discussed at the European Particle Physics Strategy Update Symposium (May 13–16, 2019, Granada, Spain) (Ellis *et al.*, 2019). V. S. was supported by Fermi National Accelerator Laboratory, which is operated by the Fermi Research Alliance under Contract No. DE-AC02-07CH11359 with the U.S. Department of Energy. F. Z. was supported by the European Organization for Nuclear Research, and by the European Commission under the Horizon 2020 project ARIES, Grant Agreement No. 730871.

REFERENCES

Abe, K., *et al.* (SLD Collaboration), 2000, Phys. Rev. Lett. **84**, 5945.
Abe, T., *et al.*, 2010, arXiv:1011.0352.
Abelleira Fernandez, J. L., *et al.* (LHeC Study Group) , 2012, J. Phys. G **39**, 075001.
Accardi, A., *et al.*, 2016, Eur. Phys. J. A **52**, 268.
Accelerator Research and Development for European Science and Society, 2019, https://aries.web.cern.ch/ (September 18, 2019).
Achasov, M., *et al.*, 2017, Nucl. Part. Phys. Proc. **287-288**, 57.
Adams, D., *et al.*, 2019, Eur. Phys. J. C **79**, 257.
Adli, E., J.-P. Delahaye, S. J. Gessner, M. J. Hogan, T. Raubenheimer, W. An, C. Joshi, and W. Mori, 2013, arXiv:1308.1145.
Adli, E., and P. Muggli, 2016, Rev. Accel. Sci. Technol. **09**, 85.
Adli, E., *et al.*, 2018, Nature (London) **561**, 363.
Adone Group, 1971, IEEE Trans. Nucl. Sci. **18**, 217.
Ado, Y. M., and V. Balbekov, 1971, At. Energ. **31**, 731.
Adolphsen, C., *et al.*, 2013, Technical Reports No. ANL-HEP-TR-13-20, No. BNL-100603-2013-IR, No. IRFU-13-59, No. Cockcroft-13-10, No. CERN-ATS-2013-037, No. CLNS-13-2085, No. FERMILAB-TM-2554, No. IHEP-AC-ILC-2013-001, No. ILC-REPORT-2013-040, No. INFN-13-04-LNF, No. JAI-2013-001, No. JINR-E9-2013-35, No. JLAB-R-2013-01, No. KEK-Report-2013-1, No. KNU-CHEP-ILC-2013-1, No. LLNL-TR-635539, No. SLAC-R-1004, and No. ILC-HiGrade-Report-2013-003. See also http://www.linearcollider.org/ILC/TDR. The full list of signatories is inside the report.
Agostini, P., *et al.*, 2020, arXiv:2007.14491.
Aicheler, M., P. N. Burrows, N. Catalan, R. Corsini, M. Draper, J. Osborne, D. Schulte, S. Stapnes, and M. Stuart, 2019, Eds., CERN Yellow Report No. CERN-2018-010-M.
Aicheler, M., P. Burrows, M. Draper, T. Garvey, P. Lebrun, K. Peach, N. Phinney, H. Schmickler, D. Schulte, and N. Toge, 2012, Eds., CERN Yellow Reports: Monographs No. CERN-2012-007, No. SLAC-R-985, No. KEK-Report-2012-1, No. PSI-12-01, and No. JAI-2012-001.
Aihara, H., *et al.* (Linear Collider Collaboration), 2019, arXiv:1901.09829.
Akai, K., K. Furukawa, and H. Koiso, 2018, Nucl. Instrum. Methods Phys. Res., Sect. A **907**, 188.
Akre, R., L. Bentson, P. Emma, and P. Krejcik, 2002, Stanford Linear Accelerator Center Technical Report No. SLAC-PUB-9241.
Albert, F., and A. G. Thomas, 2016, Plasma Phys. Controlled Fusion **58**, 103001.
Alexahin, Y., E. Gianfelice-Wendt, and V. Kapin, 2018, J. Instrum. **13**, P11002.
Alexahin, Y. I., 1998, Part. Accel. **59**, 43, https://cds.cern.ch/record/314169/files/p43.pdf.
Alharbi, K., S. Riemann, G. Moortgat-Pick, and A. Alrashdi, 2019, arXiv:1902.07755.
Alley, R., *et al.*, 1995, Nucl. Instrum. Methods Phys. Res., Sect. A **365**, 1.
Altarelli, M., *et al.*, 2006, DESY Report No. DESY-2006-097.
Amaldi, U., 1976, Phys. Lett. **61B**, 313.
Ambrosino, F., *et al.*, 2006, Phys. Lett. B **632**, 76.
Ambrosio, G., *et al.*, 2001, Fermilab Report No. FERMILAB-TM-2149.
Anashin, V., *et al.*, 2010, Phys. Lett. B **686**, 84.
Angal-Kalinin, D., *et al.*, 2018, J. Phys. G **45**, 065003.
Ankenbrandt, C., *et al.*, 1999, Phys. Rev. ST Accel. Beams **2**, 081001.
Antchev, G., *et al.* (TOTEM Collaboration), 2019, Eur. Phys. J. C **79**, 103.
Antonelli, M., M. Boscolo, R. Di Nardo, and P. Raimondi, Nucl. Instrum. Methods Phys. Res., Sect. A **807**, 101 2016.
Antonov, A., *et al.*, 2011, Nucl. Instrum. Methods Phys. Res., Sect. A **637**, 60.
Apollinari, G., I. Bejar Alonso, O. Bruning, F. P., M. Lamont, L. Rossi, and L. Tavian, 2017, CERN Technical Report No. 2017-007-M.

Arkani-Hamed, N., T. Han, M. Mangano, and L.-T. Wang, 2016, Phys. Rep. **652**, 1.

Artamonov, A., *et al.*, 1984, Phys. Lett. **137B**, 272.

Aschenauer, E., *et al.*, 2014, arXiv:1409.1633.

Asian Committee for Future Accelerators, 2019, http://www.acfa-forum.net/ (September 11, 2019).

Assmann, R., and K. Cornelis, 2000, in *Proceedings of the 7th European Particle Accelerator Conference (EPAC 2000), Vienna, 2000*, Vols. 1–3, edited by W. Mitaroff, C. Petit-Jean-Genaz, and J. Poole, p. 1187, https://accelconf.web.cern.ch/e00/PAPERS/TUP6B01.pdf.

Assmann, R., and J. Grebenyuk, 2014, in *Proceedings of the 5th International Particle Accelerator Conference (IPAC '14), Dresden, Germany, 2014*, edited by C. Petit-Jean-Genaz (JACoW, Geneva), p. 961, http://accelconf.web.cern.ch/IPAC2014/papers/tuobb01.pdf.

Assmann, R., M. Lamont, S. Myers, 2002, Nucl. Phys. B, Proc. Suppl. **109**, 17.

Assmann, R., *et al.* (LEP Energy Working Group), 1999, Eur. Phys. J. C **6**, 187.

Aulchenko, V., *et al.*, 2003, Phys. Lett. B **573**, 63.

Aune, B., *et al.*, 2000, Phys. Rev. ST Accel. Beams **3**, 092001.

Bacci, C., G. Penso, G. Salvini, B. Stella, R. Baldini-Celio, G. Capon, C. Mencuccini, G. Murtas, A. Reale, and M. Spinetti, 1972, Phys. Lett. **38B**, 551.

Bae, S., *et al.*, 2018, Phys. Rev. Accel. Beams **21**, 050101.

Baglin, V., *et al.*, 1998, CERN Technical Report No. LHC-Project-Report-188.

Bai, M., *et al.*, 2006, Phys. Rev. Lett. **96**, 174801.

Baier, V., 1972, Sov. Phys. Usp. **14**, 695.

Bailey, R., 2012, arXiv:1201.4648.

Baklakov, B., T. Bolshakov, A. Chupyra, A. Erokhin, P. Lebedev, V. Parkhomchuk, S. Singatulin, J. Lach, and V. Shiltsev, 1998, Phys. Rev. ST Accel. Beams **1**, 031001.

Baklakov, B., A. Sleptsov, A. Seryi, P. Lebedev, V. Parkhomchuk, and V. Shiltsev, 1993, Zh. Tekh. Fiz. **63**, 123[**38**, 894 (1993), https://inspirehep.net/literature/379003].

Balachandran, S., C. Tarantini, P. J. Lee, F. Kametani, Y.-F. Su, B. Walker, W. Starch, and D. C. Larbalestier, 2019, Supercond. Sci. Technol. **32**, 044006.

Balagura, V., 2011, Nucl. Instrum. Methods Phys. Res., Sect. A **654**, 634.

Balakin, V., G. Budker, E. Pakhtusova, V. Sidorov, A. Skrinsky, G. Tumaikin, and A. Khabakhpashev, 1971, Phys. Lett. **34B**, 328.

Balakin, V., A. Novokhatsky, and V. Smirnov, 1983, in *Proceedings of the 12th International Conference on High-Energy Accelerators (HEACC 1983), Batavia, IL, 1983*, edited by F. T. Cole (Fermilab, Batavia, IL), p. 119, https://inspirehep.net/files/7fed12b8dcaaf3525cc37cf50b56a545.

Balakin, V. E., and A. N. Skrinsky, 1979, Conf. Proc. C **791004**, 31, https://lss.fnal.gov/conf/C791004/p31.pdf.

Balik, G., B. Caron, D. Schulte, J. Snuverink, and J. Pfingstner, 2013, Nucl. Instrum. Methods Phys. Res., Sect. A **700**, 163.

Bambade, P., R. Erickson, W. A. Koska, W. Kozanecki, N. Phinney, and S. Wagner, 1989, Phys. Rev. Lett. **62**, 2949.

Bambade, P., *et al.*, 2010, Phys. Rev. ST Accel. Beams **13**, 042801.

Bambade, P., *et al.*, 2019, arXiv:1903.01629.

Bane, K., *et al.*, 2018, arXiv:1807.10195.

Barber, D., G. Ripken, J. Kewisch, R. Schmidt, and R. Rossmanith, 1985, Part. Accel. **17**, 243, https://cds.cern.ch/record/155608/files/p243.pdf.

Barber, D., *et al.*, 1994, Nucl. Instrum. Methods Phys. Res., Sect. A **338**, 166.

Barber, D., *et al.*, 1995, Phys. Lett. B **343**, 436.

Barber, W., B. Gittelman, G. O'Neill, and B. Richter, 1966, Phys. Rev. Lett. **16**, 1127.

Barber, W., B. Richter, W. K. Panofsky, G. O'Neill, and B. Gittelman, 1959, U.S. Atomic Energy Commission and Office of Naval Research Technical Report No. HEPL-170.

Barger, V. D., 2018, *Collider Physics* (CRC Press, Boca Raton).

Barklow, T., *et al.*, 1999, in *Proceedings of the 1999 Particle Accelerator Conference (PAC '99), New York, 1999*, edited by A. Luccio (IEEE, Piscataway, NJ), p. 307.

Barletta, W., 1996, AIP Conf. Proc. **351**, 56.

Barron, R. F., 1985, *Cryogenic Systems* (Oxford University Press, New York) .

Bartosik, N., *et al.*, 2019, arXiv:1905.03725.

Baru, S., *et al.*, 1992, Z. Phys. C **53**, 219.

Battiston, F., F. Musciotto, D. Wang, A.-L. Barabasi, M. Szell, and R. Sinatra, 2019, Nat. Rev. Phys. **1**, 89.

Baudrenghien, P., A. C. Butterworth, M. Jaussi, T. Mastoridis, G. Papotti, E. N. Shaposhnikova, and J. Tuckmantel, 2011, Conf. Proc. C **110904**, 1819, https://accelconf.web.cern.ch/IPAC2011/papers/TUPZ010.PDF.

Baudrenghien, P., and P. Collier, 1996, CERN Technical Report No. CERN-SL-96-021-OP.

Bazzi, M., *et al.*, 2011, Phys. Lett. B **704**, 113.

Bell, M., and J. S. Bell, 1995, in *Quantum Mechanics, High Energy Physics and Accelerators: Selected Papers of John S. Bell (with Commentary)*, edited by M. Bell, K. Gottfried, and M. J. G. Veltman (World Scientific, Singapore), pp. 105–114.

Bellafont, I., M. Morrone,, L. Mether, J. Fernández, R. Kersevan, C. Garion, V. Baglin, P. Chiggiato, and F. Pérez, 2020, Phys. Rev. Accel. Beams **23**, 033201.

Belomestnykh, S., 2012, Rev. Accel. Sci. Technol. **05**, 147.

Benedikt, M., A. Blondel, P. Janot, M. Michelangelo, and F. Zimmermann, 2020, Nat. Phys. **16**, 402.

Benedikt, M., D. Schulte, and F. Zimmermann, 2015, Phys. Rev. ST Accel. Beams **18**, 101002.

Benedikt, M., and F. Zimmermann, 2018, Nucl. Instrum. Methods Phys. Res., Sect. A **907**, 200.

Benedikt, M., *et al.*, 2019a, Eur. Phys. J. Special Topics **228**, 261.

Benedikt, M., *et al.*, 2019b, Annu. Rev. Nucl. Part. Sci. **69**, 389.

Benedikt, M., *et al.*, 2019c, Eur. Phys. J. Special Topics **228**, 755.

Benson, S., *et al.*, 2018, in *Proceedings of the 9th International Particle Accelerator Conference (IPAC '18), Vancouver, Canada, 2018*, edited by J. Thomson, T. Satogata, and V. Schaa (JACoW Publishing, Geneva), p. 382.

Ben-Zvi, I., 2016, Supercond. Sci. Technol. **29**, 103002.

Berkaev, D., *et al.*, 2012, Nucl. Phys. B, Proc. Suppl. **225–227**, 303.

Berkelman, K., 2004, *A Personal History of CESR and CLEO: The Cornell Electron Storage Ring and Its Main Particle Detector Facility* (World Scientific, Singapore).

Bernardini, C., 2004, Phys. Perspect. **6**, 156.

Bernardini, C., G. Corazza, G. Di Giugno, G. Ghigo, J. Haissinski, P. Marin, R. Querzoli, and B. Touschek, 1963, Phys. Rev. Lett. **10**, 407.

Bernardini, C., G. Corazza, G. Di Giugno, J. Haissinski, P. Marin, R. Querzoli, and B. Touschek, 1964, Nuovo Cimento **34**, 1473.

Bernardini, C., G. Corazza, G. Ghigo, and B. Touschek, 1960, Nuovo Cimento **18**, 1293.

Besnier, G., D. Brandt, and B. Zotter, 1984 Part. Accel. **17**, 51, https://cds.cern.ch/record/154782/files/p51.pdf.

Bevan, A., *et al.*, 2014, Eur. Phys. J. C **74**, 3026.

Bhat, C., 2004, Phys. Lett. A **330**, 481.

Bhat, P., and R. Rubinstein, 2019, Rev. Accel. Sci. Technol. **10**, 303.
Bjorken, J., 1983, Part. Accel. **13**, 115, https://cds.cern.ch/record/140304/files/p115.pdf.
Blaskiewicz, M., J. M. Brennan, and K. Mernick, 2010, Phys. Rev. Lett. **105**, 094801.
Blinov, A., 1983, in *Proceedings of the 12th International Conference on High-Energy Accelerators, Batavia, IL, 1983*, edited by F. T. Cole and R. Donaldson (Fermi National Accelerator Laboratory, Batavia, IL), p. 183.
Blinov, V., A. Bogomyagkov, N. Y. Muchnoi, S. Nikitin, I. Nikolaev, A. Shamov, and V. Zhilich, 2009, Nucl. Instrum. Methods Phys. Res., Sect. A **598**, 23.
Blinov, V., *et al.*, 2014, Phys. Part. Nucl. Lett. **11**, 620.
Blondel, A., A. Chao, W. Chou, J. Gao, D. Schulte, and K. Yokoya, 2013, arXiv:1302.3318.
Blondel, A., and P. Janot, 2019, arXiv:1912.11871.
Blondel, A., *et al.*, 2019, arXiv:1909.12245.
Bogacz, S., J. Ellis, L. Lusito, D. Schulte, T. Takahashi, M. Velasco, M. Zanetti, and F. Zimmermann, 2012, arXiv:1208.2827.
Bogomilov, M., *et al.*, 2020, Nature (London) **578**, 53.
Bogomyagkov, A., V. Druzhinin, E. Levichev, A. Milstein, and S. Sinyatkin, 2018, EPJ Web Conf. **181**, 01032.
Bogomyagkov, A., E. Levichev, and D. Shatilov, 2014, Phys. Rev. ST Accel. Beams **17**, 041004.
Bohringer, T., *et al.*, 1980, Phys. Rev. Lett. **44**, 1111.
Bonvicini, G., E. Gero, R. Frey, W. Koska, C. Field, N. Phinney, and A. Minten, 1989, Phys. Rev. Lett. **62**, 2381.
Bordais, L., *et al.*, 2012, CERN Technical Report No. TIARA-REP-WP3-2012-004.
Bordry, F., M. Benedikt, O. Bruning, J. Jowett, L. Rossi, D. Schulte, S. Stapnes, and F. Zimmermann, 2018, arXiv:1810.13022.
Boscolo, M., H. Burkhardt, and M. Sullivan, 2017, Phys. Rev. Accel. Beams **20**, 011008.
Boscolo, M., J. P. Delahaye, and M. Palmer, 2019, Rev. Accel. Sci. Technol. **10**, 189.
Bowring, D., *et al.*, 2020, Phys. Rev. Accel. Beams **23**, 072001.
Bramham, P., G. Carron, H. Hereward, K. Hubner, W. Schnell, and L. Thorndahl, 1975, Nucl. Instrum. Methods **125**, 201.
Brandt, D., H. Burkhardt, M. Lamont, S. Myers, and J. Wenninger, 2000, Rep. Prog. Phys. **63**, 939.
Braun, H. H., S. Dobert, I. Wilson, and W. Wuensch, 2003, Phys. Rev. Lett., **90**, 224801.
Brock, R., *et al.*, 2014, arXiv:1401.6081.
Brodsky, S. J., 2016, Eur. Phys. J. A **52**, 220.
Broemmelsiek, D., *et al.*, 2018, New J. Phys. **20**, 113018.
Brookhaven National Laboratory, 2020, https://www.bnl.gov/newsroom/news.php?a=116982 (February 29, 2020).
Brown, I. G., 2004, *The Physics and Technology of Ion Sources* (John Wiley & Sons, New York).
Brown, P., O. Brunner, A. Butterworth, E. Ciapala, H. Frischholz, G. Geschonke, E. Peschardt, and J. Sladen, 2001, in *Proceedings of the IEEE Particle Accelerator Conference (PACS 2001), Chicago, 2001*, Vol. 2 (IEEE, New York), p. 1059.
Bruning, O., 2018, CERN Technical Report No. CERN-ACC-2018-0061.
Bruning, O., H. Burkhardt, and S. Myers, 2012 Prog. Part. Nucl. Phys. **67**, 705.
Bruning, O., and P. Collier, 2007, Nature (London) **448**, 285.
Bruning, O., J. Jowett, M. Klein, D. Pellegrini, D. Schulte, and F. Zimmermann, 2017, CERN Technical Report No. CERN-ACC-2017-0019.
Bubley, A., M. Bryzgunov, A. Denisov, A. Goncharov, V. Panasyuk, V. Parkhomchuk, and V. Reva, 2017, in *Proceedings for the 25th Russian Particle Accelerator Conference (RuPAC '16), St. Petersburg, Russia, 2016* (JACoW Publishing, Geneva), p. 452.
Budker, G., 1967, Phys. Usp. **9**, 534.
Budker, G. I., 1970a, in *Proceedings of the 7th International Conference on High-Energy Accelerators, Yerevan, USSR, 1969*, Vol. 1, edited by A. Alikhanian (Akademii Nauk Armyanskoj Institut Fiziki, Yerevan, USSR), p. 33.
Budker, G. I., 1970b, in *Proceedings of the 15th International Conference on High-Energy Physics (ICHEP '70), Kiev, 1970*, edited by V. P. Shelest, Yu. A. Budagov, L. L. Jenkovszky, A. A. Komar, V. Kukhtin (Naukova Dumka, Kiev), p. 1017, https://cds.cern.ch/record/108467/files/C70-08-26-ENTIRE.pdf.
Budker, G. I., B. G. Yerozolimsky, and A. A. Naumov, 1962, in *Proceedings of the Workshop on Physics and Technics of Colliding Beams, Kharkov, USSR, 1962*, Part 2 (Kharkov Institute of Physics and Technology, Kharkov, USSR).
Bunce, G., N. Saito, J. Soffer, and W. Vogelsang, 2000, Annu. Rev. Nucl. Part. Sci. **50**, 525.
Buon, J., and K. Steffen, 1986, Nucl. Instrum. Methods Phys. Res., Sect. A **245**, 248.
Burkhardt, H., and R. Kleiss, 1995, Conf. Proc. C **940627**, 1353, http://accelconf.web.cern.ch/e94/PDF/EPAC1994_1353.PDF.
Burov, A., 2016, Phys. Rev. Accel. Beams **19**, 084402.
Burov, A., J. Marriner, V. Shiltsev, V. Danilov, and G. Lambertson, 2000, Nucl. Instrum. Methods Phys. Res., Sect. A **450**, 194.
Butterworth, A., P. Brown, O. Brunner, E. Ciapala, H. Frischholz, G. Geschonke, E. Peschardt, and J. Sladen, 2008, Nucl. Instrum. Methods Phys. Res., Sect. A **587**, 151.
Caldwell, A., K. Lotov, A. Pukhov, and F. Simon, 2009, Nat. Phys. **5**, 363.
Caldwell, A., and M. Wing, 2016, Eur. Phys. J. C **76**, 463.
Carlsten, B. E., 1995, Part. Accel. **49**, 27, https://cds.cern.ch/record/1108320/files/p27.pdf.
Carver, L., *et al.*, 2019, in *Proceedings of the 10th International Particle Accelerator Conference (IPAC '19), Melbourne, 2019*, edited by R. Dowd (JACoW Publishing, Geneva), p. 338.
Caspi, S., *et al.*, 2014, IEEE Trans. Appl. Supercond. **24**, 1.
CEPC Study Group, 2018, arXiv:1809.00285.
CERN, 1999, Report No. CERN-DI-9906025.
CERN, 2017, https://cds.cern.ch/record/2255762/files/CERN-Brochure-2017-002-Eng.pdf (September 18, 2019).
CERN, 2019a, https://fap-dep.web.cern.ch/rpc/2019-annual-contributions-cern-budget (April 1, 2019).
CERN, 2019b, CERN Courier **59**, 13, https://cds.cern.ch/record/2666160.
Chao, A., and R. D. Ruth, 1985, Part. Accel. **16**, 201, https://inspirehep.net/files/4ceedc6b5506902bdc2de2ec9499fe4a.
Chao, A. W., 1985, AIP Conf. Proc. **127**, 201.
Chao, A. W., 1993, *Physics of Collective Beam Instabilities in High Energy Accelerators* (Wiley, New York).
Chao, A. W., K. H. Mess, M. Tigner, and F. Zimmermann, 2013, *Handbook of Accelerator Physics and Engineering*, 2nd ed. (World Scientific, Singapore).
Chao, A. W., B. Richter, and C.-Y. Yao, 1980, Nucl. Instrum. Methods **178**, 1.
Chao, A. W., *et al.*, 2013, *Handbook of Accelerator Physics and Engineering* (World Scientific, Singapore).
Chao, K.-T., and Wang, Y., Eds., 2008, IHEP Report No. IHEP-Physics-Report-BES-III-2008-001.
Chen, J., 2018, in *Probing Nucleons, and Nuclei in High Energy Collisions*, edited by A. Prokudin, Y. Hatta, Y. Kovchegov, and C. Marquet (World Scientific, Singapore).
Chen, P., 1992, Phys. Rev. D **46**, 1186.

Chen, P., J. Dawson, R. W. Huff, and T. Katsouleas, 1985, Phys. Rev. Lett. **54**, 693.
Chen, P., and R. J. Noble, 1997, AIP Conf. Proc. **398**, 273.
Chen, X., 2018, arXiv:1809.00448.
Cho, A., 2020, Science **367**, 235.
Chorowski, M., H. Correia Rodrigues, D. Delikaris, P. Duda, C. Haberstroh, F. Holdener, S. Klöppel, C. Kotnig, F. Millet, and J. Polinski, 2017, IOP Conf. Ser. Mater. Sci. Eng. **278**, 012097.
Chou, W., G. Mourou, N. Solyak, T. Tajima, and M. Velasco, 2013, arXiv:1305.5202.
Chung, M., *et al.*, 2013, Phys. Rev. Lett. **111**, 184802.
Church, M., and J. Marriner, 1993, Annu. Rev. Nucl. Part. Sci. **43**, 253.
Cid-Vidal, X., and R. Cid, 2011, Phys. Educ. **46**, 45.
Clarke, J. A., 2004, *The Science and Technology of Undulators and Wigglers*, Vol. 4 (Oxford University Press, New York).
Clendenin, J. E., *et al.*, 1988, in *Proceedings of the 14th International Linear Accelerator Conference (LINAC '88), Williamsburg, VA, 1988*, edited by A. Soltys (CEBAF, Newport News, VA), https://inspirehep.net/literature/264914.
Cockcroft, J. D., and E. T. Walton, 1932, Proc. R. Soc. A **136**, 619.
Colby, E. R., and L. Len, 2016, Rev. Accel. Sci. Technol. **09**, 1.
Collette, C., K. Artoos, A. Kuzmin, S. Janssens, M. Sylte, M. Guinchard, and C. Hauviller, 2010, Nucl. Instrum. Methods Phys. Res., Sect. A **621**, 71.
Cosme, G., B. Jean-Marie, S. Jullian, F. Laplanche, J. Lefrançois, A. Liberman, G. Parrour, J. Repellin, G. Sauvage, and G. Szklarz, 1972, Phys. Lett. **40B**, 685.
Courant, E. D., and A. M. Sessler, 1966, Rev. Sci. Instrum. **37**, 1579.
Courant, E. D., and H. S. Snyder, 1958, Ann. Phys. (N.Y.) **3**, 1.
Crease, R. P., 2005a, Phys. Perspect. **7**, 330.
Crease, R. P., 2005b, Phys. Perspect. **7**, 404.
Cronin, J. W., 2004, *Fermi Remembered*, Vol. 12 (University of Chicago Press , Chicago).
Cros, B., and P. Muggli (ALEGRO Collaboration), 2019, https://indico.cern.ch/event/765096/contributions/3295514/ (September 18, 2019).
Danilov, V., P. Ivanov, I. Koop, I. Nesterenko, E. Perevedentsev, D. Shatilov, Y. M. Shatunov, and A. Skrinsky, 1996, in *Proceedings of the 5th European Particle Accelerator Conference, Sitges, Spain, 1996*, Vol. 96, edited by S. Myers, A. Pacheco, R. Pascual, C. Petit-Jean-Genaz, and J. Poole (IOP, Bristol, England), p. 1149.
Danilov, V., and E. Perevedentsev, 1997, Nucl. Instrum. Methods Phys. Res., Sect. A **391**, 77.
Dawson, J. M., 1959, Phys. Rev. **113**, 383.
Dawson, J. W., and M. N. Polyanskiy, 2018, in *Proceedings of the 18th IEEE Advanced Accelerator Concepts Workshop (AAC), Breckenridge, CO, 2018*, edited by E. Simakov (IEEE, New York), p. 1.
De Florian, D., *et al.*, 2016, arXiv:1610.07922.
Dehning, B., A. Melissinos, F. Perrone, C. Rizzo, and G. Von Holtey, 1990, Phys. Lett. B **249**, 145.
Delahaye, J. P., 2018, in *Proceedings of the ARIES Muon Collider Workshop, Padua, 2018*, https://indico.cern.ch/event/719240/contributions/2966555/.
Delahaye, J. P., B. Mansoulie, M. Diemoz, D. Schulte, A. Wulzer, A. Skrinsky, L. Rivkin, N. Pastrone, and K. Long, 2019, arXiv:1901.06150.
Delahaye, J.-P., 2016, in *Challenges and Goals for Accelerators in the XXI Century*, edited by O. Brüning and S. Myers (World Scientific, Singapore), pp. 561–572.
d'Enterria, D., 2017, Proc. Sci. ICHEP2016, 434 [arXiv:1701.02663].
Derbenev, Y., 1973, Technical Report No. SLAC-TRANS-0151.
Derbenev, Y. S., A. Skrinsky, Y. M. Shatunov, G. Tumaikin, S. Serednyakov, and A. Kondratenko, 1978, Part. Accel. **8**, 115, https://inspirehep.net/files/3d1ba4e45a59386e2b20da3d307b636a.
Derbenev, Y. S., A. Skrinsky, Y. M. Shatunov, G. Tumaikin, S. Serednyakov, and A. Kondratenko, 1980, Part. Accel. **10**, 177, https://cds.cern.ch/record/1107974/files/p177.pdf.
Dhakal, P., G. Ciovati, P. Kneisel, and G. R. Myneni, 2015, IEEE Trans. Appl. Supercond. **25**, 3500104.
Dikanskij, N., and D. Pestrikov, 1982, Part. Accel. **12**, 27, https://cds.cern.ch/record/1107996/files/p27.pdf.
Dimopoulou, C., K. Beckert, P. Beller, A. Dolinskii, U. Laier, F. Nolden, G. Schreiber, M. Steck, and J. Yang, 2007, Phys. Rev. ST Accel. Beams **10**, 020101.
Dolgashev, V., S. Tantawi, Y. Higashi, and B. Spataro, 2010, Appl. Phys. Lett. **97**, 171501.
Dominguez, O., K. Li, G. Arduini, E. Metral, G. Rumolo, F. Zimmermann, and H. M. Cuna, 2013, Phys. Rev. ST Accel. Beams **16**, 011003.
Dorda, U., 2008, CERN Technical Report No. CERN-THESIS-2008-055.
Dugan, G., 1989, Part. Accel. **26**, 121, https://cds.cern.ch/record/201386/files/p121.pdf.
Edwards, D. A., and M. J. Syphers, 2008, *An Introduction to the Physics of High Energy Accelerators* (John Wiley & Sons, New York).
Edwards, H. T., 1985, Annu. Rev. Nucl. Part. Sci. **35**, 605.
Eichten, E., I. Hinchliffe, K. Lane, and C. Quigg, 1984, Rev. Mod. Phys. **56**, 579.
Eliasson, P., 2008, Phys. Rev. ST Accel. Beams **11**, 051003.
Ellis, J., 2018, arXiv:1810.11263.
Ellis, R. K., W. J. Stirling, and B. R. Webber, 2003, *QCD and Collider Physics* (Cambridge University Press, Cambridge, England).
Ellis, R. K., *et al.* (European Strategy for Particle Physics Preparatory Group), 2019, arXiv:1910.11775.
ELSA Working Group, 2019, http://www-elsa.physik.uni-bonn.de/accelerator_list.html (February 19, 2019).
Emanov, F., *et al.*, 2018, Phys. Part. Nucl. Lett. **15**, 720.
Emma, P., L. J. Hendrickson, P. Raimondi, and F. Zimmermann, 1997, Conf. Proc. C **970512**, 452, https://accelconf.web.cern.ch/pac97/papers/pdf/5B007.PDF.
Emma, P., and T. Raubenhemier, 2001, Phys. Rev. ST Accel. Beams **4**, 021001.
England, J., *et al.*, 2014, Rev. Mod. Phys. **86**, 1337.
Englert, F., 2014, Rev. Mod. Phys. **86**, 843.
Erickson, R., *et al.*, 1984, *SLAC Linear Collider Design Handbook* (Stanford Linear Accelerator Center, Menlo Park, CA).
Esarey, E., C. Schroeder, and W. Leemans, 2009, Rev. Mod. Phys. **81**, 1229.
European Committee for Future Accelerators, 2019, https://ecfa.web.cern.ch/ (September 18, 2019).
European Plasma Research Accelerator with Excellence in Applications, 2019, http://www.eupraxia-project.eu/ (September 18, 2019).
European Strategy Group, 2020, CERN Technical Report No. CERN-ESU-013, https://home.cern/sites/home.web.cern.ch/files/2020-06/2020 Update European Strategy.pdf.
Europe-Japan Accelerator Development Exchange Programme, 2019, https://www.e-jade.eu/ (September 18, 2019).
Evans, L., 2016, Technol. Forecast. Soc. Change **112**, 4.
Evans, L., and P. Bryant, 2008, J. Instrum. **3**, S08001.

Evans, L., and S. Michizono, 2017, CERN Technical Report No. KEK-2017-3.
Evans, L. R., 2009, *The Large Hadron Collider: A Marvel of Technology* (EPFL Press, Lausanne, Switzerland).
FAIR Project, https://www.gsi.de/fileadmin/oeffentlichkeitsarbeit/fair/RevBoardReport_190429_Public.pdf (September 10, 2019).
Fartoukh, S., 2013, Phys. Rev. ST Accel. Beams **16**, 111002.
Fartoukh, S., 2014, Phys. Rev. ST Accel. Beams **17**, 111001.
Fernow, R. C., and R. C. Fernow, 1989, *Introduction to Experimental Particle Physics* (Cambridge University Press, Cambridge, England).
Finocchiaro, G., *et al.*, 1980, Phys. Rev. Lett. **45**, 222.
Fischer, G. E., 1987, AIP Conf. Proc. **153**, 1047.
Fischer, W., *et al.*, 2008, Phys. Rev. ST Accel. Beams **11**, 041002.
Fischer, W., *et al.*, 2015 Phys. Rev. Lett. **115**, 264801.
Flanagan, J., K. Ohmi, H. Fukuma, S. Hiramatsu, M. Tobiyama, and E. Perevedentsev, Phys. Rev. Lett. **94**, 054801 2005.
Fowler, W., 1990, Part. Accel. **208**, 179.
Frauenfelder, H., and E. Henley, 1991, *Subatomic Physics*, 2nd ed. (Prentice-Hall, Englewood Cliffs, NJ), p. 286.
Funakoshi, Y., 2014, CERN Report No. CERN-2014-004, p. 27.
Furman, M. A., 1994, Conf. Proc. C **940627**, 1144, https://accelconf.web.cern.ch/e94/PDF/EPAC1994_1144.PDF.
Furman, M. A. (LHC US Collaboration), 1998, CERN Technical Reports No. LHC-Project-Report-180 and No. CERN-LHC-Project-Report-180.
Gai, W., 2009, AIP Conf. Proc. **1086**, 3.
Gai, W., J. Power, and C. Jing, 2012, J. Plasma Phys. **78**, 339.
Gai, W., P. Schoessow, B. Cole, R. Konecny, J. Norem, J. Rosenzweig, and J. Simpson, 1988, Phys. Rev. Lett. **61**, 2756.
Gaiduk, A., and Y. Pestov, 1976, Budker Institute of Nuclear Physics Technical Report No. BINP 76-67.
Gao, J., 2017 (private communication).
Gareyte, J., 1999, CERN Report No. CERN-SL-00-039 AP.
Geer, S., 1998, Phys. Rev. D **57**, 6989.
Geer, S., 2009, Annu. Rev. Nucl. Part. Sci. **59**, 347.
Giacomelli, G., and M. Jacob, 1979, Phys. Rep. **55**, 1.
Gianotti, F., *et al.*, 2005, Eur. Phys. J. C **39**, 293.
Ginzburg, I. F., G. L. Kotkin, V. I. Telnov, and V. Serbo, 1983, Nucl. Instrum. Methods **205**, 47.
Gittelman, B., 1965, IEEE Trans. Nucl. Sci. **12**, 1033.
Giudice, G. F., 2019, arXiv:1902.07964.
Golovatyuk, V., V. Kekelidze, V. Kolesnikov, O. Rogachevsky, and A. Sorin, 2016, Eur. Phys. J. A **52**, 212.
Gonsalves, A., *et al.*, 2019, Phys. Rev. Lett. **122**, 084801.
Gonzalez, L., M. Gil-Costa, V. Baglin, P. Chiggiato, C. Garion, R. Kersevan, S. Casalbuoni, E. Huttel, I. Bellafont, and F. Perez, 2019, Phys. Rev. Accel. Beams **22**, 083201.
Grassellino, A., A. Romanenko, D. Sergatskov, O. Melnychuk, Y. Trenikhina, A. Crawford, A. Rowe, M. Wong, T. Khabiboulline, and F. Barkov, 2013, Supercond. Sci. Technol. **26**, 102001.
Grassellino, A., *et al.*, 2018, arXiv:1806.09824.
Green, D., 2000, *The Physics of Particle Detectors*, Vol. 12 (Cambridge University Press, Cambridge, England).
Gronberg, J., 2014, Rev. Accel. Sci. Technol. **07**, 161.
Grudiev, A., S. Calatroni, and W. Wuensch, 2009, Phys. Rev. ST Accel. Beams **12**, 102001.
Gruner, S. M., D. Bilderback, I. Bazarov, K. Finkelstein, G. Krafft, L. Merminga, H. Padamsee, Q. Shen, C. Sinclair, and M. Tigner, 2002, Rev. Sci. Instrum. **73**, 1402.
Grupen, C., and B. Shwartz, 2008, *Particle Detectors*, Vol. 26 (Cambridge University Press, Cambridge, England).
Gu, X., *et al.*, 2017, Phys. Rev. Accel. Beams **20**, 023501.
Gupta, R., *et al.*, IEEE Trans. Appl. Supercond. **24**, 1, 2014.
Gutbrod, H. H., I. Augustin, H. Eickhoff, K. Gross, W. Henning, D. Kramer, and G. Walter, 2006, GSI Technical Report, https://www.researchgate.net/publication/230785058_FAIR_Baseline_Technical_Report.
Haissinski, J., 1969, CERN Report No. CERN-1969-029, p. 61.
Hangst, J., M. Kristensen, J. Nielsen, O. Poulsen, J. Schiffer, and P. Shi, 1991, Phys. Rev. Lett. **67**, 1238.
Hauptman, J., 2011, *Particle Physics Experiments at High Energy Colliders* (John Wiley & Sons, New York).
Haussecker, E. F., and A. W. Chao, 2011, Phys. Perspect. **13**, 146. We extended the original analysis period of the paper (1939–2009) to 1939–2018.
Heifets, S., and S. Kheifets, 1991, Rev. Mod. Phys. **63**, 631.
Helm, R., *et al.*, 1983, IEEE Trans. Nucl. Sci. **30**, 2001.
Hendrickson, L., S. Bes, P. Grossberg, D. McCormick, N. Phinney, P. Raimondi, and M. Ross, 1999, in *Proceedings of the International Conference on Accelerator and Large Experimental Physics Control Systems (ICALEPCS '97), Beijing, 1997*, https://www3.aps.anl.gov/News/Conferences/1997/icalepcs/paper97/p126.pdf.
Herb, S., *et al.*, 1977, Phys. Rev. Lett. **39**, 252.
Higgs, P. W., 2014, Rev. Mod. Phys. **86**, 851.
Himel, T., and J. Siegrist, 1985, AIP Conf. Proc. **130**, 602.
Hirata, K., 1995, Phys. Rev. Lett. **74**, 2228.
Hirata, K., and F. Ruggiero, 1990, Part. Accel. **28**, 137, https://cds.cern.ch/record/200329/files/p137.pdf.
Hoddeson, L., L. Brown, M. Dresden, and M. Riordan, 1997, *The Rise of the Standard Model: A History of Particle Physics from 1964 to 1979* (Cambridge University Press, Cambridge, England).
Hofmann, I., 2017, *Space Charge Physics for Particle Accelerators* (Springer, New York).
Hogan, M. J., 2016, Rev. Accel. Sci. Technol. **09**, 63.
Holmes, S. D., and V. D. Shiltsev, 2013, Annu. Rev. Nucl. Part. Sci. **63**, 435.
Huang, H., *et al.*, 1994, Phys. Rev. Lett. **73**, 2982.
International Union of Pure and Applied Physics, 2019, https://archive.iupap.org (September 18, 2019).
Issinsky, I., P. Rukoyatkin, A. Kovalenko, and A. Kirillov, 1994, Acta Phys. Pol. **25**, 673, Dhttps://www.actaphys.uj.edu.pl/fulltext?series=Reg&vol=25&page=673.
Jackson, G., 1996, Fermilab Technical Report No. FNAL-TM-1991.
Janot, P., and S. Jadach, 2020, Phys. Lett. B **803**, 135319.
Jing, C., 2016, Rev. Accel. Sci. Technol. **09**, 127.
Johnsen, K., 1973, Nucl. Instrum. Methods **108**, 205.
Jowett, J., 2018, in *Proceedings of the 9th International Particle Accelerator Conference (IPAC '18), Vancouver, Canada, 2018*, edited by S. Koscielniak, T. Satogata, V. R. W. Schaa, and J. Thomson (JACoW Publishing, Geneva), p. 584.
Kamihara, Y., H. Hiramatsu, M. Hirano, R. Kawamura, H. Yanagi, T. Kamiya, and H. Hosono, 2006, J. Am. Chem. Soc. **128**, 10012.
Karliner, M., and K. Popov, 2005, Nucl. Instrum. Methods Phys. Res., Sect. A **537**, 481.
Kayran, D., *et al.*, 2019, in *Proceedings of the 10th International Particle Accelerator Conference (IPAC '19), Melbourne, 2019*, edited by M. Boland, H. Tanaka, D. Button, R. Dowd, V. R. W. Schaa, and E. Tan (JACoW Publishing, Geneva, Switzerland), p. 769.
Kayran, D., *et al.*, 2020, Phys. Rev. Accel. Beams **23**, 021003.
KEK B-Factory, 1995, KEK Technical Report No. KEK-Report-95-07.

Kekelidze, V., R. Lednicky, V. Matveev, I. Meshkov, A. Sorin, and G. Trubnikov, 2012, Phys. Part. Nucl. Lett. **9**, 313.
Kekelidze, V., R. Lednicky, V. Matveev, I. Meshkov, A. Sorin, and G. Trubnikov, 2016, Eur. Phys. J. A **52**, 211.
Kerst, D., F. Cole, H. Crane, L. Jones, L. J. Laslett, T. Ohkawa, A. Sessler, K. Symon, K. Terwilliger, and N. V. Nilsen, 1956, Phys. Rev. **102**, 590.
Kheifets, S., and B. Zotter, 1998, *Impedances and Wakes in High Energy Particle Accelerators* (World Scientific, Singapore).
Khodzhibagiyan, H., *et al.*, 2019, IEEE Trans. Appl. Supercond. **29**, 1.
Kimura, Y., 1986, in *Proceedings of the 13th International Conference on High-Energy Accelerators, Novosibirsk, Soviet Union, 1986*, edited by A. N. Skrinsky, https://cds.cern.ch/record/111903
Klein, M., and R. Yoshida, 2008, Prog. Part. Nucl. Phys. **61**, 343.
Koba, K., and J. Steimel, 2002, AIP Conf. Proc. **642**, 223.
Kohaupt, R. D., 1980, Experientia **40**, 562, http://old.inspirehep.net/record/155228?ln=en
Kostromin, S., V. Borisov, A. Bichkov, O. Golubitsky, A. Donyagin, N. Morozov, E. Samsonov, M. Omelyanenko, H. Khodzhibagiyan, and A. Shemchuk, 2016, Phys. Part. Nucl. Lett. **13**, 855.
Kostromin, S., I. Meshkov, A. Sidorin, A. Smirnov, G. Trubnikov, and N. Shurkhno, 2012, Phys. Part. Nucl. Lett. **9**, 322.
Koutchouk, J.-P., 2001, in *Proceedings of the 19th IEEE Particle Accelerator Conference, Chicago, 2001*, editor by P. W. Lucas and S. Webber (JACoW Publishing, Geneva), p. 1681.
Krasny, M., *et al.*, 2018, in *Proceedings of the 9th International Particle Accelerator Conference (IPAC 2018), Vancouver, Canada, 2018*, edited by S. Koscielniak, T. Satogata, V. R. W. Schaa, and J. Thomson (IOP, Bristol, England), p. WEYGBD3.
Krasny, M. W., 2015, arXiv:1511.07794.
Krasny, W. N., A. Petrenko, and W. Płaczek, 2020, Prog. Part. Nucl. Phys. **114**, 103792.
Krejcik, P., *et al.*, 1992, in *Proceedings of the 3rd European Particle Accelerator Conference (EPAC '92), Berlin, 1992*, edited by H. Henke, H. Homeyer, and Ch. Petit-Jean-Genaz, p. 527, http://accelconf.web.cern.ch/e92/PDF/EPAC1992_0527.PDF.
Krishnagopal, S., and R. Siemann, 1991, Phys. Rev. Lett. **67**, 2461.
Kubo, K., 2011, Phys. Rev. ST Accel. Beams **14**, 014401.
Kuiper, B., 1994, Europhys. News **25**, 66.
Kulikov, A., A. Fisher, S. Heifets, J. Seeman, M. Sullivan, U. Wienands, and W. Kozanecki, 2001, in *Proceedings of the 19th IEEE Particle Accelerator Conference, Chicago, 2001*, Vol. 3, edited by P W. Lucas and S. Webber (IEEE, New York), p. 1903.
Kurdadze, L., A. Onuchin, S. Serednyakov, V. Sidorov, and S. Eidelman, 1972, Phys. Lett. **42B**, 515.
Kuroo, N., K. Ohmi, K. Oide, D. Zhou, and F. Zimmermann, 2018, Phys. Rev. Accel. Beams **21**, 031002.
Kuze, M., 2018, Int. J. Mod. Phys. Conf. Ser. **46**, 1860081.
Lafferty, J. M., 1998, Ed., *Foundations of Vacuum Science and Technology* (John Wiley & Sons, New York).
Lauer, I., U. Eisenbarth, M. Grieser, R. Grimm, P. Lenisa, V. Luger, T. Schätz, U. Schramm, D. Schwalm, and M. Weidemüller, 1998, Phys. Rev. Lett. **81**, 2052.
Lavine, T. L., 1992, in *Proceedings of the 3rd European Particle Accelerator Conference (EPAC '92), Berlin, 1992*, Vol. 1, edited by H. Henke, H. Homeyer, and Ch. Petit-Jean-Genaz (JACoW Publishing, Geneva), p. 302.
Lawrence, E. O., and M. S. Livingston, 1932, Phys. Rev. **40**, 19.
Lebedev, V., A. Burov, and S. Nagaitsev, 2016, Rev. Accel. Sci. Technol. **09**, 187.
Lebedev, V., and V. Shiltsev, 2014, *Accelerator Physics at the Tevatron Collider* (Springer, New York).
Le Duff, J., M. Level, P. Marin, E. Sommer, and H. Zyngier, 1980, in *Proceedings of the 11th International Conference on High-Energy Accelerators, Geneva, 1980*, edited by W. S. Newman (Springer, New York), p. 707.
Lee, P. J. (NHMFL Collaboration), 2019, https://nationalmaglab.org/magnet-development/applied-superconductivity-center/plots (September 18, 2019).
Lee, S.-Y., 1997, *Spin Dynamics and Snakes in Synchrotrons* (World Scientific, Singapore).
Lee, S.-Y., 2018, *Accelerator Physics* (World Scientific, Singapore).
Leemans, W., and E. Esarey, 2009, Phys. Today **62**, No. 3, 44.
Levedev, V., V. Parkhomchuk, V. Shiltsev, and G. Stupakov, 1994, Part. Accel. **44**, 147, https://cds.cern.ch/record/248620/files/p147.pdf.
Levichev, E., 2014, Rev. Accel. Sci. Technol. **07**, 207.
Levichev, E. B., A. N. Skrinsky, G. M. Tumaikin, and Y. M. Shatunov, 2018, Phys. Usp. **61**, 405.
Liepe, M., and J. Knobloch, 2006, Nucl. Instrum. Methods Phys. Res., Sect. A **557**, 354.
List, B., 2019, Report No. ILC-CR-0018, https://agenda.linearcollider.org/event/8389/contributions/45111/attachments/35278/54677/ILC-CR-0018.pdf.
Litos, M., *et al.*, 2014, Nature (London) **515**, 92.
Litos, M., *et al.*, 2016, Plasma Phys. Controlled Fusion **58**, 034017.
Litvinenko, V. N., and Y. S. Derbenev, 2009, Phys. Rev. Lett. **102**, 114801.
Litvinenko, V. N., T. Roser, and M. Chamizo-Llatas, 2020, Phys. Lett. B **804**, 135394.
Livingston, M. S., 1954, *High Energy accelerators* (Interscience, New York).
Luo, Q., W. Gao, J. Lan, W. Li, and D. Xu, 2019, in *Proceedings of the 10th International Particle Accelerator Conference (IPAC '19), Melbourne, 2019*, edited by M. Boland, H. Tanaka, D. Button, R. Dowd, V. R. W. Schaa, and E. Tan (JACoW Publishing, Geneva), p. 643.
Maclean, E. H., *et al.*, 2019, Phys. Rev. Accel. Beams **22**, 061004.
Magnus, W., and S. Winkler, 1979, *Hill's Equation* (Dover, New York).
Marcellini, F., and D. Alesini, 2004, in *Proceedings of the 9th European Particle Accelerator Conference (EPAC04), Lucerne, Switzerland, 2004*, Vol. 4, edited by C. Petit-Jean-Genaz (JACoW Publishing, Geneva), p. 689.
Marin, P. C., *et al.* (Orsay Storage Ring Group), 1965, in *Proceedings of the 5th International Conference on High Energy Accelerators, Frascati, Italy, 1965*, edited by M. Grilli, p. 271, https://inspirehep.net/files/72cb29229227ddb3c8d7134f5ccacfcf.
Martin, R., M. I. Besana, F. Cerutti, A. Langner, R. Tomás, E. Cruz-Alaniz, and B. Dalena, 2017, Phys. Rev. Accel. Beams **20**, 081005.
Martinello, M., M. Checchin, A. Romanenko, A. Grassellino, S. Aderhold, S. Chandrasekeran, O. Melnychuk, S. Posen, and D. Sergatskov, 2018, Phys. Rev. Lett. **121**, 224801.
McDaniel, B., 1981, IEEE Trans. Nucl. Sci. **28**, 1983.
McDonald, K., *et al.*, 2009, *Proceedings of the Particle Accelerator Conference (PAC '09), Vancouver, Canada*, edited by P. Schmor and S. Koschelniak, p. 795, http://accelconf.web.cern.ch/PAC2009/papers/tu4gri03.pdf.
McIntyre, P. M., S. Assadi, S. Bannert, D. Chavez, J. Gerity, N. Pogue, A. Sattarov, J. Breitschopf, and J. N. Kellams, 2016, in *Proceedings of the 2016 North American Particle Accelerator Conference (NA-PAC '16), Chicago, 2016*, edited by M. Power,

V. Shiltsev, V. R. W. Schaa, and M. White (JACoW Publishing, Geneva), p. 13.
McMillan, E. M., 1945, Phys. Rev. **68**, 143.
Mellado, B., 2013, in *Proceedings of the 21st International Workshop on Deep-Inelastic Scattering and Related Subjects (DIS 2013), Marseilles, France, 2013*, edited by C. Diaconu, E. Perez, B. Pire, V. Radescu, C. Royon, E. Sauvan, and L. Schoeffel, p. 264, https://pos.sissa.it/cgi-bin/reader/conf.cgi?confid=191.
Merminga, L., D. R. Douglas, and G. A. Krafft, 2003, Annu. Rev. Nucl. Part. Sci., **53**, 387.
Mess, K.-H., and M. Seidel, 1994, Nucl. Instrum. Methods Phys. Res., Sect. A **351**, 279.
Mess, K.-H., *et al.*, 1996, *Superconducting Accelerator Magnets* (World Scientific, Singapore).
Métral, E., 1999, Part. Accel. **62**, 259.
Métral, E., 2016, in *Proceedings of the 57th ICFA Advanced Beam Dynamics Workshop on High-Intensity, High Brightness and High Power Hadron Beams, Malmö, Sweden, 2016*, https://cds.cern.ch/record/380927/files/ps-99-011.pdf .
Métral, E., *et al.*, 2014, CERN Report No. CERN-ACC-NOTE-2014-0006.
Métral, E., *et al.*, 2017 CERN Report No. CERN-ACC-NOTE-2017-0005.
Michnoff, R., *et al.*, 2019, in *Proceedings of the 10th International Particle Accelerator Conference (IPAC '19), Melbourne, 2019*, edited by M. Boland, H. Tanaka, D. Button, R. Dowd, V. R. W. Schaa, and E. Tan (JACoW Publishing, Geneva), p. 1651.
Minty, M. G., and F. Zimmermann, 2013, *Measurement and Control of Charged Particle Beams* (Springer Science+Business Media, New York).
Mohayai, T. A., 2018, arXiv:1806.01807.
Mokhov, N., Y. Alexahin, V. Kashikhin, S. Striganov, and A. Zlobin, 2012, arXiv:1202.3979.
Mokhov, N., *et al.*, 2010, Int. J. Mod. Phys. A **25**, 98.
Mokhov, N., *et al.*, 2011, J. Instrum. **6**, T08005.
Month, M., 2003, *Weep for Isabelle: A Rhapsody in a Minor Key—A Historical Novel Depicting the Rise and Fall of Big Physics in the Second Half of the Twentieth Century* (Avant Garde Press, Nicosia).
Moortgat-Pick, G., *et al.*, 2008, Phys. Rep. **460**, 131.
Mourou, G., 2019, Rev. Mod. Phys. **91**, 030501.
Mourou, G., B. Brocklesby, T. Tajima, and J. Limpert, 2013, Nat. Photonics **7**, 258.
Muggli, P., and B. Cros, 2018, in *Proceedings of the 9th International Particle Accelerator Conference (IPAC '18), Vancouver, Canada, 2018*, edited by S. Koscielniak, T. Satogata, V. R. W. Schaa, and J. Thomson (JACoW Publishing, Geneva), p. 1619.
Myers, S., 2020, Phys. Rev. Accel. Beams **23**, 124802.
Myers, S., and O. Brüning, 2016, Eds., *Challenges and Goals for Accelerators in the XXI Century* (World Scientific, Singapore).
Myers, S., and H. Schopper, 2013, Eds., *Numerical Data and Functional Relationships in Science and Technology*, Landolt-Bornstein—Group I: Elementary Particles, Nuclei and Atoms, Vol. 21, https://doi.org/10.1007/978-3-642-23053-0.
Nagaitsev, S., *et al.*, 2006, Phys. Rev. Lett. **96**, 044801.
Napoly, O., 1993, Part. Accel. **40**, 181, https://cds.cern.ch/record/240071/files/CM-P00062693.pdf.
National Academies of Sciences, Engineering, and Medicine, 2018, *An Assessment of U.S.-Based Electron-Ion Collider Science* (National Academies Press, Washington, DC).
Nelson, W., and J. W. N. Tuyn, 1979, CERN Technical Report No. CERN-HS-RP/037.
Nesemann, H., and K. Wille, 1983, IEEE Trans. Nucl. Sci. **30**, 1998.
Neuffer, D., 1983, Part. Accel. **14**, 75, https://cds.cern.ch/record/142710/files/p75.pdf.
Neuffer, D., and V. Shiltsev, 2018, J. Instrum. **13**, T10003.
Neuffer, D. V., and S. Peggs, 1986, Superconducting Super Collider Technical Report No. SSC-63.
Ng, K.-Y., 2006, *Physics of Intensity Dependent Beam Instabilities* (World Scientific, Singapore).
Nghiem, P. A. P., *et al.*, 2019, in *Proceedings of the 10th International Particle Accelerator Conference (IPAC '19), Melbourne, 2019*, edited by M. Boland, H. Tanaka, D. Button, R. Dowd, V. R. W. Schaa, and E. Tan (JACoW Publishing, Geneva), p. 2291.
Nishikawa, T., S. Ozaki, and Y. Kimura, 1983, Surv. High Energy Phys. **3**, 161.
Nobel Foundation, 2020, http://www.nobelprize.org/prizes/physics/ (February 27, 2020).
Norris, B., and J. C. Theilacker, 1989, in *Supercollider 1*, edited by M. McAshan (Springer, New York), pp. 321–328.
Nuclear Physics European Collaboration Committee, 2019, http://www.nupecc.org/ (September 18, 2019).
Ohmi, K., 1995, Phys. Rev. Lett. **75**, 1526.
Ohmi, K., N. Kuroo, K. Oide, D. Zhou, and F. Zimmermann, 2017, Phys. Rev. Lett. **119**, 134801.
Ohnishi, Y., 2018, in *Proceedings of the 9th International Particle Accelerator Conference (IPAC '18), Vancouver, Canada, 2018*, edited by S. Koscielniak, T. Satogata, V. R. W. Schaa, and J. Thomson (JACoW Publishing, Geneva), p. 1, http://accelconf.web.cern.ch/ipac2018/papers/moxgb1.pdf
Ohnishi, Y., *et al.*, 2013, Prog. Theor. Exp. Phys. 2013, 3A011.
Oide, K., 2009 Prog. Theor. Phys. **122**, 69.
Oide, K., 2014, Rev. Accel. Sci. Technol. **07**, 35.
Oide, K., and K. Yokoya, 1989, Phys. Rev. A **40**, 315.
Oide, K., *et al.*, 2016, Phys. Rev. Accel. Beams **19**, 111005.
O'Neill, G. K., 1956, Phys. Rev. **102**, 1418.
Orsay Storage Ring Group, 1979, IEEE Trans. Nucl. Sci. **26**, 3559.
Otboyev, A. V., and E. A. Perevedentsev, 1999, Phys. Rev. ST Accel. Beams **2**, 104401.
Padamsee, H., 2019, Rev. Accel. Sci. Technol. **10**, 125.
Padamsee, H., J. Knobloch, and T. Hays, 2008, *RF Superconductivity for Accelerators*, Vol. 2011 (Wiley-VCH, Weinheim).
Palmer, R., 1988, Stanford Linear Accelerator Center Technical Report No. SLAC-PUB-4707.
Palmer, R., 2014, Rev. Accel. Sci. Technol. **07**, 137.
Palmer, R., *et al.*, 1996, in AIP Conf. Proc. **372**, 3.
Papaphilippou, Y., and F. Zimmermann, 1999, Phys. Rev. ST Accel. Beams **2**, 104001.
Parkhomchuk, V., V. Shiltsev, and G. Stupakov, 1993, Part. Accel. **46**, 241, https://cds.cern.ch/record/1108302/files/p241.pdf
Parkhomchuk, V., and A. Skrinsky, 2000, Phys. Usp. **43**, 433.
Parkhomchuk, V., and A. Skrinsky, 2008, Rev. Accel. Sci. Technol. **01**, 237.
Paterson, J., 1975, IEEE Trans. Nucl. Sci. **22**, 1366.
Patrignani, C., T. K. Pedlar, and J. L. Rosner, 2013, Annu. Rev. Nucl. Part. Sci. **63**, 21.
Peggs, S., and T. Satogata, 2017, *Introduction to Accelerator Dynamics* (Cambridge University Press, Cambridge, England).
Pellegrini, C. M., and A. M. Sessler, 1995, Eds., *The Development of Colliders* (American Institute of Physics, College Park, MD).
PEP-II Collaboration, 1993, PEP-II and SLAC Technical Reports No. SLAC-418 and No. LBL-PUB-5379.
Peralta, E., *et al.*, 2013, Nature (London) **503**, 91.
Perkins, D. H., 2000, *Introduction to High Energy Physics* (Cambridge University Press, Cambridge, England), p. 148.

Persson, T., *et al.*, 2017a, Phys. Rev. Accel. Beams **20**, 061002.
Persson, T., *et al.*, 2017b Phys. Rev. Accel. Beams **20**, 061002.
Pestrikov, D. V., 1993, Nucl. Instrum. Methods Phys. Res., Sect. A **336**, 427.
Pfingstner, J., E. Adli, and D. Schulte, 2017, Phys. Rev. ST Accel. Beams **20**, 011006.
Phinney, N., 2000, arXiv:physics/0010008.
Phinney, N., N. Toge, and N. Walker, 2007, arXiv:0712.2361.
Piekarz, H., S. Hays, J. Blowers, B. Claypool, and V. Shiltsev, 2019, Nucl. Instrum. Methods Phys. Res., Sect. A **943**, 162490.
Piekarz, H., *et al.*, 2006, IEEE Trans. Appl. Supercond. **16**, 342.
Pieloni, T., and W. Herr, 2013, *Proceedings of the CERN Accelerator School, Erice, Italy, 2013*, edited by W. Herr (CERN, Geneva), p.431 [arXiv:1601.05235].
Piminov, P., 2018, Phys. Part. Nucl. Lett. **15**, 732.
Piwinski, A., 1986, in *Nonlinear Dynamics Aspects of Particle Accelerators*, Lecture Notes in Physics Vol. 247, edited by J. M. Jowett, M. Month, and S. Turner (Springer, New York), pp. 104–120.
Piwinski, A., 1988, in *Frontiers of Particle Beams*, Lecture Notes in Physics Vol. 296, edited by M. Month and S. Turner (Springer, New York), pp. 297–309, https://doi.org/10.1007/BFb0031487.
Piwinski, A., J. D. Bjorken, and S. K. Mtingwa, 2018, Phys. Rev. Accel. Beams **21**, 114801.
Podobedov, B., and R. H. Siemann, 1995, Phys. Rev. E **52**, 3066.
Qin, Q., *et al.*, 2012, in *Proceedings of the Third International Particle Accelerator Conference (IPAC '12), New Orleans, 2012*, edited by F. Zimmermann and C. Eyberger, p. 1030, https://cds.cern.ch/record/1445554.
Quigg, C., 2011a, arXiv:1101.3201.
Quigg, C., 2011b, CERN Courier **51**, 20, https://cerncourier.com/a/long-live-the-tevatron/.
Quigg, C., 2019, Rev. Accel. Sci. Technol. **10**, 3.
Raimondi, P., 2006, in *Proceedings of the 2nd SuperB Workshop, Frascati, Italy, 2006*, edited by C. Petit-Jean-Genaz (unpublished).
Raimondi, P., D. N. Shatilov, and M. Zobov, 2007, arXiv:physics/0702033.
Raimondi, P., M. Zobov, and D. Shatilov, 2008, Conf. Proc. C **0806233**, WEPP045.
Ranjbar, V., *et al.*, 2017, in *Proceedings of the 8th International Particle Accelerator Conference (IPAC '17), Copenhagen, 2017*, edited by G. Arduini, M. Lindroos, J. Pranke, V. R. W. Schaa, M. Seidel (JACoW Publishing, Geneva, Switzerland), p. 2188.
Ranjbar, V., M. Blaskiewicz, F. Méot, C. Montag, S. Tepikian, S. Brooks, H. Witte, I. Marneris, V. Ptitsyn, and F. J. Willeke, 2018, Phys. Rev. Accel. Beams **21**, 111003.
Ranjbar, V. H., *et al.*, 2004, Phys. Rev. ST Accel. Beams **7**, 051001.
Raubenheimer, T., and F. Zimmermann, 1995, Phys. Rev. E **52**, 5487.
Raubenheimer, T. O., 2000, Phys. Rev. ST Accel. Beams **3**, 121002.
Rees, J. R., 1986, Beam Line **9**, 1, https://www.slac.stanford.edu/vault/pubvault/bln19801989/bln1986marsp.pdf.
Reiser, M., 2008, *Theory and Design of Charged Particle Beams* (John Wiley & Sons, New York).
Riordan, M., L. Hoddeson, and A. W. Kolb, 2015, *Tunnel Visions: The Rise and Fall of the Superconducting Super Collider* (University of Chicago Press, Chicago).
Ritz, S., *et al.*, 2019, https://www.usparticlephysics.org/wp-content/uploads/2018/03/FINAL_P5_Report_053014.pdf (September 11, 2019).
Robinson, K. W., and G. A. Voss, 1966, Cambridge Electron Accelerator Report No. CEAL-TM-149.
Robson, A., P. Burrows, N. C. Lasheras, L. Linssen, M. Petric, D. Schulte, E. Sicking, S. Stapnes, and W. Wuensch, 2018, arXiv:1812.07987.
Roser, T., 2008, AIP Conf. Proc. **980**, 15.
Rossbach, J., 1987, Part. Accel. **23**, 121, https://cds.cern.ch/record/184292/files/p121.pdf.
Rossi, L., and L. Bottura, 2012, Rev. Accel. Sci. Technol. **05**, 51.
Rossi, L., and D. Tommasini, 2019, Rev. Accel. Sci. Technol. **10**, 157.
Rubbia, C., 1985, Rev. Mod. Phys. **57**, 699.
Rubbia, C., P. McIntyre, and D. Cline, 1977, in *Proceedings of the International Neutrino Conference Aachen 1976*, edited by H. Faissner (Springer, New York), p. 683.
Rubin, D., 1989, Part. Accel. **26**, 63, https://cds.cern.ch/record/201605/files/p63.pdf.
Ruggiero, F., and F. Zimmermann, 2002, Phys. Rev. ST Accel. Beams **5**, 061001.
Rumolo, G., F. Ruggiero, and F. Zimmermann, 2001, Phys. Rev. ST Accel. Beams **4**, 012801.
Salam, G., and A. Weiler, 2019, http://collider-reach.web.cern.ch/ (September 17, 2019).
Sands, M., 1970, Stanford Linear Accelerator Center Technical Report No. SLAC-121.
Sandström, R. (for the MICE Collaboration), 2008, AIP Conf. Proc. **981**, 107.
Satoh, M., 2010, Conf. Proc. C **100523**, THPD006, http://accelconf.web.cern.ch/IPAC10/papers/thpd006.pdf.
Savin, I., A. Efremov, D. Peshekhonov, A. Kovalenko, O. Teryaev, O. Shevchenko, A. Nagajcev, A. Guskov, V. Kukhtin, and N. Toplilin, 2016, Eur. Phys. J. A **52**, 215.
Sayed, H. K., R. B. Palmer, and D. Neuffer, 2015, Phys. Rev. ST Accel. Beams **18**, 091001.
Scandale, W., 2014, Rev. Accel. Sci. Technol. **07**, 9.
Scandale, W., *et al.*, 2016, Phys. Lett. B **758**, 129.
Schael, S., *et al.* (ALEPH, DELPHI, L3, OPAL, and SLD Collaborations, LEP Electroweak Working Group, SLD Electroweak Group, and SLD Heavy Flavour Group), 2006, Phys. Rep. **427**, 257.
Scharf, W. H., 1989, *Particle Accelerators: Applications in Technology and Research* (Research Studies Press, Baldock, England).
Schaumann, M., *et al.*, 2019, in *Proceedings of the 10th International Particle Accelerator Conference (IPAC 2019), Melbourne, 2019*, edited by M. Boland, H. Tanaka, D. Button, R. Dowd, V. R. W. Schaa, and E. Tan (JACoW Publishing, Geneva), p. 689, http://accelconf.web.cern.ch/ipac2019/papers/moprb055.pdf.
Schenk, M., X. Buffat, L. R. Carver, R. De Maria, K. Li, and E. Métral, 2018, Phys. Rev. Accel. Beams **21**, 084401.
Schmidt, R., *et al.*, 2006, New J. Phys. **8**, 290.
Schoerling, D., and Zlobin, A., 2019, Eds., *Nb_3Sn Accelerator Magnets* (Springer, New York) .
Schröder, S., *et al.*, 1990, Phys. Rev. Lett. **64**, 2901.
Schroeder, C., E. Esarey, C. Benedetti, and W. Leemans, 2016, AIP Conf. Proc. **1777**, 020001.
Schroeder, C., E. Esarey, C. Geddes, C. Benedetti, and W. Leemans, 2010, Phys. Rev. ST Accel. Beams **13**, 101301.
Schroeder, C. B., E. Esarey, and W. P. Leemans, 2012, Phys. Rev. ST Accel. Beams **15**, 051301.
Schulte, D., 2016, Rev. Accel. Sci. Technol. **09**, 209.
Seeman, J., 2008a, in *Proceedings of the 11th European Particle Accelerator Conference (EPAC '08), Genoa, Italy, 2008*, edited by C. Boscari and C. Petit-Jean-Genaz (JACoW Publishing, Geneva), p. 23.

Seeman, J., 2008b, in *Proceedings of the 11th European Particle Accelerator Conference (EPAC '08), Genoa, Italy, 2008* (JACoW Publishing, Geneva), p. 946.
Seeman, J., 2015, in *Proceedings of the 55th ICFA Advanced Beam Dynamics Workshop on High Luminosity Circular e^+e^- Colliders Higgs Factory (HF 2014), Beijing, 2014*, edited by N. Zhao and V. R. W. Schaa, p. SAT4A1, https://accelconf.web.cern.ch/HF2014/papers/proceed.pdf.
Seeman, J., *et al.*, 2006, in *Proceedings of the 10th European Particle Accelerator Conference (EPAC '06), Edinburgh, 2006*, Vol. 4, edited by C. Biscari, H. Owen, C. Petit-Jean-Genaz, J. Poole, and J. Thomason (JACoW Publishing, Geneva), p. 643, https://cds.cern.ch/record/687798.
Seeman, J. T., 1986, in *Nonlinear Dynamics Aspects of Particle Accelerators*, Lecture Notes in Physics Vol. 247, edited by J. M. Jowett, M. Month, and Stuart Turner (Springer, New York), pp. 121–153.
Seeman, J. T., 1992, AIP Conf. Proc. **255**, 19.
Sen, T., and J. Norem, 2002, Phys. Rev. ST Accel. Beams **5**, 031001.
Senes, E., T. Argyropoulos, F. Tecker, and W. Wuensch, 2018, Phys. Rev. Accel. Beams **21**, 102001.
Senger, P., 2016, Eur. Phys. J. A **52**, 217.
Sery, A., and O. Napoly, 1996, Phys. Rev. E **53**, 5323.
Sessler, A., and E. Wilson, 2014, *Engines of Discovery: A Century of Particle Accelerators* (World Scientific, Singapore).
Sessler, A. M., 1998, Phys. Today **51**, No. 3, 48.
Shamov, A., *et al.*, 2009, Nucl. Phys. B, Proc. Suppl. **189**, 21.
Shao, J., *et al.*, 2018, in *Proceedings of the 9th International Particle Accelerator Conference (IPAC 2018), Vancouver, Canada, 2018*, edited by S. Koscielniak, T. Satogata, V. R. W. Schaa, and J. Thomson, 640, https://accelconf.web.cern.ch/ipac2018/papers/tuygbe3.pdf.
Shatilov, D., E. Levichev, E. Simonov, and M. Zobov, 2011, Phys. Rev. ST Accel. Beams **14**, 014001.
Shatunov, P., *et al.*, 2016, Phys. Part. Nucl. Lett. **13**, 995.
Shatunov, Y., *et al.*, 2000, in *Proceedings of the 7th European Particle Accelerator Conference (EPAC 2000), Vienna, 2000*, edited by W. A. Mitaroff, C. Petit-Jean-Genaz, J. Poole, M. Regler, and J. L. Laclare, p. 439, https://cds.cern.ch/record/444438?ln=en.
Shatunov, Y., *et al.*, 2018, Phys. Part. Nucl. Lett. **15**, 310.
Shemyakin, D., *et al.*, 2016, Phys. Lett. B **756**, 153.
Shiltsev, V., 1996, Nucl. Instrum. Methods Phys. Res., Sect. A **374**, 137.
Shiltsev, V., 2010a, Phys. Rev. ST Accel. Beams **13**, 094801.
Shiltsev, V., 2010b, Mod. Phys. Lett. A **25**, 567.
Shiltsev, V., 2011, Mod. Phys. Lett. A **26**, 761.
Shiltsev, V., 2012a, Phys. Usp. **55**, 965.
Shiltsev, V., 2012b, Mod. Phys. Lett. A **27**, 1230001.
Shiltsev, V., 2014, J. Instrum. **9**, T07002.
Shiltsev, V., 2015, Int. J. Mod. Phys. A **30**, 1544001.
Shiltsev, V., 2016, *Electron Lenses for Super-Colliders* (Springer, New York).
Shiltsev, V., 2019, Int. J. Mod. Phys. A **34**, 1943002.
Shiltsev, V., Y. Alexahin, K. Bishofberger, V. Kamerdzhiev, G. Kuznetsov, and X.-L. Zhang, 2007, Phys. Rev. Lett. **99**, 244801.
Shiltsev, V., Y. Alexahin, V. Lebedev, P. Lebrun, R. Moore, T. Sen, A. Tollestrup, A. Valishev, and X. Zhang, 2005, Phys. Rev. ST Accel. Beams **8**, 101001.
Shiltsev, V., V. Danilov, D. Finley, and A. Sery, 1999, Phys. Rev. ST Accel. Beams **2**, 071001.
Shiltsev, V., and T. Tajima, 2019, Int. J. Mod. Phys. A **34**, 1943001.
Shiltsev, V., *et al.*, 2008, Phys. Rev. ST Accel. Beams **11**, 103501.
Shin, Y., A. Lumpkin, and R. Thurman-Keup, 2015, Nucl. Instrum. Methods Phys. Res., Sect. B **355**, 94.
Shin, Y.-M., D. A. Still, and V. Shiltsev, 2013, Phys. Plasmas **20**, 123106.
Simon, H., 2007, Nucl. Phys. **A787**, 102.
Sissakian, A., and A. Sorin (NICA Collaboration), 2009, J. Phys. G **36**, 064069.
Skrinskii, A. N., and Y. M. Shatunov, 1989, Phys. Usp. **32**, 548.
Skrinsky, A., 2002, Nucl. Instrum. Methods Phys. Res., Sect. A **494**, 1.
Skrinsky, A., and V. Parkhomchuk, 1981, Sov. J. Part. Nucl. **12**, 223, https://hep.princeton.edu//~mcdonald/mumu/physics/skrinsky_sjpn_12_223_81.pdf.
Sokolov, A., and I. Ternov, 1964, Sov. Phys. Dokl., **8**, 1203.
Stancari, G., A. Valishev, G. Annala, G. Kuznetsov, V. Shiltsev, D. Still, and L. Vorobiev, 2011, Phys. Rev. Lett. **107**, 084802.
Stapnes, S., CERN Council Open Symposium on the Update of European Strategy for Particle Physics, Granada, Spain, 2019, https://indico.cern.ch/event/808335/.
Steerenberg, R., *et al.*, 2019, in *Proceedings of the 10th International Particle Accelerator Conference (IPAC '19), Melbourne, 2019*, edited by M. Boland, H. Tanaka, D. Button, V. R. W Schaa, and E. Tan (JACoW Publishing, Geneva), p. 504, http://accelconf.web.cern.ch/ipac2019/papers/mopmp031.pdf.
Steinke, S., *et al.*, 2016, Nature (London) **530**, 190.
Stephans, G., 2006, J. Phys. G **32**, S447.
Sterbini, G., *et al.*, 2019, in *Proceedings of the 10th International Particle Accelerator Conference (IPAC '19), Melbourne, 2019*, M. Boland, H. Tanaka, D. Button, R. Dowd, V. R. W. Schaa, and E. Tan (JACoW Publishing, Geneva), p. 2262, http://accelconf.web.cern.ch/ipac2019/papers/weyyplm3.pdf.
Suda, T., and H. Simon, 2017, Prog. Part. Nucl. Phys. **96**, 1.
Sun, Y.-P., R. Assmann, J. Barranco, R. Tomás, T. Weiler, F. Zimmermann, R. Calaga, and A. Morita, 2009, Phys. Rev. ST Accel. Beams **12**, 101002.
Syresin, E., *et al.*, 2019, in *Proceedings of the 10th International Particle Accelerator Conference (IPAC 2019), Melbourne, 2019* (JACoW Publishing, Geneva), p. 452.
Tajima, T., and M. Cavenago, 1987, Phys. Rev. Lett. **59**, 1440.
Tajima, T., and J. M. Dawson, 1979, Phys. Rev. Lett. **43**, 267.
Tajima, T., X. Yan, and T. Ebisuzaki, 2020, Rev. Mod. Plasma Phys. **4**, 7.
Takahashi, T., 2019, Rev. Accel. Sci. Technol. **10**, 215.
Talman, R., 1995, Phys. Rev. Lett. **74**, 1590.
Tanabashi, M., *et al.*, 2018, Phys. Rev. D **98**, 030001.
Tanabe, J. T., 2005, *Iron Dominated Electromagnets: Design, Fabrication, Assembly, and Measurements* (World Scientific, Singapore).
Tang, J., 2017, ICFA Beam Dyn. Newsl. **72**, 121, http://www.icfa-bd.org/Newsletter72.pdf.
Telnov, V., 1995, Nucl. Instrum. Methods Phys. Res., Sect. A **355**, 3.
Telnov, V., 2014, J. Instrum. **9**, C09020.
Telnov, V. I., 2013, Phys. Rev. Lett. **110**, 114801.
Telnov, V. I., Nucl. Instrum. Methods Phys. Res., Sect. A **260**, 304 1987.
Teng, L., 2001, in *Proceedings of the Second Asian Particle Accelerator Conference, Beijing, 2001* (Academia Sinica, Beijing), p. 926.
Test Infrastructure and Accelerator Research Area, 2019, http://www.eu-tiara.eu/ (September 18, 2019).
Thompson, M., *et al.*, 2008, Phys. Rev. Lett. **100**, 214801.
Tigner, M., 1965, Nuovo Cimento **37**, 1228.

Tikhonin, F., 1968, Joint Institute for Nuclear Research Report No. P2-4120.
Todesco, E., and J. Wenninger, 2017, Phys. Rev. Accel. Beams **20**, 081003.
Tollestrup, A., and E. Todesco, 2008, Rev. Accel. Sci. Technol. **01**, 185.
Tomas, R., 2017, in Proceedings of the EuCARD-2 XBEAM Strategy Workshop: From EuCARD-2 XBEAM to ARIES APEC, Valencia, Spain, 2017, edited by A. Faus-Golfe, G. Franchetti, and F. Zimmermann, p. 22, https://indico.cern.ch/event/587477/.
Tomás, R., *et al.*, 2012, Phys. Rev. ST Accel. Beams **15**, 091001.
Tumaikin, G. M., 1977, in *Proceedings of the 10th , International Conference on High Energy Particle Accelerators, Serpukhov, USSR, 1977*, Vol. 1 (Institute of High Energy Physics, Protvino, USSR), p. 443, https://inis.iaea.org/collection/NCLCollectionStore/_Public/10/435/10435083.pdf.
Tygier, S., R. B. Appleby, R. Bruce, D. Mirarchi, S. Redaelli, and A. Valloni, 2019, Phys. Rev. Accel. Beams **22**, 023001.
Uesaka, M., and K. Koyama, 2016, Rev. Accel. Sci. Technol. **09**, 235.
U.S. Department of Energy, Office of Science, 2016, https://science.osti.gov/-/media/hep/pdf/accelerator-rd-stewardship/Advanced_Accelerator_Development_Strategy_Report.pdf (August 3, 2020).
U.S. Department of Energy, Office of Science User Facilities, 2019, https://science.energy.gov/user-facilities/ (February 18, 2019).
Valdivia García, M. A., and F. Zimmermann, 2019, in *Proceedings of the 10th International Particle Accelerator Conference (IPAC 2019), Melbourne, 2019*, edited by M. Boland, H. Tanaka, D. Button, R. Dowd, V. R. W. Schaa, and E. Tan (JACoW Publishing, Geneva), p. 516, http://accelconf.web.cern.ch/ipac2019/papers/mopmp035.pdf.
Valentino, G., R. Assmann, R. Bruce, S. Redaelli, A. Rossi, N. Sammut, and D. Wollmann, 2012, Phys. Rev. ST Accel. Beams **15**, 051002.
van der Meer, S., 1968, CERN Technical Report No. ISR-PO/68-31.
van der Meer, S., 1972, CERN Technical Report No. ISR-PO/72-31.
van der Meer, S., 1985, Rev. Mod. Phys. **57**, 689.
Veksler, V., 1944, Dokl. Akad. Nauk SSSR **43**, 346, http://lhe.jinr.ru/rus/veksler/wv0/publikacii/1944Veksler.pdf.
Veksler, V., 1957, Sov. J. At. En. **2**, 525.
VEPP-4 Group, 1980, in *Proceedings of the 11th International Conference on High-Energy Accelerators, Geneva, 1980*, edited by W. S. Newman (Springer, Basel), p. 38, https://link.springer.com/chapter/10.1007/978-3-0348-5540-2_5.
Verdu-Andres, S., S. Belomestnykh, I. Ben-Zvi, R. Calaga, Q. Wu, and B. Xiao, 2016, Nucl. Part. Phys. Proc. **273–275**, 193.
Verdu-Andres, S., and Q. Wu, 2019, in *Proceedings of the 10th International Particle Accelerator Conference (IPAC 2019), Melbourne, 2019*, edited by M. Boland, H. Tanaka, D. Button, R. Dowd, V. R. W. Schaa, and E. Tan (JACoW Publishing, Geneva), p. 818, http://accelconf.web.cern.ch/ipac2019/papers/moprb109.pdf.
Vignola, G., 1996, in *Proceedings of the 5th European Particle Accelerator Conference (EPAC '96), Sitges, Spain, 1996*, edited by S. Myers, A. Pacheco, R. Pascual, C. Petit-Jean-Genaz, and J. Poole (JACOW Publishing, Geneva), p. 22.
Von Holtey, G., 1987, CERN Report No. CERN-LEP-BI-87-04.
Voss, G., and B. Wiik, 1994, Annu. Rev. Nucl. Part. Sci. **44**, 413.
Voss, G.-A., 1996, in *History of Original Ideas and Basic Discoveries in Particle Physics*, Nato Science Series B Vol. 352, edited by H. B. Newman and T. Ypsilantis (Springer, New York), pp. 465–487.
Voss, G.-A., *et al.*, 1979, IEEE Trans. Nucl. Sci. **26**, 2670.
Walker, P., *et al.*, 2017, J. Phys. Conf. Ser. **874**, 012029.
Waloschek, P., 2013, *The Infancy of Particle Accelerators: Life and Work of Rolf Wideroe* (Springer Science+Business Media, New York).
Weingarten, W., 1996, CERN Technical Report No. CERN-1996-003.
Weng, W., 1987, AIP Conf. Proc. **153**, 348.
Wenninger, J., 2019 (unpublished), https://cds.cern.ch/record/2668326.
Wheeler, J., G. Mourou, and T. Tajima, 2019, Rev. Accel. Sci. Technol. **10**, 227.
Wideroe, R., 1953, German Patent No. 876279.
Wiedemann, H., 2003, *Particle Accelerator Physics* (Springer, New York).
Wiedemann, H., 2012, *Particle Accelerator Physics II: Nonlinear and Higher-Order Beam Dynamics* (Springer Science+Business Media, New York).
Willeke, F., 2006, in *Proceedings of the 10th European Particle Accelerator Conference (EPAC '06), Edinburgh, 2006*, Vol. 4, edited by C. Biscari, H. Owen, Ch. Petit-Jean-Genaz, J. Poole, and J. Thomason (JACoW Publishing, Geneva), p. 3621.
Willeke, F., *et al.*, 2019, Brookhaven National Laboratory Technical Report No. BNL-211943-2019-FORE.
Wojcicki, S., 2009, Rev. Accel. Sci. Technol. **02**, 265.
Wolf, B., 2017, *Handbook of Ion Sources* (CRC Press, Boca Raton).
Wootton, K. P., Z. Wu, B. M. Cowan, A. Hanuka, I. V. Makasyuk, E. A. Peralta, K. Soong, R. L. Byer, and R. J. England, 2016, Opt. Lett. **41**, 2696.
Xu, J., 1983, in *Proceedings of the 12th International Conference on High-Energy Accelerators, Batavia, IL, 1983*, edited by F. T. Cole and R. Donaldson (Fermi National Accelerator Laboratory, Batavia, IL), p. 157.
Xu, X., X. Peng, J. Rochester, M. Sumption, and M. Tomsic, 2019, arXiv:1903.08121.
Xu, X., M. Sumption, X. Peng, and E. Collings, 2014, Appl. Phys. Lett. **104**, 082602.
Yamamoto, A., and Y. Makida, 2002, Nucl. Instrum. Methods Phys. Res., Sect. A **494**, 255.
Yang, J., *et al.*, 2013, Nucl. Instrum. Methods Phys. Res., Sect. B **317**, 263.
Yarba, V., 1990, Part. Accel. **26**, 131, https://cds.cern.ch/record/1108085/files/p131.pdf.
Yin Vallgren, C., *et al.*, 2011, Phys. Rev. ST Accel. Beams **14**, 071001.
Yokoya, K., and P. Chen, 1992, in *Frontiers of Particle Beams: Intensity Limitations*, Lecture Notes in Physics Vol. 400, edited by M. Dienes, M. Month, and S. Turner (Springer, New York), p. 415.
Yokoya, K., Y. Funakoshi, E. Kikutani, H. Koiso, and J. Urakawa, 1989, Part. Accel. **27**, 181, https://cds.cern.ch/record/200504/files/p181.pdf.
Young, E., S. Henderson, R. Littauer, B. McDaniel, T. Pelaia, and R. Talman, 1998, in *Proceedings of the 17th Particle Accelerator Conference (PAC '97), Vancouver, Canada, 1997* (IEEE, Piscataway, NJ), https://accelconf.web.cern.ch/pac97/papers/pdf/3B003.PDF.
Zelenski, A., 2010, Rev. Sci. Instrum. **81**, 02B308.
Zhang, X., T. Tajima, D. Farinella, Y. Shin, G. Mourou, J. Wheeler, P. Taborek, P. Chen, F. Dollar, and B. Shen, 2016, Phys. Rev. Accel. Beams **19**, 101004.
Zhang, X.-L., K. Bishofberger, V. Kamerdzhiev, V. Lebedev, V. Shiltsev, R. Thurman-Keup, and A. Tollestrup, 2008, Phys. Rev. ST Accel. Beams **11**, 051002.

Zhang, Y., 2019, in *Proceedings of the 10th International Particle Accelerator Conference (IPAC '19), Melbourne, 2019*, edited by M. Boland, H. Tanaka, D. Button, R. Dowd, V. R. W. Schaa, and E. Tan (JACoW Publishing, Geneva), p. 1916.
Zholents, A., *et al.*, 2016, Nucl. Instrum. Methods Phys. Res., Sect. A **829**, 190.
Zichichi, A., 1990, in *The Superworld II* (Springer, New York), pp. 443–499.
Zimmermann, F., 1994, Part. Accel. **49**, 67, https://cds.cern.ch/record/274807/files/p67.pdf.
Zimmermann, F., 1997, CERN Technical Reports No. LHC-Project-Report-95, No. CERN-LHC-Project-Report-95, and No. SLAC-PUB-7425.
Zimmermann, F., 2001a, CERN Report No. CERN-SL-2001-009-AP.
Zimmermann, F., 2001b, AIP Conf. Proc. **592**, 494.
Zimmermann, F., 2004, Phys. Rev. ST Accel. Beams **7**, 124801.
Zimmermann, F., 2018, J. Phys. Conf. Ser. **1067**, 022017.
Zimmermann, F., O. Bruning, and M. Klein, 2013, *Proceedings of the 4th International Particle Accelerator Conference, Shanghai, 2013*, edited by Z. Dai, C. Petit-Jean-Genaz, V. Schaa, and C. Zhang (JACoW Publishing, Geneva), p. 1017, http://accelconf.web.cern.ch/IPAC2013/papers/mopwo054.pdf.
Zimmermann, F., *et al.*, 2019, Eur. Phys. J. Special Topics **228**, 1109.
Zinovyev, L., *et al.*, 2018, Phys. Part. Nucl. Lett. **15**, 745.
Zlobin, A., *et al.*, 2019, in *Proceedings of the 2019 North American Particle Accelerator Conference (NA-PAC '19), Lansing, MI, 2019*, edited by M. Boland, H. Tanaka, D. Button, R. Dowd, V. R. W. Schaa, and E. Tan, p (JACoW Publishing, Geneva). 282, http://accelconf.web.cern.ch/napac2019/papers/moplo20.pdf.
Zlobin, A., *et al.*, 2020, IEEE Trans. Appl. Supercond. **30**, 1.
Zobov, M., 2013, *Handbook of Accelerator Physics and Engineering*, 2nd ed., edited by A. W. Chao, K. H. Mess, M. Tigner, and F. Zimmermann (World Scientific, Singapore), Chap. 2.5.2, pp. 174–175.
Zobov, M. (for the DAFNE Team), 2016, J. Phys. Conf. Ser. **747**, 012090.
Zobov, M., C. Milardi, P. Raimondi, E. Levichev, P. Piminov, D. Shatilov, and K. Ohmi, 2009, ICFA Beam Dyn. Newsl. **48**, 34, https://icfa-usa.jlab.org/archive/newsletter/icfa_bd_nl_48.pdf.
Zobov, M., *et al.*, 2010, Phys. Rev. Lett. **104**, 174801.